Evolution of Fluvial Landscapes during the Eocene-Oligocene Transition in Central North America

Queenie Chang[1], Fernandes, Anjali M.[1], Hren, Michael T.[2], Smith, Virginia B.[3], Terry Jr., Dennis O.[4], Luffman, David B.[1], Rhodes, Mia M.[1], Kurtz, Madelyn A.[1]

[1] Department of Earth and Environmental Sciences, Denison University, 100 W College St.,Granville, OH 43023

[2] Department of Earth Sciences, University of Connecticut, 354 Mansfield Rd,Unit 1045, Storrs, CT 06269

[3] Department of Civil and Environmental Engineering, Villanova University, 800 Lancaster Ave., Villanova, PA 19085

[4] Department of Earth & Environmental Science, Temple University, Philadelphia, PA 19122

Corresponding author: Anjali M. Fernandes (fernandesa@denison.edu)

This is a non peer-reviewed pre-print submitted to EarthArXiv, and in review the Journal of Sedimentary Research.

Evolution of Fluvial Landscapes during the Eocene-Oligocene Transition in Central North America

Queenie Chang[1], Fernandes, Anjali M.[1], Hren, Michael T.[2], Smith, Virginia B.[3], Terry Jr., Dennis O.[4], Luffman, David B.[1], Rhodes, Mia M.[1], Kurtz, Madelyn A.[1]

[1] Department of Earth and Environmental Sciences, Denison University, 100 W College St.,Granville, OH 43023

[2] Department of Earth Sciences, University of Connecticut, 354 Mansfield Rd,Unit 1045, Storrs, CT 06269

[3] Department of Civil and Environmental Engineering, Villanova University, 800 Lancaster Ave., Villanova, PA 19085

[4] Department of Earth & Environmental Science, Temple University, Philadelphia, PA 19122

Corresponding author: Anjali M. Fernandes (fernandesa@denison.edu)

ABSTRACT

Rivers drive geomorphic change at Earth's surface by transporting sediment from mountains to sedimentary basins. They are sensitive to changes in water and sediment flux driven by tectonism, climatic perturbation and or volcanism. We characterized changes in fluvial landscapes during a major Cenozoic cooling event, the Eocene-Oligocene Transition (EOT) at 33.9 Ma. The EOT is characterized by a long term ~4-5°C decrease in global mean annual temperature, punctuated by short, intense climatic fluctuations. In the Great Plains region of central North America, the temperature decreased by ~7°C and mean annual precipitation declined by ~50% across the EOT. Preceding the EOT, renewed Cordilleran uplift near northeastern Nevada began at ~39 Ma and extensive volcanism in the Great Basin region occurred at ~36 Ma. We reconstruct characteristics of rivers and floodplains through the Late Eocene-

Early Oligocene deposits of White River Group (WRG), exposed at Toadstool Geologic Park in northwestern Nebraska, U.S.A., and evaluate how river landscapes responded to these events.

We identified five stages of change in the paleo-rivers and -floodplain strata of the White River Group: (1) Following the Laramide uplift, the rivers of the Late Eocene Chamberlain Pass Formation adjusted from steep gradients (~10^{-3}) to gentler ones (~10^{-4}), and transitioned from shallow, mobile channels to deeper, stable channels and floodplains. (1) The transition from the Chamberlain Pass Formation to the Late Eocene Chadron Formation saw a shift from a relatively coarse-grained fluvial system with mobile channels to an extremely fine-grained, aggradational, floodplain-dominated system influenced by high volcanogenic sediment loads. (3) The transition from the Late Eocene Chadron Formation to the Early Oligocene Orella Member of the Brule Formation is associated with the onset of the Eocene-Oligocene Transition (EOT) and is marked by coarse floodplains and ephemeral river deposits that display evidence of significant, likely seasonality-driven, discharge variability. (4) Early Oligocene strata (33.9 - 31.6 Ma) also show compelling evidence of recurrent episodes of sustained channel incision and fill that we connect to climate fluctuations associated with the early phase of relatively rapid EOT cooling. (5) Early Oligocene strata deposited from 33.4 to 31.6 Ma show no significant erosional surfaces and continue to reflect discharge variability, high volcanogenic sediment loads, and a relatively stable climate system after the end of the initial phase of rapid cooling.

1. INTRODUCTION

Rivers are vital components of Earth's hydrological cycle and play a critical role in shaping landscapes by transporting sediment from catchments to sedimentary basins. Environmental perturbations such as variations in tectonic, climatic and volcanic forcings can exert significant influence on river networks. In this work, we explore the impacts of environmental changes on river landscapes in central North America during the Eocene-Oligocene transition (EOT) approximately 33.9 - 33.5 million years ago (Ma) and we focus on the late Eocene-early Oligocene White River Group (WRG) deposits exposed in Nebraska, USA. (Fig.1).

A significant body of work exists to describe tectonic, climatic and volcanic activity during this period (e.g., (Sjostrom et al., 2006; Zanazzi et al., 2007; Boardman and Secord, 2013; Fan et al., 2020). However, detailed characterizations of rivers and their floodplains across this key interval are limited (Fernandes et al, in review; (Galloway et al., 2011; Korus and Joeckel, 2023)). Here, we address this knowledge gap by parameterizing changes in stratal patterns, particle size and channel hydraulic geometries in river landscapes during this period of paleoenvironmental change.

In the Great Plains of North America, river landscapes may have been influenced by three possible external factors: They are:

(1) tectonically driven changes in surface relief (uplift/subsidence) and moisture availability associated with late stage surface uplift of the North American Cordillera (~40 - 38 Ma) (Mix et al., 2011; Chamberlain et al., 2012; Fan et al., 2018),

(2) long term cooling and drying associated with the EOT (33.9 - 33.5 Ma), punctuated by cycles of climatic variability for the ~300 ky at the beginning of the Oligocene (Zachos et al., 2001a; Coxall et al., 2005; Zanazzi et al., 2007),

(3) transported volcaniclastic sediment influx from intense pyroclastic volcanism (~36 Ma) in the Great Basin region (Larson and Evanoff, 1998; Best et al., 2009, 2013), associated with the roll-back of the subducting Farallon plate and upwelling of the asthenosphere in its place.

All three factors may have caused alterations in river hydraulic geometry (width,depth, gradient) and fluvial stratigraphic patterns from the Late Eocene through the Early Oligocene.

1.2 Tectonically driven changes in relief (uplift/subsidence)

The Laramide orogeny in the North American Cordillera resulted from the compression during the shallow subduction of the oceanic Farallon plate beneath the North American continental plate ((DeCelles, 2004)). After the Laramide orogeny, the region's evolution was shaped by extensional tectonics. This was due to the rollback of the subducting oceanic plate or slab sinking, which led to the upwelling of the asthenosphere from north to south ((Humphreys, 1995; Schmandt and Humphreys, 2010)).

These tectonic processes caused a rapid north-to-south wave of surface uplift. By the early Eocene, a topographic wave had formed in northwestern North America (British Columbia and eastern Washington) around 50 million years ago. This wave moved southward, reaching mid-western North America (northeastern Nevada) around 40 to 38 million years ago, and southern Nevada by about 23 million years ago ((Chamberlain et al., 2012)).

By the late Eocene, the mean elevation and relief between the central Rockies and the western Great Plains is thought to have reached present-day levels (Sjostrom et al., 2006; Mix et al., 2011; Chamberlain et al., 2012; Fan et al., 2014a, 2014b)). A widespread disconformity between the upper Cretaceous and late Eocene strata in western Nebraska indicates extensive erosion around 42 to 37 million years ago, linked to the surface uplift of the central Rockies during this period ((Cather et al., 2012)). Topographic changes associated with this uplift increased the supply of coarse-grained sediment to fluvial systems on the Great Plains after the late Eocene ((Galloway et al., 2011; Blum et al., 2017)). Slow subsidence and increased sedimentation associated with surface uplift resulted in widespread aggradation on the Great Plains (McMillan et al., 2006).

1.1 Climatic variability associated with the Eocene Oligocene Transition

The Eocene-Oligocene transition (EOT), around 34 million years ago, was the most dramatic climate shift of the Cenozoic era, marked by significant global climate changes (Zachos et al., 2001b). Marine isotope data indicate a global mean annual temperature decrease of 4-5°C (Zachos et al., 2001a; Coxall et al., 2005). Over roughly 300,000 years beginning at 33.9 Ma, fluctuating carbon dioxide (CO2) levels (from about 1,100 ppm to below 750 ppm) led to changes in atmospheric and oceanic circulation patterns (Zachos et al., 2001b). Along with favorable orbital conditions like insolation minima, these changes eventually triggered the formation of the first large-scale permanent ice sheets on Antarctica ((Ivany et al., 2003, 2006; Galeotti et al., 2016)).

Unlike marine data, terrestrial records of environmental change during the EOT are relatively sparse and vary widely. For instance, clumped isotope data from gastropod shells on the Isle of Wight (Hampshire Basin, UK) show a 4-5°C cooling that coincides with changes in CO_2 levels (Hren et al., 2013). In North America, terrestrial records also indicate overall cooling, but the extent of temperature change is inconsistent, ranging from less than 2°C to 8°C (Zanazzi et al., 2007; Retallack, 2007; Sheldon, 2009)).

Zanazzi et al. (2007) estimated that mean annual temperatures dropped by about 8.2°C across the EOT, between 33.7 Ma and 33.3 Ma, based on the oxygen isotope composition ($\delta^{18}O$) of fossil bone carbonate. Similarly, Fan et al. (2018) found an approximate 7°C decrease in air temperature from the latest Eocene to the early Oligocene, around 34.5 Ma to 33.5 Ma, using clumped isotope paleotemperature data of pedogenic carbonate samples. However, these reconstructions cover a broader time range due to lower sample resolution.

Despite this dramatic estimated decrease in temperature, the $\delta^{18}O$ of fossil mammal teeth showed limited change throughout the EOT (Zanazzi et al., 2007; Boardman and Secord, 2013). This is surprising because such a significant cooling should have led to a notable decline in the $\delta^{18}O$ of ambient water. A possible concern with these paleotemperature reconstructions is that the δ18O values of carbonate might be influenced by evaporation during formation, potentially introducing significant bias (Quade et al., 2007).

1.3 Pyroclastic volcanism in the Great Basin region

The rollback of the subducting oceanic Farallon plate is thought to have triggered extensive volcanic activity in the Great Basin region from the latest Eocene to the Oligocene (Sato and Denson, 1967; Lipman and McIntosh, 2008; Best et al., 2009, 2013). Evidence suggests that explosive volcanism and ignimbrite flare-ups in eastern Nevada and western Utah were active between approximately 36 Ma and 18 Ma (Best et al., 2009, 2013). Geochemical analysis of mineral phases and age correlation of volcanic tuffs indicate that Great Basin volcanism was a major source of pyroclastic material found in the Eocene-Oligocene White River Group deposits (Larson and Evanoff, 1998).

1.4 The Eocene-Oligocene Strata of the White River Group

The Eocene-Oligocene White River Group (WRG) consists of extensive volcaniclastic fluviolacustrine and eolian deposits spread across the northern Great Plains (Sahy et al., 2015), from southwestern North Dakota to northeastern Colorado (Fig. 1E). Exposures of the WRG in northwestern Nebraska near the Toadstool Geological Park (TGP) have been studied extensively and now have high-resolution age control (Evanoff, 1990; Swisher and Prothero, 1990; Terry et al., 1998; Prothero and Emry, 2004; Sahy et al., 2015; Fan et al., 2020).

The WRG contains numerous late Eocene-Oligocene mammal fossil assemblages, which provide the basis for defining the Chadronian (38.0 - 33.9 Ma), Orellan (33.9 - 33.3 Ma), and Whitneyan (33.3 - 30.8 Ma) North American Land Mammal Ages (NALMA) (Prothero and Emry, 2004). Stratal age constraints are further supported by detailed magnetostratigraphy (Prothero and Swisher, 1992; Prothero, 1996; Prothero and Whittlesey, 1998) and single-crystal laser fusion $^{40}Ar/^{39}Ar$ dates from volcanic ash layers (Swisher and Prothero, 1990; Larson and Evanoff, 1998). More recently, high-precision $^{206}Pb/^{238}U$ zircon dates have refined these age constraints (Sahy et al., 2015).

At Toadstool Geologic Park in northwestern Nebraska, the WRG is divided into three formations in order of depositional age (Fig. 1B, C): (1) the Late Eocene Chamberlain Pass Formation, (2) the Late Eocene Chadron Formation, and (3) the Oligocene Brule Formation.

(1) The Late Eocene Chamberlain Pass Formation (CPF)

Vertebrate fossils in the CPF date to the Chadronian (38.0 - 33.9 Ma), including an early Chadronian brontothere jaw recovered from a channel sandstone (Wood et al., 1941; Emry et al., 1987) (Vondra, 1958; Terry, 1998). No radiometric dates currently exist from the CPF.

The CPF consists of white fluvial sandstone, mudstone, and basal conglomerate, with the upper part overprinted by pedogenesis and displaying a reddish-brown paleosol (Terry, 1998). This episode of pedogenesis is equivalent to the Interior Paleosol Series and Weta Paleosol Series described by Retallack (1983) and Terry and Evans (1994) in southwestern South Dakota. Pedogenic features preserved within the channel sandstone and overbank deposits suggest that soils were formed under oxidizing, acidic, and well-drained conditions (Terry and Evans, 1994). Authors infer seasonal wet and dry cycles linked to climatic shifts between humid and dry phases (Terry and Evans, 1994). Mean annual precipitation (MAP) estimated from the chemical index of weathering of these paleosols of the CPF is 1168 ± 181 mm/yr (Bobik, 2021).

(2) The Late Eocene Chadron Formation (CF)

The CF is dated to approximately 36.5-34 Ma based on $^{40}Ar/^{39}Ar$ dating of tephras (Swisher and Prothero, 1990), magnetostratigraphy (Prothero and Swisher, 1992; Prothero, 1996; Prothero and

Whittlesey, 1998), and land mammal faunal ages (Emry et al., 1987). Recent $^{206}Pb/^{238}U$ zircon ages from beds TP1 and TP2 (Fig. 1C) at the base of the BCCM are 35.224 ± 0.038 Ma and 34.476 ± 0.021 Ma (Sahy et al., 2015).

The Chadron Formation (CF) sharply contrasts with the CPF and is divided into the Peanut Peak Member (PPM) and the Big Cottonwood Creek Member (BCCM) in northeastern Nebraska (Terry, 1998; Terry and LaGarry, 1998). The PPM is a predominantly bluish green, smectite-rich mudstone, consisting of volcaniclastic overbank silty claystone interbedded with tabular and lenticular channel sandstones (Terry and LaGarry, 1998). The BCCM, only distinguished in northwestern Nebraska, is a siltier, cliff-forming unit with volcaniclastic overbank silty claystone interbedded with tabular and lenticular channel sandstones (Terry and LaGarry, 1998). Weakly developed paleosols within both PPM and BCCM suggest less humid climate conditions than the underlying CPF (Terry, 1998, 2001). Estimated mean annual precipitation (MAP) from paleosols associated with CF strata is 830.22 ± 181 mm/yr (Bobik, 2021).

In southern South Dakota, the lowermost members of the Chadron Formation (named the Ahearm and Crazy Johnson Members) consists of sand and mud that fill the Red River paleo-valley. The valley cuts through the CPF and into the pre-Tertiary rock (Evans and Terry, 1994). The valley and deposits of the Ahearm and Crazy Johnson Members do not extend outside the southern extent of South Dakota. The Red River paleo-valley is interpreted as a large incision event that occurred during the late Eocene due to the regional Black Hills uplift (Evans and Terry, 1994).

(3) The Early Oligocene Brule Formation (BF)

The transition from the Chadron Formation to the Oligocene Brule Formation is delineated by the Upper Purplish White (UPW) ash layer. Although this ash layer is actually gray to the naked eye, it was initially described as "purplish white" by scientists who were wearing purple-tinted sunglasses. Schultz and Stout (1955) first identified the UPW, and its most recent $^{206}Pb/^{238}U$ zircon age constraint is 33.939 ± 0.033 Ma (Sahy et al., 2015) (Fig. 1C).

The Brule Formation exposure in the TGP area serves as the type section for this formation (LaGarry, 1998). The Brule Formation is further separated into the Orella Member, Whitney Member, and Brown Siltstone Member (Terry, 1998). Our study extends through the stratigraphic interval that encompasses the Orella Member (OM), which is characterized by rare single or multistoried channel sandstones within a ~50 m interval of thinly interbedded brown and brownish-orange volcaniclastic overbank claystones and siltstones, and bluish-green overbank sheet sandstone (LaGarry, 1998; Fan et al., 2020). Paleosols mapped through this section were described by Terry et al. (2001), as weakly developed inceptisols characteristic of cool and/or dry climates. Mean annual precipitation from this interval was estimated from paleosols as 347 ± 147 mm/yr (Bobik, 2021).

Serendipity ash layer (SA), in the middle of the OM dates to 33.414 ± 0.035 Ma (Sahy et al., 2015). The detrital zircon U-Pb age from the base of the overlying Whitney Member is 31.6 ± 0.5 Ma (Fan et al., 2020) (Fig. 1C)

2. METHODS

The shapes and mobility of rivers, and the physical characteristics and transport dynamics of the sediment they move, can be sensitive to environmental perturbation. In the sedimentary record, unsteadiness in external environmental factors can lead to variation in the records of bank full geometries of river channels and in the particle size and sedimentary structures of river and floodplain deposits (Mohrig et al., 2000; Foreman et al., 2012; Chamberlin and Hajek, 2015; Ganti et al., 2020; Barefoot et al., 2022). From TGP exposures of the CPF, CF and OM (Fig. 1), we assembled measurements of (1) bar heights and cross-stream width as proxies for bank full width and depth (Fig. 2. A, B, C), (2) thicknesses of the individual sand bodies as proxies for the relative mobility of channels (Fig. 2, D) , (3) grain-size in sediment samples keyed to sedimentary structures and position on the landscape (i.e., channel versus floodplain, and (4) vertical stratigraphic columns.

We estimated the widths and depths of channels using the geometry of bar clinoforms and channel-filling mudstones (Fig. 2 A, B) with a combination of scaled photographs, tape measures, laser range finders, stratigraphic column measurements and LiDAR (Tables S1, S2, S3). Bank full flow depth was determined from the measured relief on fully-preserved bar clinoform surfaces and channel-filling mudstones; truncated or partially preserved bars were used as proxies for minimum flow depth (Fig. 2A, B) (Mohrig et al., 2000; Foreman et al., 2012; Barefoot et al., 2022). We estimated bar widths from the toe-to-crest horizontal distance of bar clinoforms on exposures that were transverse to the direction of transport (Greenberg et al., 2021) (Fig. 2A, B). Bank full flow widths were estimated by applying the empirical relation between the bank full flow width and clinoform bar width established by (Greenberg et al., 2021): Flow width = (2.34 ± 0.13) x bar width .

The thicknesses of individual sand bodies were measured to estimate the degree of aggradation relative to formative channel depth (Fig. 2A, B). Mohrig et al., 2000 demonstrated that freely avulsing, i.e., unconfined, river systems can aggrade to as much at 60% of its flow depth above its floodplain before the channel is primed to avulse. We used a ratio of sand body thickness to bank full flow depth of ~1.6 to separate freely avulsing from erosionally confined river channels as an index of relative channel stability (i.e. avulsivity; (Mohrig et al., 2000; Foreman et al., 2012; Barefoot et al., 2022).

We sampled deposits associated with (a) channel bed material load, including plane-laminated, cross-stratified and ripple-laminated sandstones, (b) channel suspended load, including climbing ripple laminated and climbing dune stratified sandstone, draping mudstones and mudstones trapped near the toes of inclined bar strata, and (c) flat-lying sandstones and mudstones associated with floodplain deposition (Fig. 3, 4, 5). The weakly cemented rock samples collected in the field were gently crushed using a mortar and pestle. The crushed sample was then disaggregated using a Q-sonica pulse generator which separated grains along partially cemented inter-grain boundaries. The disaggregated sediment was then separated into mud (< 62 μm), sand (62 μm - 2000 μm) and gravel (> 2000 μm), dried and weighed. The size-distributions of the different components were measured using a Horiba LA-960 Laser Particle Size

Analyzer (LPSA). Particle size distributions were generated using the weighted contributions of mud, sand and gravel (Fig. 6 A). The contributions of mud in bed material load (Fig. 6B) and the median particle sizes in floodplain sediment (Fig. 6C) were compared across stratigraphic units. We generated vertical stratigraphic columns to map key sedimentary structures, bed thickness, and grain size trends in the field (Fig. 7).

We used the detailed grain-size data from bed material load samples and the estimates of bank full flow depth to estimate the longitudinal slopes of the formative rivers through each unit. Based on the relationships developed by (Trampush et al., 2014) and (Mahon and McElroy, 2018) for sand bedded channels, we estimated paleoslope, S, using median particle diameter D_{50} of bed material and estimates of channel depth H_{bf}:

$$\log S = a_0 + a_1 * \log D_{50} + a_2 * \log H_{bf}$$

Where $a_0 = -2.08$, $a_1 = 0.254$, and $a_2 = -1.09$ are empirical coefficients.

3. RESULTS

3.1 Chamberlain Pass Formation

3.1.1 Outcrop description

Outcrops of Chamberlain Pass Formation (CPF) were mapped and sampled at Orella Road and Sugarloaf Road (Fig. 1G). CPF exposures along Sugarloaf Road were limited in vertical and lateral extent and comprise cross-bedded gravel-rich white sandstones and/or red paleosols (Fig. 1F). The most extensive CPF exposure was at Orella Road (Fig. 1G, 3). It comprises a ~6.7 m thick unit dominated by scour-based, white, inclined bed-sets, of trough cross-stratified and planar stratified, poorly sorted, gravel-rich, medium to very coarse grained sandstones with angular to subrounded particle shapes. The outcrop is capped by a bright red paleosol (Fig. 3A, 7A). Horizontally bedded, fine-grained, pedogenically-modified sandstone layers cap inclined, cross-stratified sandstones near the base of the outcrop (Fig. 3A). These layers transition laterally into beds that drape an erosionally-based, concave-up surface and before taper away on the opposite side (Fig. 3A). The pedogenically modified horizon separates the otherwise amalgamated gravel-rich sandstone outcrop into two distinct sand bodies (Fig. 3A, B). Elsewhere along the outcrop, sandstones are vertically amalgamated.

Conglomeratic deposits composed of very weakly cemented clast-supported, cross-bedded, granule to pebble sized particles are present at the base of the lower sand body (Fig. 3C). Elsewhere in the lower sand body, gravel-sized rip-up clasts, granules and pebbles are found imbricated within cross-bedded or inclined stratified sandstones, and concentrated within dune troughs (Fig. 4A). While granule-sized particles are still common in the upper sand body, pebble-sized clasts are less abundant. No mudstones are found within the sandstone unit; Sandstones sampled from the base of inclined strata, the pedogenically- modified layer and the adjacent draping beds were finer-grained than other parts of the sandstone outcrop.

Deep red mudstones dominate the upper part of this outcrop and are adjacent to scour-based, inclined, medium-grained, trough cross-stratified sandstone. The red mudstones overlie both conformable and erosional basal contacts with the underlying sandstones. The erosionally-based red mudstones display thin, inclined siltstone layers parallel to the adjacent inclined sandstones.

3.1.2 Interpretations to support detailed sampling and measurements

We interpreted the white, inclined sets of sandstone strata as clinoforms produced by migrating channel bars and the red pedogenically-modified horizons as relatively static floodplain surfaces. We interpret the flat-lying, pedogenically-modified horizon that caps inclined strata (Fig 3A) as representative of a period of stasis. The adjacent and laterally continuous draping beds are interpreted as channel fill associated with gradual channel avulsion (REf avulsion mechanics Mohrig, Hajek, Slingerlan, Edmonds). We inferred that the 6.7m sandstone unit was formed by avulsion and reoccupation of the same channel path (Chamberlin and Hajek, 2015). We separate the 6.7 m thick sandstone unit into an upper 4.9 m thick and a lower ~1.8 m thick sand body.

The deeply weathered, scour-based, red mudstones in the upper sand body are interpreted to be the product of passive filling of an abandoned channel. Inclined siltstone layers within the channel fill suggest an extended period during which the abandoned channel remained hydraulically connected to the newly avulsed main channel. The basal conglomerates are interpreted as part of the regional lag surface that overlies the Pierre Shale (Terry and Evans, 1994) and was later reworked and incorporated into CPF channels. The dominance of inclined stratification with imbricated gravel and trough crossbedding in this outcrop is interpreted to represent high transport stages.

3.1.3 Particle size and hydraulic geometry

Median particle sizes of the bed material load, sampled from trough cross-beds, planar stratified or inclined beds, and basal conglomerates, range between 3 μm - 3 mm; the median particle size in suspended load deposits, sampled from the bases of inclined bed-sets, is 5 - 20 μm (Fig. 6A). The median mud contribution to bed material deposits is 20-25% (Fig. 6B). The floodplain deposits are generally dominated by silt and clay, with a few samples including sand sizes >200 μm. Median floodplain particle size is 4 μm (Fig. 6C).

From bar strata in the lower sand body (n=1), we estimated bank full flow depth from one fully preserved bar as 1.76 m and bank full flow width as 29 m ± 2 m. From truncated or partially preserved bar strata (n=4) we estimated a minimum flow depth estimate of 1 - 1.6 m (Fig. 2 B, C). The maximum measured thickness of the lower sand body is 1.8 m and the ratio of sand body thickness to the flow depth is 1 (Fig. 2D). We estimated the longitudinal slope of the formative streams as 3.8×10^{-4} - 1.3×10^{-3}.

From fully preserved bar clinoforms in the upper sand body and the thickness of interpreted abandoned channel fill, we estimated bank full flow depths of 3 - 4.6 m. The width of fully-preserved bar clinoforms provided an estimated flow width of 29 ± 1.6 m to 41 ± 2 m (Fig. 2 B, C).The thickness of the upper sand body is 4.9 m; the ratio of sand body thickness to the flow depth is therefore 1.1 -1.6 (Fig. 2D). Estimated longitudinal slope of the formative streams was 1.1 - 7.8 x 10-4 (Fig. 2E). Source measurements for the CPF are recorded in Table S1.

3.2 Chadron Formation

3.2.1 Outcrop description

The Chadron Formation (CF) contains the Peanut Peak Member (PPM) and Big Cottonwood Creek Member (BCCM) (Fig. 1C, F). The PPM consists of structureless bluish green, gray, and olive claystones to siltstone. The thickness of PPM in NW Nebraska can vary from <1 m to >10 m thick. At the outcrop in the TGP area (Fig. 4), PPM is only ~1 m thick; in the outcrops along the Sugarloaf Road (Fig. 1F), PPM is around 10 m thick and contains thin layers of lacustrine gypsum and limestone near the contact with the overlying BCCM (Terry, 1998; Evans and Welzenbach, 1998).

The BCCM exposure in the TGP area (Fig. 4) is the type section of this unit (Terry and LaGarry, 1998). It is dominated by thick bluish green to gray claystone and siltstone interbedded with very fine-grained sandstone sheets (Fig. 4A). We mapped and sampled two laterally discontinuous outcrops of a 2.7m thick lenticular sand body near the base of the BBCM. The sand body is characterized by inclined sets of thin to medium bedded trough cross-bedded (Fig. 4C) or structureless, extremely mud-rich, extensively burrowed (Fig. 4E), very fine-grained sandstones or siltstones (Fig. 7B), interspersed with decimeter-scale mudstones that appear to drape coarser layers. One bed contains a high concentration of large mammal bone fragments (Fig. 4D).

3.2.2 Interpretations to support detailed sampling and measurements

We interpreted the inclined strata as channel bar clinoforms and the adjacent flat-lying mudstones as floodplain strata (Fig. 4A). We assumed the record of sediment transport modes, usually preserved in sedimentary structures, was obfuscated in sandstone beds with intense bioturbation, and so we did not sample these beds. From trough cross-stratification, generally indicative of high transport stages, in anomalously fine-grained deposits (Fig. 4C), we inferred that larger granular particles in transport had been converted to clay through post depositional chemical alteration. The accumulation of large mammal bone fragments (Fig. 4D) near the base of one such bed supported our inference that the formative channels transported significantly coarser sediment than was apparent from the particle size described in the field. Thick, inclined mudstones between the sandstone and siltstone inclined strata are interpreted as slack water deposits.

3.1.3 Particle size and hydraulic geometry

The floodplain deposits of both PPM and BCCM are dominated by clay and silt (Fig. 6C) and display median particle sizes in the 1 - 10 μm range. No channel sand bodies were found in PPM outcrops. The median grain size of bed material load in BCCM channel deposits ranges from 10 μm to 80 μm (Fig. 9). BCCM bed material deposits are anomalously rich in mud, which contributes between 45% and 100% of the sample mass (Fig. 6B). Overall, the Chadron Formation displays a narrow range in particle size for both floodplain and channel deposits (Fig. 6, Fig.7B, C).

From fully preserved BCCM bar clinoforms (n=2), we estimated a bank full flow depth of 1.2 - 1.6 m (Fig. 2B). From associated sand body thicknesses of 1.6 m - 2 m, we estimated a ratio of sand body thickness to flow depth of 0.7 - 1.7 (Fig. 2D). The minimum estimated bank full depth from a truncated bar deposit is 0.8 m (Fig. 2B). The estimated bank full flow width from one fully preserved bar exposed along a flow-transverse section is 11 m ± 1 m (Fig. 2C). Source measurements for the BCCM are recorded in Table S2.

Based on the presence of trough cross-stratification, we inferred that the formative channels were sand-bedded channels. We did not use the median grain-size from the measured distributions, because well-defined trough cross-beds are unlikely to form in silt. Instead, we used the range of sand-sized particles (63 - 200 μm) in bed material samples as representative of the median particle size of the bed material. With this assumption, our estimate of longitudinal channel gradient was 4.3 - 7.6 x 10^{-4} (Fig. 2E)

3.3 Orella Member

3.3.1 Outcrop description

The exposures of the Orella Member (OM) within the Toadstool Geological Park are laterally extensive and approximately 50m thick (Sahy et al., 2015).These exposures are predominantly composed of pale, interbedded sheet sandstone and volcaniclastic claystone and siltstone (Fig. 5A). Here we leverage existing detailed reconstructions of the paleohydrology associated with the OM (Fernandes et al., in review) and compare previous work with new data.

The lowermost OM strata above the Upper Purplish White (UPW) ash layer, dated at 33.9 Ma (Schultz and Stout, 1955; Sahy et al., 2015), consist of interbedded, flat-lying mudstones and thinly-bedded sandstones (Fig. 5 A). These strata are several meters thick in certain locations, but they are missing elsewhere and have been removed by up to 10 m of erosion into the underlying OM and BCCM strata (Grandstaff and Terry, 2009; Sahy et al., 2015)). Overlying the unconformity are two erosionally-based, multistoried sandstone bodies, separated by laminated mudstones, identified here as the lower sand body and the upper sand body (Fig. 5A-G). These units are characterized by inclined sets of eastward or north-eastward dipping, upward-fining, very fine- to coarse-grained, thinly- to thickly-bedded, trough cross-stratified, sub- to super-critically climbing ripple laminated, plane-laminated, or structureless sandstone beds (Fig. 5C-H, Fig. 7B, D).

The surfaces of these sandstone beds exhibit mudcracks (Fig. 5C), burrows (Fig. 5H), and well-preserved mammal hoofprints superimposed on ripple reworked tops of beds (Figs. 5F, 5G). Mud-rich climbing ripple laminated deposits and climbing dune cross-stratified deposits (Fig. 5D) are commonly associated with soft sediment deformation features (Fig. 2E). The sand bodies are encased in fine-grained, horizontally bedded mudstones with recurrent, closely spaced, ledge-forming tabular sandstone or siltstone beds.

Above the upper sand body and below the Serendipity Ash (33.414 +/- 0.035 Ma, (Sahy et al., 2015), the outcrop is dominated by brown to orange, volcaniclastic claystone to siltstone interbedded with pale-brown tabular sandstones (Fig. 5A, 5I). Paleosols mapped through this section were described by Terry et al., (2001), as weakly developed inceptisols.Tabular sandstones are thin to medium-bedded (less than 0.2 m thick), fine-to-medium-grained, plane- or ripple-laminated and rarely cross-bedded. Multiple erosional features, some of which are draped by volcanic ash (Fig.5I, Sahy et al., 2015), truncate horizontally-bedded sheet sandstones and siltstones, and are predominantly overlain by flat-lying mudstones interbedded with thin tabular sandstones. Weakly developed reddish-brown or orange paleosols are common.

Above the Serendipity Ash (~33.4 Ma, Sahy et al., 2015, Fig. 1C), up to the boundary between the OM and the overlying Whitney Member (~31.6 Ma, Sahy et al., 2015, Fig. 1 C), the outcrop is characterized by silty mudstone and interbedded tabular sandstones that are pedogenically modified and fine upward (Lukens, 2013). No large-scale erosional features are observed in this interval.

3.3.2 Interpretations to support detailed sampling and measurements

This sequence was previously identified as the TGP channel complex (Schultz and Stout, 1955; LaGarry, 1998). The inclined sandstone beds are interpreted as channel bar deposits, while the adjacent flat-lying interbedded sandstones and mudstones are interpreted as overbank floodplain deposits. Where individual inclined beds thin upwards and flatten out, transitioning into finer-grained mudstones and siltstones of adjacent floodplains, they are interpreted as fully preserved channel bars (Fernandes et al, in review, Chamberlin and Hajek, 2019). Mudstone layers interspersed between inclined sandstone beds are interpreted as slackwater deposits. We interpret thin- to medium-bedded flat lying tabular sandstones that are interbedded with laminated claystone and siltstone, and adjacent to channel sandstones, as crevasse splay deposits on floodplains. The erosional features above the upper sandstone body and below the Serendipity Ash are interpreted to represent periods of sustained channel incision (Fernandes et al., in review; Sahy et al., 2015).

Within channel deposits, abundant dune cross-stratification and plane lamination indicate high transport stages. Abundant climbing ripples, climbing dunes, and soft sediment deformation features suggest high suspended loads and rapid suspended sediment deposition. Mudcracks and mammal hoof prints on the channel beds imply that subaerial exposure of channel beds between high flow events was common (Fernandes et al., in review).

3.3.3 Particle size and channel hydraulic geometry

Bed material load, including trough cross-stratified, plane laminated, ripple laminated sandstones, contained median particle sizes ranging from 80 μm to 1000 μm (Fernandes et al, Fig. 6A). Suspended load, including climbing ripple laminated, climbing dune stratified sandstones and mud-rich draping layers, contained median particle sizes ranging from 10 μm to 200 μm (Fernandes et al, Fig. 6A). We found that mud contributions in channel bed material load range between 30% and 60%, which is less than that measured in the underlying BCCM and greater than in CPF. Floodplain deposits between the UPW (~33.9Ma) and the Serendipity ash (~33.4 Ma) are silt-rich, with a median particle size of 10 - 20 μm, while sampled floodplain deposits between the Serendipity and the base of the Whitney Member display a slightly finer median particle size of 6 μm.

Fernandes et al (in review) estimated peak flow depth from fully-preserved bar clinoforms (n=7) in the **lower** sand body as 1.6 - 2.8 m (Fig. 2B) and peak flow width as 56 +/- 3 m (Fig. 2C); measured sand body thickness was 5.3 - 6.5 m and the estimated ratio of sand body thickness to peak flow depth was ~2 - 4 (Fig. 2D). The minimum estimated flow depth from truncated clinoforms (n=94) was 1.1 m.The estimated longitudinal slope of the formative channels is 2.3 - 8.4 x 10^{-4}(Fig. 2E).

Peak flow depth estimated from fully preserved bar clinoforms (n=7) in the **upper** sand body was 1.6 - 2.8 m (Fig. 2B) and peak flow width was 56 +/- 3 m Fernandes et al (in review; Fig. 2C). Measured sand body thickness is 3.4 - 4.4 m and the ratio of sand body thickness to peak flow depth is 1 - 1.5 (Fig. 2D) . The minimum estimated flow depth from median thickness of truncated/partially preserved clinoforms (n=10) was 0.6 m. We estimated the longitudinal slope of the formative channels as 1.1 - 7.8 x 10^{-4}. Source measurements for OM strata are recorded in Table S-3.

From the interval above the upper sand body and below the Serendipity Ash, previous workers (Sahy et al. 2015, Fernandes et al) recorded several erosional surfaces overlain by flat-lying mudstones or thinly-bedded sandstones that onlap the margins of the erosional surface. One of the erosional features is draped by volcanic ash that preserves ~3.6 m of erosional relief. Another is overlain by ~2m of inclined, fining-upward, medium-bedded sandstones interpreted as channel bar deposits.

Fernandes et al. (in review) assumed two major episodes of sustained erosion punctuated by less significant filling and incision events; the first and second erosional episode produced maximum erosional relief of approximately 11 m and 4 m respectively (Fig. 5I). Elsewhere in TGP, (Sahy et al., 2015) measured two separate scours that preserve erosional relief of 15 m and 5 m, draped by the Horus and Serendipity ashes respectively (Fig. 1A, Fig. 5I). Fernandes et al., interpreted the predominantly fine-grained fill in the erosional scours to primarily be floodplain and crevasse splay deposits, and suggest that the true magnitude of erosional relief may be underestimated.

4. DISCUSSION

We characterized the sedimentary record of fluvial landscape change through the Late Eocene-Early Oligocene White River Group, northwestern Nebraska, using sedimentary structures keyed to grain-size distributions and reconstructed channel hydraulic geometries. With these results we assess the response of the fluvial transport systems to climate change, tectonic-driven surface uplift, and pyroclastic volcanism on river behavior across the Eocene/Oligocene boundary.

4.1 The Late Eocene Chamberlain Pass Formation (CPF)

From the distributions of particle sizes in bed material (Fig. 6A), we infer that CPF deposits in the TGP area (Fig. 3) were created by sand-bedded channels with sufficient transport capacity to transport gravel. We infer that formative channels were mobile, high-energy systems located proximal to their sediment source based on (a) the dominance of sedimentary structures such as trough cross beds and plane lamination characteristic of high-transport stages, (b) coarse, subangular to subrounded particles, and (c) the relatively scarcity of preserved fine-grained floodplain deposits.

Based on the presence of a pedogenically modified horizon on flat lying sandstone layers connected laterally to beds interpreted as filling an abandoned channel, we divided the outcrop into genetically distinct upper and lower sand bodies. The lower sand body was created by channels with bank full widths and depths of 1.76 m and 29 m respectively. The upper sand body was generated by deeper, wider channels with bank full flow depths width of 3 - 4.6m and 29 - 41m respectively. From the ratios of sand body thickness to flow depths (<1.6), we inferred that CPF channels were free to migrate, avulse and interact with their floodplains (Mohrig et al., 2000).

We infer a slight reduction in transport capacity of formative channels, between the lower and the upper sand body. The lower sand body displays significantly greater quantities of gravel (up to cobble sized clasts) and the upper sand body includes dominantly granule sized clasts. Our estimates of longitudinal slope ranged from 3.8×10^{-4} to 1.3×10^{-3} in the lower sand body and from 1.1 to 7.8×10^{-4} in the upper sand body. Thus, we infer that CPF channels evolved from shallower channels with steeper gradients, to deeper channels with gentler gradients. We infer that these channel deposits recorded the post-Laramide adjustment of fluvial systems to uplift that ended ~40 Ma.

Larger particles transported as bedload can trap mud in the pore spaces between grains. On the basis of an assumed bed sediment concentration of ~ 0.60, and bed porosity of 0.4 for sand-bedded streams, we view the contributions of mud in CPF bed material load as within reasonable bounds. A few samples, including those associated with interpreted gradual channel abandonment in the lower sand body, have higher volumes of mud present in the sample. We infer that these deposits were associated with a lesser degree of reworking on the bed prior to deposition and burial.

Floodplain strata show significant variability in particle size with a few coarse-grained sandstone layers but are dominated by silt and clay (Fig. 6C). Associated with the upper sand body, the bright red, channel-filling mudstones, and laterally adjacent bright red paleosols of deeply weathered floodplains suggest a warm, humid environment with mean annual precipitation of 1168 ± 181 mm/year and floodplains that were in stasis for long periods of time (Terry et al., 2001; Bobik 2021). This phase of landscape stability may have been a local condition associated with the period after channel avulsion; however, a widespread paleosol at this stratigraphic level across the Great Plains (Terry and Evans, 1994) may indicate that this phase of landscape stability was regional.

4.2 The late Eocene (~36.5 Ma - 33.9 Ma) Chadron Formation (CF)

From the abundance of extremely fine-grained (Fig. 6A, C) floodplain strata relative to channel deposits through the CF we surmised that the formative river systems comprised extensive floodplains that aggraded rapidly relative to the rates of channel migration. The dominance of floodplain strata through this section of the WRG has previously been attributed to some combination of (a) heightened aridity associated with the orogenic rainshadow from the ~4 km Sevier hinterland (Mix et al., 2011; Rowley and Fan, 2016; Fan et al., 2020)), (b) decreased discharge and transport capacity of rivers draining the northern Rockies (Galloway et al., 2011), (c) slow subsidence and high sediment supply from recently uplifted regions (McMillan et al., 2006), (d) deposition of large volumes of fine–grained volcanic ash from explosive volcanism in the Great Basin (Larson and Evanoff, 1998) and (e) enhanced supply of fine-grained aeolian loess deposits (Mix et al., 2011; Rowley and Fan, 2016; Fan et al., 2020). A recent study of CF paleosols indicate that they contain moderately alkaline to alkaline, light brownish gray, carbonate rich mudstone, which are characteristic of estimated mean annual precipitation of 830 ± 181 mm/yr (Bobik, 2021).

Our estimates indicate that BCCM channels in the CF were smaller than CPF channels, with estimated bank full flow depths and widths of 1.2 - 1.6 m and 11.4 m respectively (Fig. 2A, B). Our reconstructed river gradient from the BCCM channel outcrop is remarkably similar to that seen in the upper CPF (Fig. 2D). We treat these estimates with caution as our assumptions about the particle size of channel bed material could be incorrect. If correct, however, a decrease in channel depth coupled with similar longitudinal slopes to the underlying CPF suggest an overall decrease in sediment transport capacity and water flux. We speculate that the relative scarcity of the coarse grained particles in BCCM bed material relative to CPF bed material suggests that the coarser fractions of sediment load were trapped upstream as channels were no longer able to transport them. This hypothesis aligns with arguments that downstream sediment starvation and inland transgression of the ocean in the Gulf of Mexico was driven by enhanced sediment storage and decreasing river discharge associated with the transport system in this region (Galloway, 2011).

BCCM river channels produced strata that are roughly 1.6 times the estimated bank full flow depth (Fig. 2C). We therefore infer that channels were free to migrate and avulse across their floodplains. i.e., they were not confined by significant erosional relief and floodplain aggradation rates were not high enough to allow the channel to aggrade in place without triggering avulsion (Mohrig et al., 2000).

We attribute the anomalously high mud fraction in sampled cross-bedded strata from BCCM channels (~60%; Fig. 6B) to a combination of high fine-grained sediment loads and post-depositional chemical alteration of sand-sized pyroclastic material in bed material load. As this floodplain-dominated stratigraphic interval coincides with significant pyroclastic volcanism in the Great Basin (Larson and

Evanoff, 1998); (Sato and Denson, 1967; Lipman and McIntosh, 2008; Best et al., 2009, 2013), it is possible that easily weathered fragments of pyroclastic material contributed a significant fraction of fine sand-sized particles originally present in bed material. We emphasize this hypothesis is challenging to test with chemically weathered, pyroclastically-sourced, floodplain sediment, as the original grain-size of particles in transport cannot be determined by the measurement methods used in this study.

Pyroclastic products from explosive volcanism have been shown to contribute a significant volume of clay-size particles to the river system and increase suspended sediment loads. A modern example is the explosive 1991 Mount Pinatubo eruption in the Philippines which produced 3.4 - 4.4 km^3 of ash and tephra fall deposits (Paladio-Melosantos and Solidum, 1996). Abundant, easily erodible, fine-grained sediment blanketed adjacent river catchments. The consequent valley widening, fluvial instability and high sediment yields continued for at least two subsequent decades (Gran et al., 2011).

Volcanic ash deposition has been shown to reduce the soil infiltration and increase flood frequency and magnitude (Lavigne, 2004; Pierson et al., 2013; Saputra et al., 2023). An abundance of fine-grained material, delivered through fluvial or eolian sources, can clog pore spaces in floodplains, reducing permeability and infiltration rates, and thereby enhancing overland flow and flood magnitudes during precipitation events. Further, volcanic ash on floodplains can weather in place relatively rapidly. Laboratory experiments at pH 4 and 25^{o}C demonstrated that the lifetime of 1 mm of rhyolite glass was 4500 yr (Wolff-Boenisch et al., 2003); air-borne volcanic ash is expected to be finer grained and have shorter lifetimes. We speculate that large volumes (Larson and Evanoff, 1998) of rapidly weathering volcaniclastic sediment, transported within rivers and deposited on floodplains, fundamentally altered water and sediment routing patterns and produced floodplain-dominated strata on these landscapes. The impacts of large volumes of ash deposition on the dynamics of fluvial landscapes through geologic time are relatively under-studied. We speculate that rapidly weathering sediment on ash-shrouded fluvial landscapes would result in extensive clay-rich, relatively impermeable floodplains that are resistant to flow channelization and water infiltration, and can produce floodplain-dominated stratigraphy. While we did not find evidence of enhanced flood frequency and/or magnitude in the CF at TGP, lacustrine limestones within the BCCM, interpreted by Evans and Welzenbach (1998) to have formed in springfed lakes, support our reasoning and indicate that BCCM floodplains were not well drained.

4. The early Oligocene (~36.5 Ma - 33.9 Ma) Orella Member (OM) of the Brule Formation

The earliest Oligocene OM strata (33.9 - 33.4 Ma, Sahy et al., 2015) of Brule Formation are thought to span the initiation of the EOT. Fossil records suggest that the climate changed from subtropical with seasonal precipitation in the Late Eocene to temperate with a pronounced dry season in the early Oligocene (Evanoff, 1990). In the TGP area, the estimated mean annual precipitation (MAP) dropped from 830.22 ± 181 mm/yr associated with CF strata to 347 ± 147 mm/yr associated with OM strata (Bobik, 2021). Paleosol analyses suggest a transition from Late Eocene closed canopy forest to early Oligocene savanna woodlands with intermixed shrubs and grasses (Retallack, 1983).

The earliest Oligocene (33.9 - 33.4 Ma) OM strata are floodplain dominated and include two multi-story channel sand bodies. Estimates indicate that bank full flows were 1.6 - 2.8 m deep and 56 m wide in the lower sand body, and 2.3 - 44 m deep and 71 m wide in the upper sand body (Fernandes et al., in review). The close association of trough cross-beds and plane lamination, indicative of high transport stages, with exposure surfaces inferred from mud cracks and well-preserved hoof-prints superimposed on ripple reworked surfaces, suggests that channels were ephemeral with estimated median peak flows of 168 cms (Fernandes et al). Abundant climbing ripple and climbing dune deposits associated with soft sediment deformation features, are interpreted as evidence of high rates of suspended sediment deposition; Fernandes et al estimated a median deposition rate of 10cm/h, inferred to be associated with waning floods.

Lower OM floodplains, which display recurrent flat-lying, thin to medium bedded siltstones or sandstones, show the coarsest median particle size (~20 μm) of the studied WRG units. We speculate that reduced precipitation and enhanced seasonality during this period resulted in pronounced discharge variability and increased flood frequency and intensity (Stromberg et al., 2010), causing floods capable of advecting up to 200-μm-sized suspended particles into floodplains. From weakly developed soil horizons adjacent to channels (i.e., inceptisols), floodplains in this interval are inferred to be relatively unstable; the time between recurrent episodes of significant floodplain deposition was insufficient to form mature soils (Fernandes et al, in review; Terry et al., 2001; Bobik, 2021).

The proportion of volcaniclastic sediment input has been shown to increase upward within the WRG sequence (Larson and Evanoff, 1998), increasing to as much as 80% in the upper Brule Formation above the section studied here. Decreased permeability, associated with floodplains “clogged” by fine volcaniclastic sediment and/or continuing loess deposition may have further enhanced flood frequency and intensity. Continued influence of high volcanogenic suspended sediment loads is also inferred from elevated contributions of mud to bed material (~45%, Fig. 6. B).

While peak discharge estimates from channel sandstones are unremarkable (Fernandes et al., in review, the lower OM strata (33.9 - 33.4 Ma) display compelling evidence of multiple episodes of sustained channel incision and filling. The lowermost sand body is ~3 times thicker than the estimated flow depths of formative channels and is inferred to be associated with channels that were confined within a corridor with at least 6.5 m of erosional relief. Elsewhere, the underlying unconformity is associated with removal of up to 10m of pre-existing strata (Sahy et al., 2015). Above the upper sand body, multiple episodes of channel incision generated significant erosional relief up to 10 m, overlain by floodplain deposits, draping ash layers, and one instance of channel bar deposits (Fig. 5I) . Recurrent episodes of erosion and fill in the lower OM strata (33.9 - 33.4 Ma) suggest a significant degree of instability in the fluvial transport system. Above the Serendipity ash layer (~33.4 Ma, Sahy et al., 2015) and up to the Whitney Member (31.6 Ma, Fan et al., 2020), no significant erosional surfaces on the scale of that seen in older OM strata are observed

Fernandes et al., in review, speculated that significant climate variability and/or instability in volcaniclastic sediment supply were drivers of this variability. They proposed that fluctuation in sediment supply from volcanogenic sources caused alternating phases of aggradation and degradation in the formative rivers and floodplains. However, this and other studies (e.g.,Terry, 1993, Sahy et al, 2015) resolve no evidence of significant channel incision in the underlying CP units that are also associated with high, and possibly more, volcaniclastic input.

On the other hand, the ~300,000 year period at the onset of the EOT was characterized by fluctuating concentrations of atmospheric carbon dioxide (CO_2) between ~1,100 p.p.m.v. to <750 p.p.m.v. (Zachos et al., 2001b). Marine oxygen isotope records indicate significant variability in global climate associated with the cooling event near the Eocene-Oligocene boundary prior to 33.5 Ma; after 33.5 Ma the climate system seemed more stable (Coxall et al., 2005; Fig 1A). Terrestrial oxygen isotope records in central North America show significant climate variability prior to 33.3 Ma (Zannazi et al., 2007, Fig. 8). The lag between terrestrial and marine records (Fig. 8) may reflect the decoupling of the continent and oceanic component during global climatic change (Zanazzi et al., 2007).

Significant instability in the climate, connected to the variability in atmospheric and oceanic circulation patterns (Zachos et al., 2001b) may have produced pronounced and alternating wet and dry periods superimposed on the long term trend of cooling and drying. We hypothesize that river transience, recorded in the phases of sustained incision and aggradation, may have been the corresponding landscape response. We emphasize that while climate variability is our preferred interpretation for recurrent incision and fill patterns, additional paleoclimate proxy data informed by the complex stratigraphic relationships observed, are necessary to test this hypothesis.

Above the Serendipity ash layer (~33.4 Ma, Sahy et al., 2015) and up to the Whitney Member (~31.6 Ma, Fan et al., 2020), no significant erosional surfaces on the scale of that seen in older OM strata are observed. As this coincides with relative climate stabilization after the rapid cooling at the start of the

EOT (Coxall et al, 2005; Zachos et al., 2001; Zanazzi et al., 2007), we infer that fluvial landscapes returned to a relatively stable state and primarily recorded seasonally variable discharges and high volcaniclastic sediment supply.

CONCLUSIONS

Building on a substantial body of work from previous authors, we characterized patterns in channel hydraulic geometry and grain size trends through White River Group fluvial strata that span the Eocene Oligocene Transition in western Nebraska. We specifically investigate potential influences of tectonics, magmatism and long and short-term climate variability on river systems from ~38 Ma to 31.6 Ma.

Our key conclusions are summarized below and in Figure 8. We identified five stages of change in river landscapes from the paleo-river and -floodplain strata of the White River Group at/near Toadstool Geologic Park in Nebraska. They are:

1. After the final stages of Laramide uplift, river gradient adjustment occurred within the Chamberlain Pass Formation. Early rivers displayed reconstructed gradients up to ~10^{-3} and late stage rivers displayed lower gradients of ~10^{-4} . This phase of adjustment is marked by a transition from shallow, mobile, sand-and-gravel channels to deeper channels with less gravel in transport and stable adjacent floodplains. We observed no significant change in channel gradient through the rest of the study interval.
2. The transition from Late Eocene CPF to Late Eocene CF is marked by a shift from sand-rich channel-dominated strata to aggradational, floodplain-dominated strata; we infer that an increase in volcanogenic sedimentation during this and overlying study intervals produced floodplain dominated river systems. Channel bed material contains unusually high mud contributions, inferred to reflect both extremely high suspended sediment load and rapid post-depositional weathering of volcanogenic sediment.

3. The transition from Late Eocene CF to early Oligocene OM is marked by coarser floodplains with recurrent flat-lying sandstone and siltstone beds, and rare channel strata that show evidence of high transport stages with high suspended sediment loads punctuated by periods when channels were dry. We infer that OM strata were produced by ephemeral streams and dynamic floodplains that resulted from enhanced seasonality and discharge variability associated with the onset of the Eocene Oligocene Climate Transition.
4. Lower OM strata (33.9 - 33.4 Ma) are characterized by recurrent incision and filling events that we estimate produced upto ~10m of erosional relief on river landscapes. We attribute these punctuated episodes of incision and fill to significant instability in climate that produced alternating wet and dry periods associated with the early ~300 ky phase of relatively rapid cooling during the Eocene Oligocene Transition.
5. OM strata younger than 33.4 - 31.6 Ma, is composed predominantly of flat-lying claystones and silstones, with no significant erosional surfaces observed. We infer that these strata continue to record significant discharge variability associated with long term cooling and drying, high volcanogenic sediment loads, and a relatively stable climate system associated after the end of the initial phase of rapid cooling.

ACKNOWLEDGEMENTS

Funding for this research was provided by the National Science Foundation (Grant EAR-2023710), Denison University Research Fund, Denison University's Provost's Office and Denison's Anderson Summer Scholars program. We thank field and lab assistants Linda Contreras Garcia, TJ Cracas, George Fox, Anna Grendys, Tricia Klosterman, Laura Lapham, Baylee McGinnis, Thea Pederson, Andi Scroggs, Christopher Sparacio and Nay Woodley.

REFERENCES

Barefoot, E.A., Nittrouer, J.A., Foreman, B.Z., Hajek, E.A., Dickens, G.R., Baisden, T., and Toms, L., 2022, Evidence for enhanced fluvial channel mobility and fine sediment export due to precipitation seasonality during the Paleocene-Eocene thermal maximum: Geology, v. 50, p. 116–120.

Best, M.G., Barr, D.L., Christiansen, E.H., Gromme, S., Deino, A.L., and Tingey, D.G., 2009, The Great Basin Altiplano during the middle Cenozoic ignimbrite flareup: insights from volcanic rocks: International geology review, v. 51, p. 589–633.

Best, M.G., Christiansen, E.H., and Gromme, S., 2013, Introduction: The 36–18 Ma southern Great Basin, USA, ignimbrite province and flareup: Swarms of subduction-related supervolcanoes: Geosphere, v. 9, p. 260–274.

Blum, M.D., Milliken, K.T., Pecha, M.A., Snedden, J.W., Frederick, B.C., and Galloway, W.E., 2017, Detrital-zircon records of Cenomanian, Paleocene, and Oligocene Gulf of Mexico drainage integration and sediment routing: Implications for scales of basin-floor fans: Geosphere, v. 13, p. 2169–2205.

Boardman, G.S., and Secord, R., 2013, Stable isotope paleoecology of White River ungulates during the Eocene–Oligocene climate transition in northwestern Nebraska: Palaeogeography, palaeoclimatology, palaeoecology, v. 375, p. 38–49.

Bobik, T., 2021, A multiproxy approach to interpreting aridity across the Eocene-Oligocene Transition of the northern Great Plains (White River group), North America: Temple University, doi:10.34944/DSPACE/7221.

Cather, S.M., Chapin, C.E., and Kelley, S.A., 2012, Diachronous episodes of Cenozoic erosion in southwestern North America and their relationship to surface uplift, paleoclimate, paleodrainage, and paleoaltimetry: Geosphere, v. 8, p. 1177–1206.

Cather, S.M., Chapin, C.E., and Kelley, S.A., 2012, Diachronous episodes of Cenozoic erosion in southwestern North America and their relationship to surface uplift, paleoclimate, paleodrainage, and paleoaltimetry: Geosphere, v. 8, p. 1177–1206.

Chamberlain, C.P., Mix, H.T., Mulch, A., Hren, M., Kend-Corson, M., Davis, S., Horton, T., and Graham, S., 2012, The Cenozoic climatic and topographic evolution of the western North American Cordillera: American Journal of Science, v. 312, p. 213–262.

Chamberlain, Mix, Mulch, and Hren, 2012, The Cenozoic climatic and topographic evolution of the western North American Cordillera: American journal of physiology. Renal physiology.

DeCelles, P.G., 2004, Late Jurassic to Eocene evolution of the Cordilleran thrust belt and foreland basin system, western U.S.A: American journal of science, v. 304, p. 105–168.

Eley, Y., and Hren, M.T., 2016, Multi-proxy reconstructions of hydrologic change during the Eocene-Oligocene transition in the North American Interior, *in* 2016 AGU Fall Meeting, PP33B–2359.

Emry, R.J., Russell, L.S., and Bjork, P.R., 1987, The chadronian, orellan, and Whitneyan North American land mammal ages: Cenozoic mammals of North America: geochronology and biostratigraphy, p. 118–152.

Evanoff, E., 1990, Early Oligocene paleovalleys in southern and central Wyoming: Evidence of high local relief on the late Eocene unconformity: Geology, v. 18, p. 443–446.

Evans, J.E., and Terry, D.O., Jr, 1994, The significance of incision and fluvial sedimentation in the basal White River Group (Eocene-Oligocene), Badlands of South Dakota, USA: Sedimentary geology, v. 90, p. 137–152.

Evans, J.E., and Welzenbach, L.C., 1998, Episodes of carbonate deposition in a siliciclastic-dominated fluvial sequence, Eocene-Oligocene White River Group, South Dakota and Nebraska, *in* Terry, D.O., LaGarry, H.E., and Hunt, R.M. eds., Lithostratigraphy, paleontology, and biochronology of the Chadron, Brule, and Arikaree Formations in North Dakota,.

Fan, M., Ayyash, S.A., Tripati, A., Passey, B.H., and Griffith, E.M., 2018, Terrestrial cooling and changes in hydroclimate in the continental interior of the United States across the Eocene-Oligocene boundary: GSA Bulletin, v. 130, p. 1073–1084.

Fan, M., Feng, R., Geissman, J.W., and Poulsen, C.J., 2020, Late Paleogene emergence of a North American loess plateau: Geology, v. 48, p. 273–277.

Fan, M., Heller, P., Allen, S.D., and Hough, B.G., 2014b, Middle Cenozoic uplift and concomitant drying in the central Rocky Mountains and adjacent Great Plains: Geology, v. 42, p. 547–550.

Fan, M., Hough, B.G., and Passey, B.H., 2014a, Middle to late Cenozoic cooling and high topography in the central Rocky Mountains: Constraints from clumped isotope geochemistry: Earth and planetary science letters, v. 408, p. 35–47.

Fan, M., Mankin, A., and Chamberlain, K., 2015, Provenance and depositional ages of late Paleogene fluvial sedimentary rocks in the central Rocky Mountains, USA: Journal of atomic and molecular physics, v. 85, p. 1416–1430.

Feng, R., Poulsen, C.J., Werner, M., Page Chamberlain, C., Mix, H.T., and Mulch, A., 2013, Early Cenozoic evolution of topography, climate, and stable isotopes in precipitation in the North American Cordillera: American journal of science, v. 313, p. 613–648.

Foreman, B.Z., Heller, P.L., and Clementz, M.T., 2012, Fluvial response to abrupt global warming at the Palaeocene/Eocene boundary: Nature, v. 491, p. 92–95.

Galewsky, J., 2009, Rain shadow development during the growth of mountain ranges: An atmospheric dynamics perspective: Journal of Geophysical Research, v. 114, doi:10.1029/2008jf001085.

Galloway, W.E., Whiteaker, T.L., and Ganey-Curry, P., 2011, History of Cenozoic North American drainage basin evolution, sediment yield, and accumulation in the Gulf of Mexico basin: Geosphere, v. 7, p. 938–973.

Galloway, W.E., Whiteaker, T.L., and Ganey-Curry, P., 2011, History of Cenozoic North American drainage basin evolution, sediment yield, and accumulation in the Gulf of Mexico basin: Geosphere, v. 7, p. 938–973.

Gran, K.B., Montgomery, D.R., and Halbur, J.C., 2011, Long-term elevated post-eruption sedimentation at Mount Pinatubo, Philippines: Geology, v. 39, p. 367–370.

Greenberg, E., Ganti, V., and Hajek, E., 2021, Quantifying bank full flow width using preserved bar clinoforms from fluvial strata: Geology, v. 49, p. 1038–1043.

Humphreys, E.D., 1995, Post-Laramide removal of the Farallon slab, western United States: Geology, v. 23, p. 987–990.

Korus, J.T., and Joeckel, R.M., 2023, Exhumed fluvial landforms reveal evolution of late Eocene–Pliocene rivers on the Central and Northern Great Plains, USA: Geosphere, doi:10.1130/GES02587.1.

LaGarry, H.E., 1998, Lithostratigraphic revision and redescription of the Brule Formation (White River Group) of northwestern Nebraska, *in* Terry, D.O., LaGarry, H.E., and Hunt, R.M. eds., Depositional Environments, Lithostratigraphy, and Biostratigraphy of the White River and Arikaree Groups (Late Eocene to Early Miocene, North America), p. 63–92.

Larson, E.E., and Evanoff, E., 1998, Tephrostratigraphy and source of the tuffs of the White River sequence, *in* Terry, D.O., LaGarry, H.E., and Hunt, R.M. eds., Depositional Environments, Lithostratigraphy, and Biostratigraphy of the White River and Arikaree Groups (Late Eocene to Early Miocene, North America), p. 1–14.

Lavigne, F., 2004, Rate of sediment yield following small-scale volcanic eruptions: a quantitative assessment at the Merapi and Semeru stratovolcanoes, Java, Indonesia: Earth Surface Processes and Landforms, v. 29, p. 1045–1058.

Lipman, P.W., and McIntosh, W.C., 2008, Eruptive and noneruptive calderas, northeastern San Juan Mountains, Colorado: Where did the ignimbrites come from? GSA Bulletin, v. 120, p. 771–795.

McMillan, M.E., Heller, P.L., and Wing, S.L., 2006, History and causes of post-Laramide relief in the Rocky Mountain orogenic plateau: GSA Bulletin, v. 118, p. 393–405.

Mix, H.T., Mulch, A., Kent-Corson, M.L., and Page Chamberlain, C., 2011, Cenozoic migration of topography in the North American Cordillera: Geology, v. 39, p. 87–90.

Molnar, P., 2004, Late Cenozoic Increase in Accumulation Rates of Terrestrial Sediment: How Might Climate Change Have Affected Erosion Rates? Annual review of earth and planetary sciences, v. 32, p. 67–89.

Paladio-Melosantos, M.L.O., and Solidum, R.U., 1996, Tephra falls of the 1991 eruptions of Mount Pinatubo: Fire and mud: eruptions and lahars of Mount Pinatubo, Philippines, p. 513–535.

Pierson, T.C., Major, J.J., Amigo, Á., and Moreno, H., 2013, Acute sedimentation response to rainfall following the explosive phase of the 2008–2009 eruption of Chaitén volcano, Chile: Bulletin of Volcanology, v. 75, p. 723.

Prothero, D.R., 1996, Magnetic Stratigraphy of the White River Group in the High Plains, *in* Prothero DR, E.R.J. ed., The Terrestrial Eocene-Oligocene Transition in North America, Cambridge University Press, p. 247–262.

Prothero, D.R., and Emry, R.J., 2004, The Chadronian, Orellan, and Whitneyan North American Land Mammal Ages:, *in* Late Cretaceous and Cenozoic Mammals of North America, Columbia University Press, p. 156–168.

Prothero, D.R., and Swisher, C.C., III, 1992, Magnetostratigraphy and Geochronology of the Terrestrial Eocene-Oligocene Transition in North America:, *in* Prohero, D.R. and Berggrrn, W.A. eds., Eocene-Oligocene Climatic and Biotic Evolution, Princeton University Press, p. 46–73.

Prothero, D.R., and Whittlesey, K.E., 1998, Magnetic stratigraphy and biostratigraphy of the Orellan and Whitneyan land mammal “ages” in the White River Group, *in* Terry, D.O., LaGarry, H.E., and Hunt, R.M. eds., Depositional Environments, Lithostratigraphy, and Biostratigraphy of the White River and Arikaree Groups (Late Eocene to Early Miocene, North America), GEOLOGICAL SOCIETY OF AMERICA, INC, p. 39–62.

Quade, J., Garzione, C., and Eiler, J., 2007, Paleoelevation Reconstruction using Pedogenic Carbonates: Reviews in Mineralogy and Geochemistry, v. 66, p. 53–87.

Retallack, G.J., 1983, Late Eocene and Oligocene Paleosols from Badlands National Park, South Dakota: Geological Society of America, 82 p.

Rowley, J., and Fan, M., 2016, Middle Cenozoic diachronous shift to eolian deposition in the central Rocky Mountains: Timing, provenance, and significance for paleoclimate, tectonics, and paleogeography: Geosphere, v. 12, p. 1795–1812.

Sahy, D., Condon, D.J., Terry, D.O., Fischer, A.U., and Kuiper, K.F., 2015, Synchronizing terrestrial and marine records of environmental change across the Eocene–Oligocene transition: Earth and planetary science letters, v. 427, p. 171–182.

Saputra, D.D., Sari, R.R., Sari, I.N., Suprayogo, D., and van Noordwijk, M., 2023, Water repellency by volcanic ash interacting with organic matter: Incubation response and effect on infiltration: Geoderma, v. 436, p. 116535.

Sato, Y., and Denson, N.M., 1967, Volcanism and tectonism as reflected by the distribution of nonopaque heavy minerals in some Tertiary rocks of Wyoming and adjacent states: U.S. Geological Survey Professional Paper, p. C42–C54.

Schmandt, B., and Humphreys, E., 2010, Complex subduction and small-scale convection revealed by body-wave tomography of the western United States upper mantle: Earth and planetary science letters, v. 297, p. 435–445.

Schultz, B.C., and Stout, T.M., 1955, Classification of Oligocene sediment in Nebraska: A Guide for the Stratigraphic Collecting of Fossil Mammals: Bulletin of the University of Nebraska State Museum, v. 4, p. 17–52.

Stromberg, J.C., Lite, S.J., and Dixon, M.D., 2010, Effects of stream flow patterns on riparian vegetation of a semiarid river: Implications for a changing climate: River research and applications, v. 26, p. 712–729.

Sjostrom, D.J., Hren, M.T., Horton, T.W., Waldbauer, J.R., and Page Chamberlain, C., 2006, Stable isotopic evidence for a pre–late Miocene elevation gradient in the Great Plains–Rocky Mountain region, USA: Geological Society of America, v. Special Paper 398, p. 309–319.

Swisher, C.C., and Prothero, D.R., 1990, Single-Crystal ^{40}Ar/^{39}Ar Dating of the Eocene-Oligocene Transition in North America: Science, v. 249, p. 760–762.

Terry, D.O., and LaGarry, H.E., 1998, The Big Cottonwood Creek member: a new member of the Chadron formation in Northwestern Nebraska, *in* Terry, D.O., LaGarry, H.E., and Hunt, R.M. eds., Depositional Environments, Lithostratigraphy, and Biostratigraphy of the White River and Arikaree Groups (Late Eocene to Early Miocene, North America), pubs.geoscienceworld.org, p. 117–142.

Terry, D.O., Jr, 1998, Lithostratigraphic revision and correlation of the lower part of the White River Group: South Dakota to Nebraska, *in* Terry Jr, D. O., LaGarry, H. E., and Hunt, R. M. ed., Depositional Environments, Lithostratigraphy, and Biostratigraphy of the White River and Arikaree Groups (Late Eocene to Early Miocene, North America), Geological Society of America Special Paper.

Terry, D.O., Jr, 2001, Paleopedology of the Chadron Formation of Northwestern Nebraska: implications for paleoclimatic change in the North American midcontinent across the Eocene–Oligocene boundary: Palaeogeography, palaeoclimatology, palaeoecology, v. 168, p. 1–38.

Terry, D.O., Jr, and Evans, J.E., 1994, Pedogenesis and paleoclimatic implications of the Chamberlain Pass Formation, Basal White River Group, Badlands of South Dakota: Palaeogeography, palaeoclimatology, palaeoecology, v. 110, p. 197–215.

Trampush, S.M., Huzurbazar, S., and McElroy, B., 2014, Empirical assessment of theory for bank full characteristics of alluvial channels: Water resources research, v. 50, p. 9211–9220.

Vondra, C.F., 1958, Depositional history of the Chadron Formation in northwestern Nebraska: Proceedings: 68th Annual Meeting, Nebraska Academy of Sciences Abstracts.

Whipple, K.X., 2001, Fluvial Landscape Response Time: How Plausible Is Steady-State Denudation? American journal of science, v. 301, p. 313–325.

Wood, H.E., Chaney, R.W., Clark, J., Colbert, E.H., Jepsen, G.L., Reeside, J.B., Stock, C., and Committee, 1941, Nomenclature and correlation of the North American continental Tertiary: GSA Bulletin, v. 52, p. 1–48.

Zachos, J., Pagani, M., Sloan, L., Thomas, E., and Billups, K., 2001, Trends, Rhythms, and Aberrations in Global Climate 65 Ma to Present: Science, v. 292, p. 686–693.

Zanazzi, A., Kohn, M.J., MacFadden, B.J., and Terry, D.O., 2007, Large temperature drop across the Eocene–Oligocene transition in central North America: Nature, v. 445, p. 639–642.

Figure 01

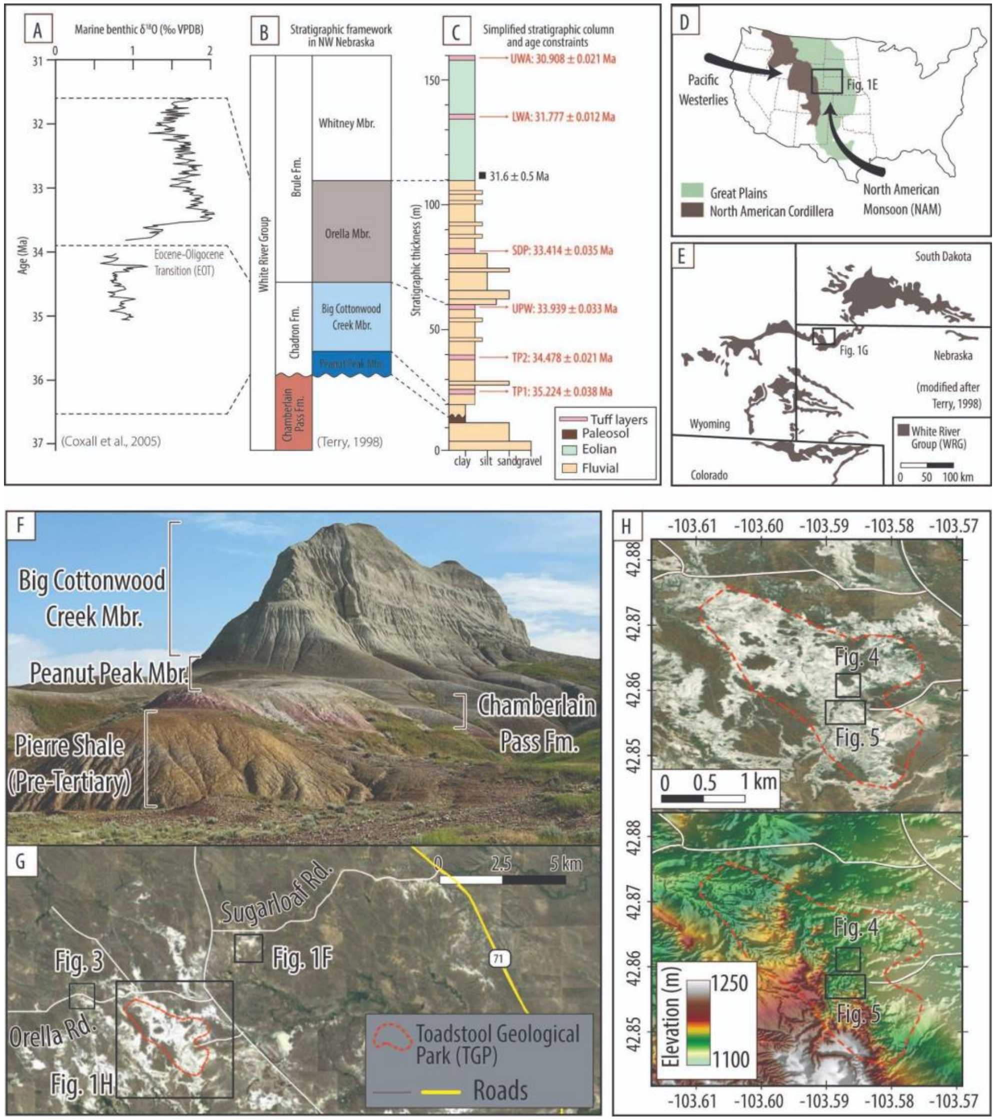

FIG. 1.—(A) High-resolution marine benthic $\delta^{18}O$ records from ODP site 1218 across the Eocene/Oligocene boundary (Coxall et al., 2005). (B) Stratigraphic framework of the Toadstool Geological Park (TGP) area in northwestern Nebraska. Studied stratigraphic units in this paper are color coded. (C) Simplified stratigraphic column and age constraints in the study area. Black squares = Age constraints from U-Pb age of detrital zircons (Fan et al., 2020)/ Red text = Zircon U-Pb ages from ash layers (Sahy et al., 2015). Abbreviation of ash layers: TP1 - Toadstool Park 1 Ash, TP2 - Toadstool Park 2 Ash, UPW - Upper Purplish White Layer, SA - Serendipity Ash, LWA - Lower Whitney Ash, UWA - Upper Whitney Ash. (D) Locality of the study area in the central Rocky Mountain and adjacent Great Plains in central North America. Thick black arrows showing the dominant wind direction in the present day. (E) Distribution of the White River Group (WRG) sedimentary succession in central North America. Black rectangle indicates the study area in NE Nebraska. (F) Representative photograph of the WRG succession at the Sugarloaf Road area. The location is shown on (G) The satellite image of the study area. (H) Detailed satellite image and elevation maps of the Toadstool Geological Park (TGP) area.

Figure 02

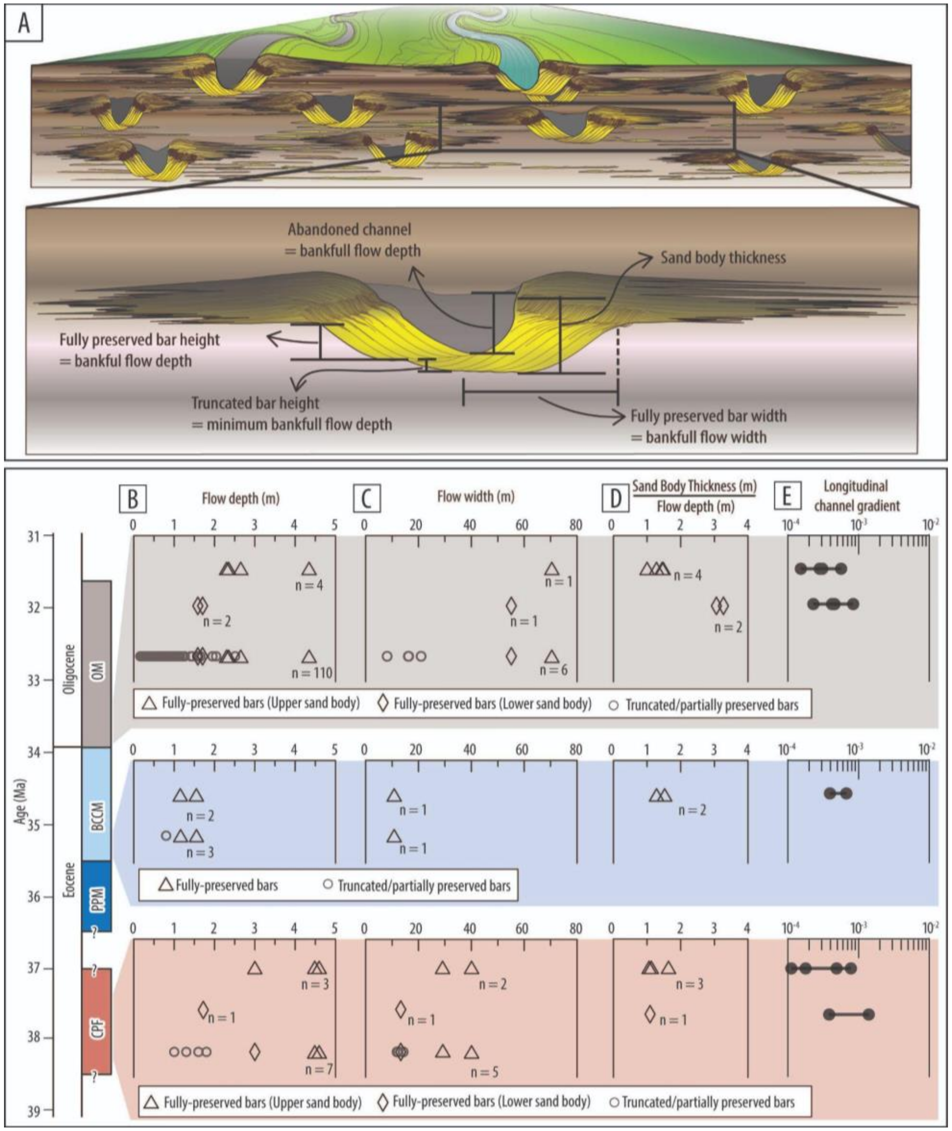

FIG. 2.— (A)Schematic diagram of fluvial stratigraphy constructed over geologic time, with schematic indicators of bar height, thickness of abandoned channel fills, bar width, sand body thickness for estimates collected in the field and used for estimates of (B) bank full flow depths, (C) bank full flow width, (D) ratios of sand body thickness to bank full flow depth. (E) Estimates longitudinal channel gradients.

Figure 03

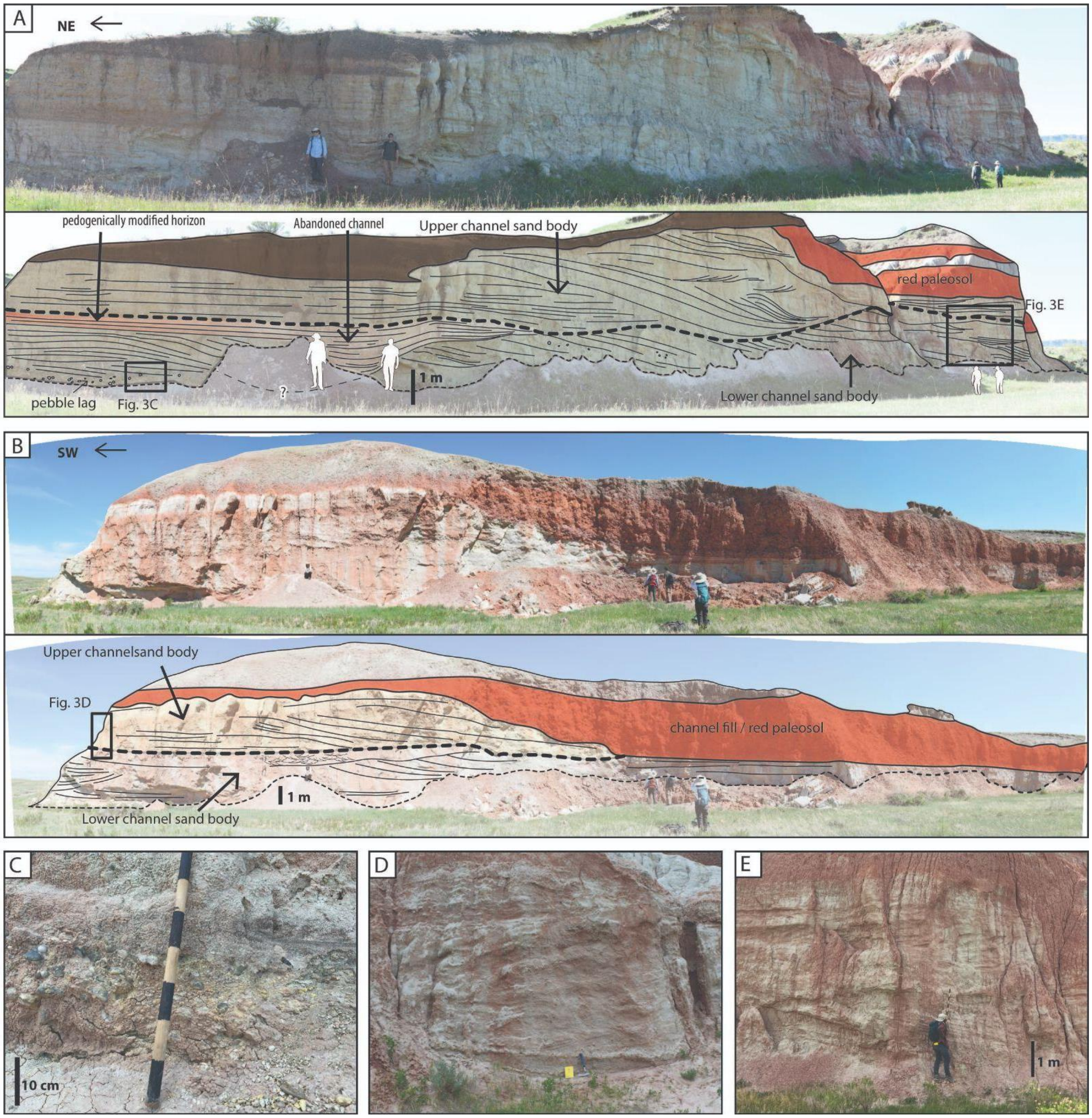

FIG. 3.—The representative outcrop of late Eocene Chamberlain Pass Formation (CPF) in the Toadstool Geological Park (TGP) area. (A) and (B) show two perspectives of the same continuous outcrops with interpreted diagrams showing key features and sedimentary structures such as (C) cross-bedded gravel deposit, (D) trough-cross beds, (E) inclined bar strata.

Figure 04

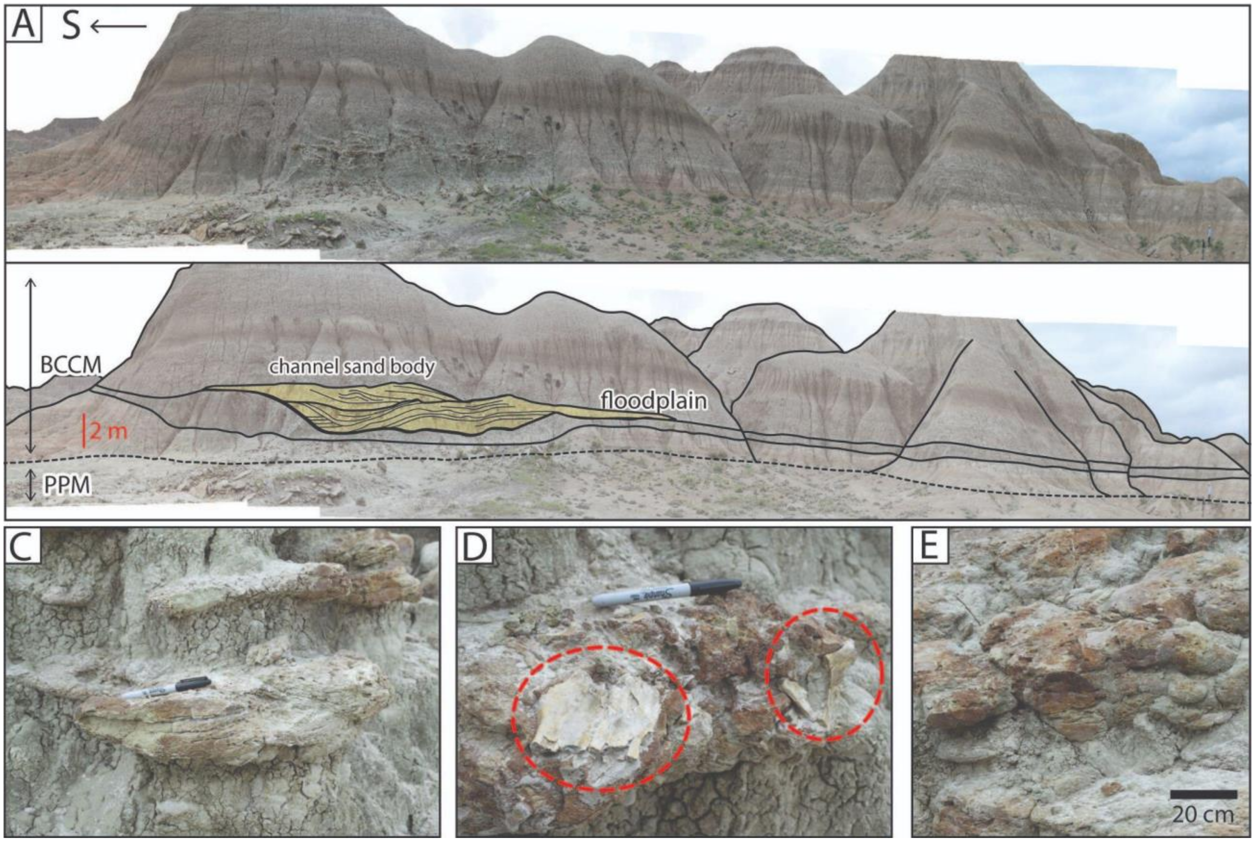

FIG. 4.— (A) The representative outcrop with (B) interpretation of key features of the late Eocene Chadron Formation (CF) in the Toadstool Geological Park (TGP) area, showing the Peanut Peak Member (PPM) and Big Cottonwood Creek Member (BCCM) and keys sedimentary structures including (C) trough cross-stratification, (D) mammal bone fragments (circled by red dashed line), and (E) burrows traces in cross-bedded strata.

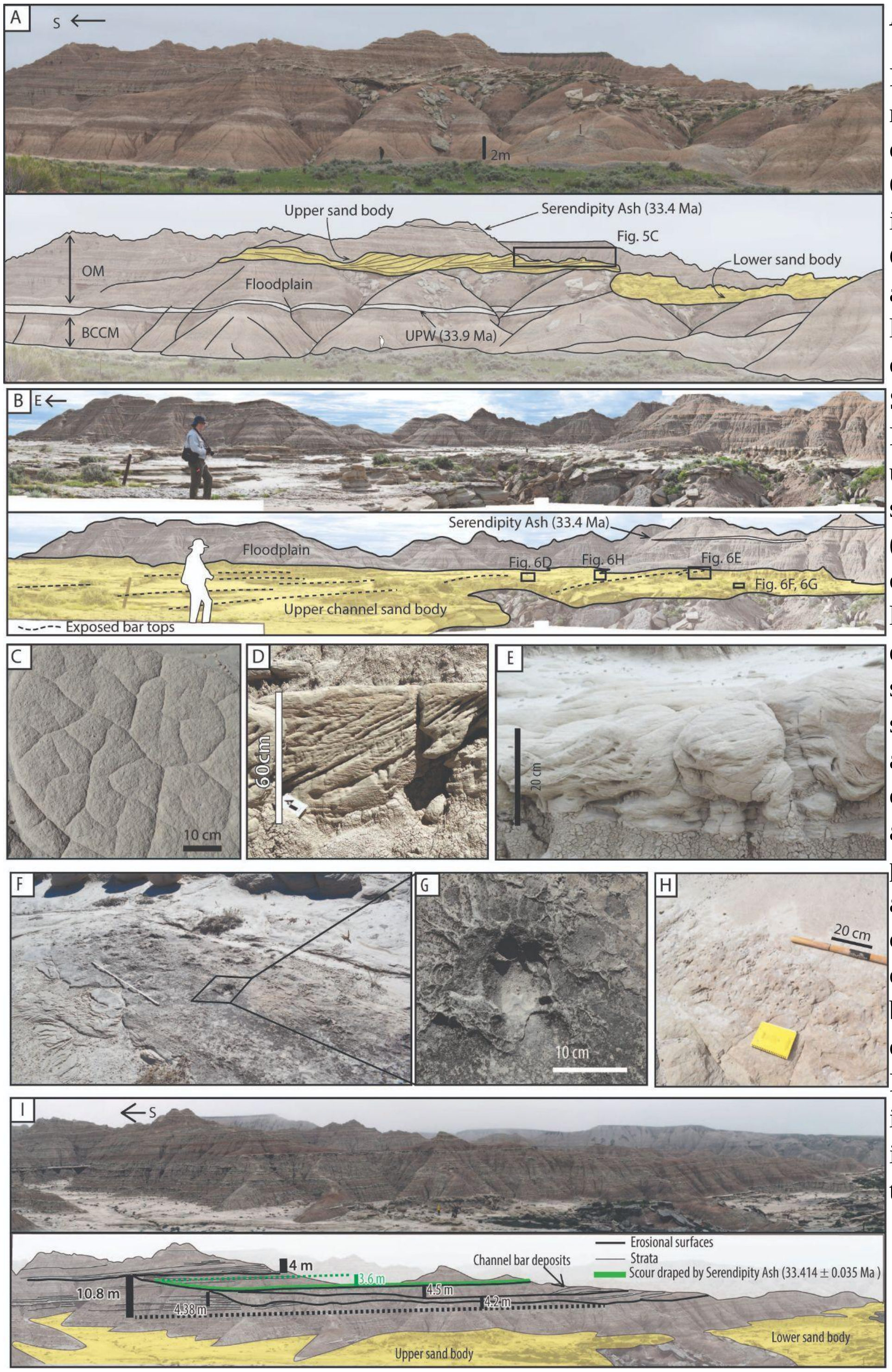

Figure 05

FIG. 5.— (B) The representative outcrop of early Oligocene Orella Member (OM) in the Toadstool Geological Park (TGP) area with key features labeled. Age constraints are after Sahy et al. (2015). (B) Perspective view of the upper sand body showing locations of (C) mud cracks, (D) climbing ripple laminated and climbing dune-stratified sandstones, (E) soft sediment deformation associated with climbing ripples, (F) and (G) mammal hoof prints superimposed on a ripple-reworked channel bed with traces of sediment splash, (H) burrows on the channe;l bed. (I) Photograph and interpretation of incision and fill above the upper sand body

Figure 06

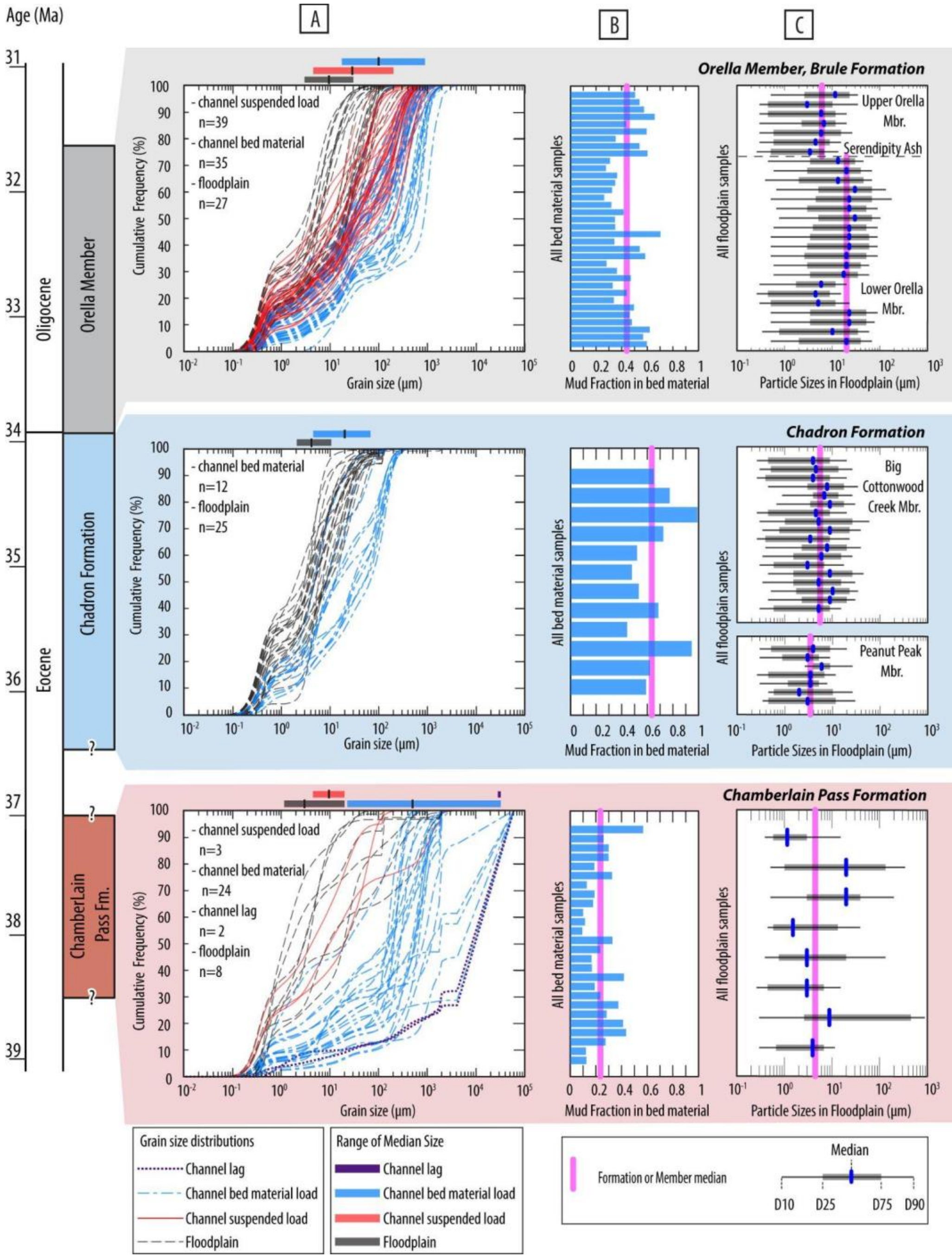

FIG. 6.— (A) Particle size distribution associated with different sedimentary facies in the studied units. (B) The mud fraction present in bed material samples. (ox plot of the grain size distribution of individual channel bed material load samples. (C) Box plot of the grain size distribution of individual floodplain samples.

Figure 07

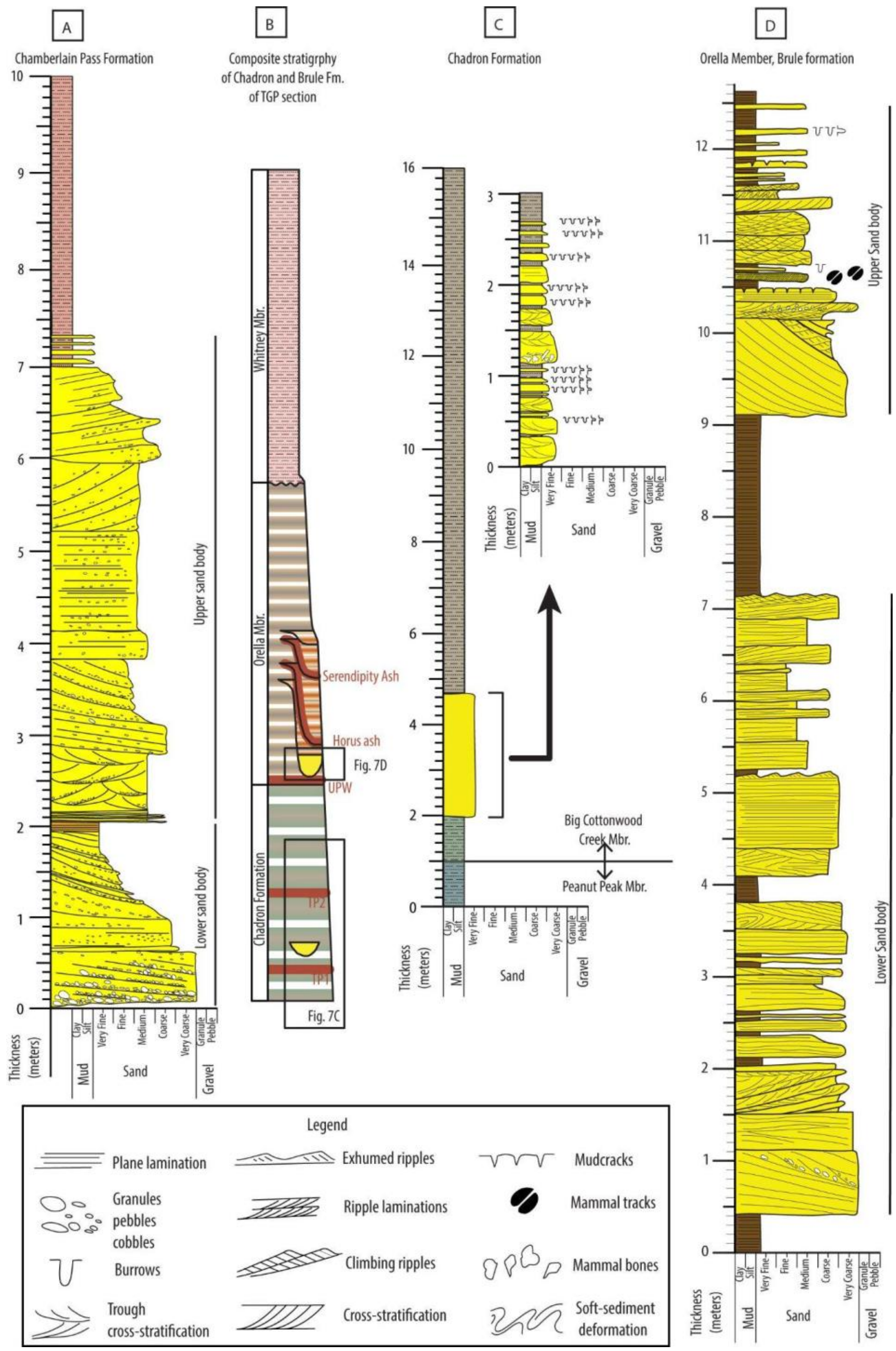

FIG. 7— Detailed Stratigraphic columns of the outcrops measured in the TGP area. (A) Chamberlain Pass Formation. (B) Composite stratigraphy of Chadron Formation and Brule Formation in the TGP section, modified after Sahy et al. (2015), showing the locations of (C) Chadron Formation. (D) Lower and upper sand bodies of the Orella Member.

Figure 08

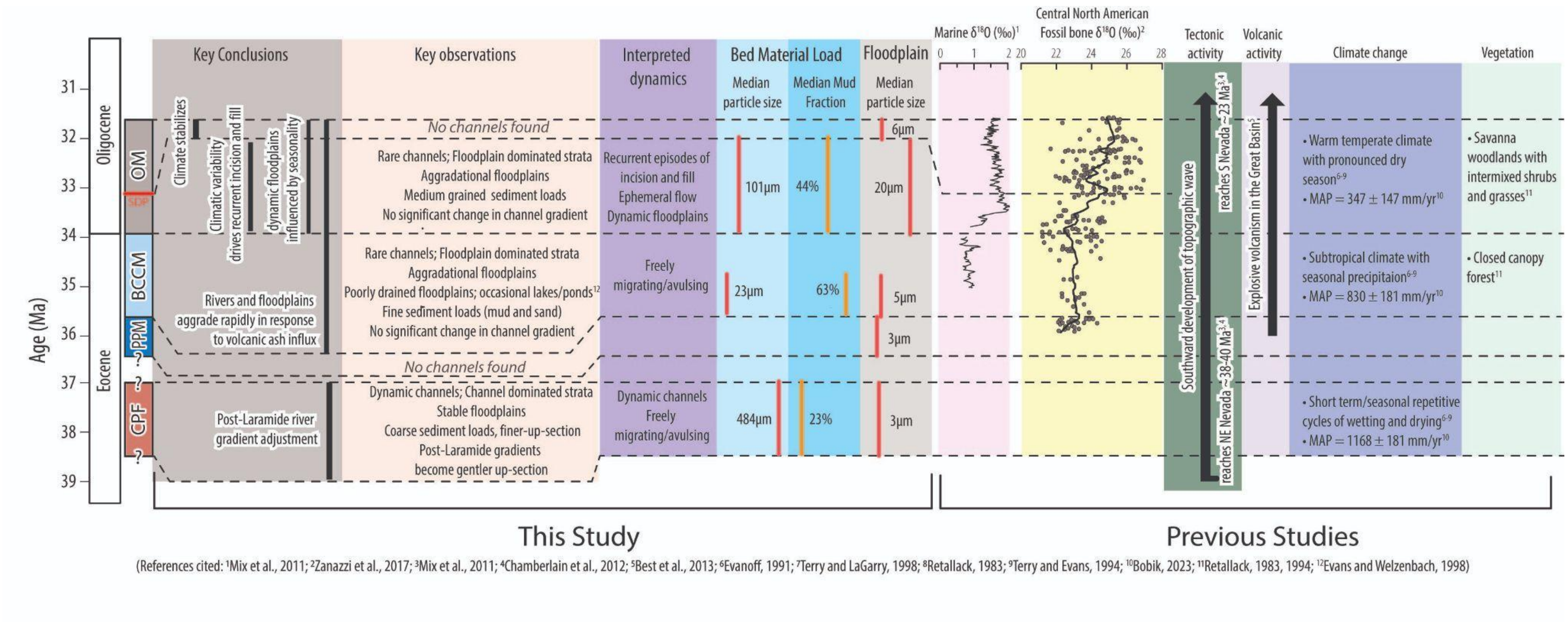

FIG. 8.—Summaries of key results and conclusions from our study, in the context of previous work on tectonism, climate change, and volcanism (literature compiled - [1]Mix et al., 2011; [2]Zanazzi et al., 2017; [3]Mix et al., 2011; [4]Chamberlain et al., 2012; [5]Best et al., 2013; [6]Evanoff, 1991; [7]Terry and LaGarry, 1998; [8]Retallack, 1983; [9]Terry and Evans, 1994; [10]Bobik, 2021; [11]Retallack, 1983, 1994; [12]Evans and Welzenbach,(1998)

Barefoot, E.A., Nittrouer, J.A., Foreman, B.Z., Hajek, E.A., Dickens, G.R., Baisden, T., and Toms, L., 2022, Evidence for enhanced fluvial channel mobility and fine sediment export due to precipitation seasonality during the Paleocene-Eocene thermal maximum: Geology, v. 50, p. 116–120.

Best, M.G., Barr, D.L., Christiansen, E.H., Gromme, S., Deino, A.L., and Tingey, D.G., 2009, The Great Basin Altiplano during the middle Cenozoic ignimbrite flareup: insights from volcanic rocks: International geology review, v. 51, p. 589–633.

Best, M.G., Christiansen, E.H., and Gromme, S., 2013, Introduction: The 36–18 Ma southern Great Basin, USA, ignimbrite province and flareup: Swarms of subduction-related supervolcanoes: Geosphere, v. 9, p. 260–274.

Blum, M.D., Milliken, K.T., Pecha, M.A., Snedden, J.W., Frederick, B.C., and Galloway, W.E., 2017, Detrital-zircon records of Cenomanian, Paleocene, and Oligocene Gulf of Mexico drainage integration and sediment routing: Implications for scales of basin-floor fans: Geosphere, v. 13, p. 2169–2205.

Boardman, G.S., and Secord, R., 2013, Stable isotope paleoecology of White River ungulates during the Eocene–Oligocene climate transition in northwestern Nebraska: Palaeogeography, palaeoclimatology, palaeoecology, v. 375, p. 38–49.

Bobik, T., 2021, A multiproxy approach to interpreting aridity across the Eocene-Oligocene Transition of the northern Great Plains (White River group), North America: Temple University, doi:10.34944/DSPACE/7221.

Cather, S.M., Chapin, C.E., and Kelley, S.A., 2012, Diachronous episodes of Cenozoic erosion in southwestern North America and their relationship to surface uplift, paleoclimate, paleodrainage, and paleoaltimetry: Geosphere, v. 8, p. 1177–1206.

Chamberlain, Mix, Mulch, and Hren, 2012, The Cenozoic climatic and topographic evolution of the western North American Cordillera: American journal of physiology. Renal physiology, https://www.ajsonline.org/content/312/2/213.short.

Chamberlin, E.P., and Hajek, E.A., 2015, Interpreting Paleo-Avulsion Dynamics from Multistory Sand Bodies: Journal of Sedimentary Research, v. 85, p. 82–94.

Chamberlin, E.P., and Hajek, E.A., 2019, Using bar preservation to constrain reworking in channel-dominated fluvial stratigraphy: Geology, v. 47, p.531-534, https://doi.org/10.1130/G46046.1

Coxall, H.K., Wilson, P.A., Pälike, H., Lear, C.H., and Backman, J., 2005, Rapid stepwise onset of Antarctic glaciation and deeper calcite compensation in the Pacific Ocean: Nature, v. 433, p. 53–57.

DeCelles, P.G., 2004, Late Jurassic to Eocene evolution of the Cordilleran thrust belt and foreland basin system, western U.S.A: American journal of science, v. 304, p. 105–168.

Emry, R.J., Russell, L.S., and Bjork, P.R., 1987, The chadronian, orellan, and Whitneyan North American land mammal ages: Cenozoic mammals of North America: geochronology and biostratigraphy, p. 118–152.

Evanoff, E., 1990, Early Oligocene paleovalleys in southern and central Wyoming: Evidence of high local relief on the late Eocene unconformity: Geology, v. 18, p. 443–446.

Evans, J.E., and Terry, D.O., Jr, 1994, The significance of incision and fluvial sedimentation in the basal White River Group (Eocene-Oligocene), Badlands of South Dakota, USA: Sedimentary geology, v. 90, p. 137–152.

Evans, J.E., and Welzenbach, L.C., 1998, Episodes of carbonate deposition in a siliciclastic-dominated fluvial sequence, Eocene-Oligocene White River Group, South Dakota and Nebraska, *in* Terry, D.O., LaGarry, H.E., and Hunt, R.M. eds., Lithostratigraphy, paleontology, and biochronology of the Chadron, Brule, and Arikaree Formations in North Dakota,.

Fan, M., Ayyash, S.A., Tripati, A., Passey, B.H., and Griffith, E.M., 2018, Terrestrial cooling and changes in hydroclimate in the continental interior of the United States across the Eocene-Oligocene boundary: GSA Bulletin, v. 130, p. 1073–1084.

Fan, M., Feng, R., Geissman, J.W., and Poulsen, C.J., 2020, Late Paleogene emergence of a North American loess plateau: Geology, v. 48, p. 273–277.

Fan, M., Heller, P., Allen, S.D., and Hough, B.G., 2014a, Middle Cenozoic uplift and concomitant drying in the central Rocky Mountains and adjacent Great Plains: Geology, v. 42, p. 547–550.

Fan, M., Hough, B.G., and Passey, B.H., 2014b, Middle to late Cenozoic cooling and high topography in the central Rocky Mountains: Constraints from clumped isotope geochemistry: Earth and planetary science letters, v. 408, p. 35–47.

Fernandes, A. M., Hren, M. T., Chang, Q, Smith, V. B., McGinnis, B., Terry, D. O., Jr., Luffman, D. B., Rhodes, M. M., Eley, Y., Kurtz, M. A., Heithaus, S. E., Paleohydrology of North American Catchments and Rivers at the Onset of the Eocene-Oligocene Climate Transition: Reconstructions from Fluvial Strata of the White River Group, Toadstool Geologic Park, Nebraska

Foreman, B.Z., Heller, P.L., and Clementz, M.T., 2012, Fluvial response to abrupt global warming at the Palaeocene/Eocene boundary: Nature, v. 491, p. 92–95.

Galeotti, S. et al., 2016, Antarctic Ice Sheet variability across the Eocene-Oligocene boundary climate transition: Science, v. 352, p. 76–80.

Galloway, W.E., Whiteaker, T.L., and Ganey-Curry, P., 2011, History of Cenozoic North American drainage basin evolution, sediment yield, and accumulation in the Gulf of Mexico basin: Geosphere, v. 7, p. 938–973.

Ganti, V., Hajek, E.A., Leary, K., Straub, K.M., and Paola, C., 2020, Morphodynamic hierarchy and the fabric of the sedimentary record: Geophysical research letters, v. 47, doi:10.1029/2020gl087921.

Grandstaff, D.E., and Terry, D.O., Jr, 2009, Rare earth element composition of Paleogene vertebrate fossils from Toadstool Geologic Park, Nebraska, USA: Applied geochemistry: journal of the International Association of Geochemistry and Cosmochemistry, https://www.sciencedirect.com/science/article/pii/S0883292708004617.

Gran, K.B., Montgomery, D.R., and Halbur, J.C., 2011, Long-term elevated post-eruption sedimentation at Mount Pinatubo, Philippines: Geology, v. 39, p. 367–370.

Greenberg, E., Ganti, V., and Hajek, E., 2021, Quantifying bank full flow width using preserved bar clinoforms from fluvial strata: Geology, v. 49, p. 1038–1043.

Humphreys, E.D., 1995, Post-Laramide removal of the Farallon slab, western United States: Geology, v. 23, p. 987–990.

Ivany, L.C., Van Simaeys, S., Domack, E.W., and Samson, S.D., 2006, Evidence for an earliest Oligocene ice sheet on the Antarctic Peninsula: Geology, v. 34, p. 377–380.

Ivany, L.C., Wilkinson, B.H., and Jones, D.S., 2003, Using Stable Isotopic Data to Resolve Rate and Duration of Growth throughout Ontogeny: An Example from the Surf Clam, Spisula solidissima: Palaios, v. 18, p. 126–137.

Korus, J.T., and Joeckel, R.M., 2023, Exhumed fluvial landforms reveal evolution of late Eocene–Pliocene rivers on the Central and Northern Great Plains, USA: Geosphere, doi:10.1130/GES02587.1.

LaGarry, H.E., 1998, Lithostratigraphic revision and redescription of the Brule Formation (White River Group) of northwestern Nebraska, *in* Terry, D.O., LaGarry, H.E., and Hunt, R.M. eds., Depositional Environments, Lithostratigraphy, and Biostratigraphy of the White River and Arikaree Groups (Late Eocene to Early Miocene, North America), p. 63–92.

Larson, E.E., and Evanoff, E., 1998, Tephrostratigraphy and source of the tuffs of the White River sequence, *in* Terry, D.O., LaGarry, H.E., and Hunt, R.M. eds., Depositional Environments, Lithostratigraphy, and Biostratigraphy of the White River and Arikaree Groups (Late Eocene to Early Miocene, North America), researchgate.net, p. 1–14.

Lavigne, F., 2004, Rate of sediment yield following small-scale volcanic eruptions: a quantitative assessment at the Merapi and Semeru stratovolcanoes, Java, Indonesia: Earth Surface Processes and Landforms, v. 29, p. 1045–1058.

Lipman, P.W., and McIntosh, W.C., 2008, Eruptive and noneruptive calderas, northeastern San Juan Mountains, Colorado: Where did the ignimbrites come from? GSA Bulletin, v. 120, p. 771–795.

Lukens, W., 2013, Paleopedology And Paleogeomorphology Of The Early Oligocene Orella And Whitney Members, Brule Formation, White River Group, Toadstool Geologic Park, Nebraska. MS Thesis.

Mahon, R.C., and McElroy, B., 2018, Indirect estimation of bedload flux from modern sand-bed rivers and ancient fluvial strata: Geology, https://pubs.geoscienceworld.org/gsa/geology/article-abstract/46/7/579/531398.

McMillan, M.E., Heller, P.L., and Wing, S.L., 2006, History and causes of post-Laramide relief in the Rocky Mountain orogenic plateau: GSA Bulletin, v. 118, p. 393–405.

Mix, H.T., Mulch, A., Kent-Corson, M.L., and Page Chamberlain, C., 2011, Cenozoic migration of topography in the North American Cordillera: Geology, v. 39, p. 87–90.

Mohrig, D., Heller, P.L., Paola, C., and Lyons, W.J., 2000, Interpreting avulsion process from ancient alluvial sequences: Guadalope-Matarranya system (northern Spain) and Wasatch Formation (western Colorado): GSA Bulletin, v. 112, p. 1787–1803.

Paladio-Melosantos, M.L.O., and Solidum, R.U., 1996, Tephra falls of the 1991 eruptions of Mount Pinatubo: Fire and mud: eruptions and lahars of Mount Pinatubo, Philippines, p. 513–535.

Pierson, T.C., Major, J.J., Amigo, Á., and Moreno, H., 2013, Acute sedimentation response to rainfall following the explosive phase of the 2008–2009 eruption of Chaitén volcano, Chile: Bulletin of Volcanology, v. 75, p. 723.

Prothero, D.R., 1996, Magnetic Stratigraphy of the White River Group in the High Plains, *in* Prothero

DR, E.R.J. ed., The Terrestrial Eocene-Oligocene Transition in North America, Cambridge University Press, p. 247–262.

Prothero, D.R., and Emry, R.J., 2004, The Chadronian, Orellan, and Whitneyan North American Land Mammal Ages:, *in* Late Cretaceous and Cenozoic Mammals of North America, Columbia University Press, p. 156–168.

Prothero, D.R., and Swisher, C.C., III, 1992, Magnetostratigraphy and Geochronology of the Terrestrial Eocene-Oligocene Transition in North America:, *in* Prohero, D.R. and Berggrrn, W.A. eds., Eocene-Oligocene Climatic and Biotic Evolution, Princeton University Press, p. 46–73.

Prothero, D.R., and Whittlesey, K.E., 1998, Magnetic stratigraphy and biostratigraphy of the Orellan and Whitneyan land mammal" ages" in the White River Group, *in* Terry, D.O., LaGarry, H.E., and Hunt, R.M. eds., Depositional Environments, Lithostratigraphy, and Biostratigraphy of the White River and Arikaree Groups (Late Eocene to Early Miocene, North America), GEOLOGICAL SOCIETY OF AMERICA, INC, p. 39–62.

Quade, J., Garzione, C., and Eiler, J., 2007, Paleoelevation Reconstruction using Pedogenic Carbonates: Reviews in Mineralogy and Geochemistry, v. 66, p. 53–87.

Retallack, G.J., 2007, Cenozoic Paleoclimate on Land in North America: The Journal of geology, v. 115, p. 271–294.

Retallack, G.J., 1983, Late Eocene and Oligocene Paleosols from Badlands National Park, South Dakota: Geological Society of America, 82 p.

Rowley, J., and Fan, M., 2016, Middle Cenozoic diachronous shift to eolian deposition in the central Rocky Mountains: Timing, provenance, and significance for paleoclimate, tectonics, and paleogeography: Geosphere, v. 12, p. 1795–1812.

Sahy, D., Condon, D.J., Terry, D.O., Fischer, A.U., and Kuiper, K.F., 2015, Synchronizing terrestrial and marine records of environmental change across the Eocene–Oligocene transition: Earth and planetary science letters, v. 427, p. 171–182.

Saputra, D.D., Sari, R.R., Sari, I.N., Suprayogo, D., and van Noordwijk, M., 2023, Water repellency by volcanic ash interacting with organic matter: Incubation response and effect on infiltration: Geoderma, v. 436, p. 116535.

Sato, Y., and Denson, N.M., 1967, Volcanism and tectonism as reflected by the distribution of nonopaque heavy minerals in some Tertiary rocks of Wyoming and adjacent states: U.S. Geological Survey Professional Paper, p. C42–C54.

Schmandt, B., and Humphreys, E., 2010, Complex subduction and small-scale convection revealed by body-wave tomography of the western United States upper mantle: Earth and planetary science letters, v. 297, p. 435–445.

Schultz, B.C., and Stout, T.M., 1955, Classification of Oligocene Sediments in Nebraska: A Guide for the Stratigraphic Collecting of Fossil Mammals: Bulletin of the University of Nebraska State Museum, v. 4, p. 17–52.

Sheldon, N., 2009, Nonmarine records of climatic change across the Eocene-Oligocene transition: Geological Society of, v. 452, p. 241–248.

Sjostrom, D.J., Hren, M.T., Horton, T.W., Waldbauer, J.R., and Page Chamberlain, C., 2006, Stable isotopic evidence for a pre–late Miocene elevation gradient in the Great Plains–Rocky Mountain region, USA: Geological Society of America, v. Special Paper 398, p. 309–319.

Stromberg, J.C., Lite, S.J., and Dixon, M.D., 2010, Effects of stream flow patterns on riparian vegetation of a semiarid river: Implications for a changing climate: River research and applications, v. 26, p. 712–729.

Swisher, C.C., and Prothero, D.R., 1990, Single-Crystal $^{40}Ar/^{39}Ar$ Dating of the Eocene-Oligocene Transition in North America: Science, v. 249, p. 760–762.

Terry, D.O., Jr, 1998, Lithostratigraphic revision and correlation of the lower part of the White River Group: South Dakota to Nebraska, *in* Terry Jr, D. O., LaGarry, H. E., and Hunt, R. M. ed., Depositional Environments, Lithostratigraphy, and Biostratigraphy of the White River and Arikaree Groups (Late Eocene to Early Miocene, North America), Geological Society of America Special Paper.

Terry, D.O., Jr, 2001, Paleopedology of the Chadron Formation of Northwestern Nebraska: implications for paleoclimatic change in the North American midcontinent across the Eocene–Oligocene boundary: Palaeogeography, palaeoclimatology, palaeoecology, v. 168, p. 1–38.

Terry, D.O., Jr, and Evans, J.E., 1994, Pedogenesis and paleoclimatic implications of the Chamberlain Pass Formation, Basal White River Group, Badlands of South Dakota: Palaeogeography, palaeoclimatology, palaeoecology, v. 110, p. 197–215.

Terry, D.O., and LaGarry, H.E., 1998, The Big Cottonwood Creek member: a new member of the Chadron formation in Northwestern Nebraska, *in* Terry, D.O., LaGarry, H.E., and Hunt, R.M. eds., Depositional Environments, Lithostratigraphy, and Biostratigraphy of the White River and Arikaree Groups (Late Eocene to Early Miocene, North America), pubs.geoscienceworld.org, p. 117–142.

Terry, D.O., LaGarry, H.E., and Hunt, R., Jr, 1998, Depositional Environments, Lithostratigraphy, and Biostratigraphy of the White River and Arikaree Groups (Late Eocene to Early Miocene, North America): Geological Society of America, 216 p.

Trampush, S.M., Huzurbazar, S., and McElroy, B., 2014, Empirical assessment of theory for bank full characteristics of alluvial channels: Water resources research, v. 50, p. 9211–9220.

Vondra, C.F., 1958, Depositional history of the Chadron Formation in northwestern Nebraska: Proceedings: 68th Annual Meeting, Nebraska Academy of Sciences,.

Wood, H.E., Chaney, R.W., Clark, J., Colbert, E.H., Jepsen, G.L., Reeside, J.B., Stock, C., and Committee, 1941, Nomenclature and correlation of the North American continental Tertiary: GSA Bulletin, v. 52, p. 1–48.

Zachos, J., Pagani, M., Sloan, L., Thomas, E., and Billups, K., 2001a, Trends, Rhythms, and Aberrations in Global Climate 65 Ma to Present: Science, v. 292, p. 686–693.

Zachos, J.C., Shackleton, N.J., Revenaugh, J.S., Pälike, H., and Flower, B.P., 2001b, Climate response to orbital forcing across the Oligocene-Miocene boundary: Science, v. 292, p. 274–278.

Zanazzi, A., Kohn, M.J., MacFadden, B.J., and Terry, D.O., 2007, Large temperature drop across the Eocene–Oligocene transition in central North America: Nature, v. 445, p. 639–642.

SUPPLEMENTAL MATERIALS

TABLE S1.— Field measurement results of bar height, bar width, and sand body thickness of Chamberlain Pass Formation (CPF).

TABLE S2.— Field measurement results of bar height, bar width, and sand body thickness of Big Cottonwood Creek Member (BCCM).

TABLE S3.— Field measurement results of bar height, bar width, and sand body thickness of Orella Member (OM).

TABLE S4.— LiDAR links to the Chamberlain Pass Formation and Orella Member outcrops.

FIG. S1.— Bar height and bar width results of Chamberlain Pass Formation (CPF).

FIG. S2.— Bar height and bar width results of Big Cottonwood Creek Member (BCCM).

FIG. S3.— Bar height and bar width results of Orella Member (OM).

FIG. S4.— Grain size distribution associated with sedimentary facies of all samples of CPF.

FIG. S5.— Grain size distribution associated with sedimentary facies of all samples of BCCM.

FIG. S6.— Grain size distribution associated with sedimentary facies of all samples of PPM.

FIG. S7.— Grain size distribution associated with sedimentary facies of all samples of OM.

FIG. S8.— Grain size distribution of individual channel bed material load samples of OM.

FIG. S9.— Grain size distribution of individual channel bed material load samples of BCCM.

FIG. S10.— Grain size distribution of individual channel bed material load samples of CPF.

FIG. S11.— Mud fraction of individual channel bed material load samples of OM.

FIG. S12.— Mud fraction of individual channel bed material load samples of BCCM.

FIG. S13.— Mud fraction of individual channel bed material load samples of CPF.

FIG. S14.— Grain size distribution of individual floodplain deposits samples of OM.

FIG. S15.— Grain size distribution of individual floodplain deposits samples of BCCM.

FIG. S16.— Grain size distribution of individual floodplain deposits samples of PPM.

FIG. S17.— Grain size distribution of individual floodplain deposits samples of CPF.

TABLE S1.— Field measurement results of bar height, bar width, and sand body thickness of Chamberlain Pass Formation (CPF).

Bar Number	**Upper/ Lower sand body**	**Bar Preservation**	**Type**	**Bar Height (m)**	**Sand Body Thickness (m)**	**Sand Body / Flow Depth**	**Bar Width (m)**	**Estimated Flow Width (m)**	**Supple. Fig. Index**
CPF-Bar 06	Upper	Fully preserved	Bar clinoforms	4.50	4.87	1.08	17.34	40.58	Fig. S1(F)
CPF-Bar 07	Upper	Fully preserved	Channel fill	4.60	4.87	1.06	--	--	Fig. S1(F)
CPF-Bar 03	Upper	Fully preserved	Bar clinoforms	3	4.87	1.62	12.32	28.83	Fig. S1(D)
CPF-Bar 01	Lower	Fully preserved	Bar clinoforms	1.76	1.76	1	5.50	12.87	Fig. S1(B)
CPF-Bar 04	Lower	Truncated	Bar clinoforms	1.80	--	--	5.50	12.87	Fig. S1(E)
CPF-Bar 02	Lower	Truncated	Bar clinoforms	1.60	--	--	6.30	14.74	Fig. S1(C)
CPF-Bar 05	Lower	Truncated	Bar clinoforms	1.00	--	--	--	--	Fig. S1(E)

TABLE S2.— Field measurement results of bar height, bar width, and sand body thickness of Big Cottonwood Creek Member (BCCM).

Bar Number	**Bar Preservation**	**Type**	**Bar Height (m)**	**Sand Body Thickness (m)**	**Sand Body / Flow Depth**	**Bar Width (m)**	**Estimated Flow Width (m)**	**Supple. Fig. Index**
BCCM-Bar01	Fully preserved	Bar clinoforms	1.22	2.6	1.38	--	--	Fig. S2(B)
BCCM-Bar02	Fully preserved	Bar clinoforms	1.6	2.4	1.5	4.86	11.37	Fig. S2(A)
BCCM-Bar03	Truncated	Bar clinoforms	0.9	2.4	--	--	--	Fig. S2(A)

TABLE S3.— Field measurement results of bar height, bar width, and sand body thickness of Orella Member (OM).

Bar Number	Upper or Lower sand body	Bar Preservation	Type	Bar Height (m)	Sand Body Thickness (m)	Sand Body / Flow Depth	Bar Width (m)	Estimated Flow Width (m)	Supple. Fig. Index
OM-Bar 66	Upper	Fully preserved	Bar clinoforms	4.35	4.35	1.00	30.31	70.93	Fig. S3(K)
OM-Bar 110	Upper	Fully preserved	Bar clinoforms	2.65	3.40	1.28	--	--	--
OM-Bar 111	Upper	Fully preserved	Bar clinoforms	2.35	3.40	1.45	--	--	--
OM-Bar 112	Upper	Fully preserved	Bar clinoforms	2.30	3.40	1.48	--	--	--
OM-Bar 49	Lower	Fully preserved	Bar clinoforms	1.59	6.50	4.09	23.83	55.76	Fig. S3(G)
OM-Bar 104	Lower	Fully preserved	Bar clinoforms	1.70	6.50	3.82	--	--	Fig. S3(R)
OM-Bar 110	Lower	Fully preserved	Bar clinoforms	2.82	5.26	1.87	--	--	Fig. S3(S)
OM-Bar 74	Upper	Truncated	Bar clinoforms	1.05	--	--	7.18	16.80	Fig. S3(M-N)
OM-Bar 22	Lower	Truncated	Bar clinoforms	0.60	--	--	3.70	8.66	Fig. S3(E)
OM-Bar 79	Lower	Truncated	Bar	1.95	--	--	7.12	16.66	Fig. S3(O)

			clinoforms						
OM-Bar 39	Lower	Truncated	Bar clinoforms	0.97	--	--	9.19	21.50	Fig. S3(F)
OM-Bar 64	Upper	Truncated	Bar clinoforms	1.57	--	--	--	--	Fig. S3(J)
OM-Bar 65	Upper	Truncated	Bar clinoforms	0.79	--	--	--	--	Fig. S3(J)
OM-Bar 67	Upper	Truncated	Bar clinoforms	0.94	--	--	--	--	Fig. S3(L)
OM-Bar 68	Upper	Truncated	Bar clinoforms	1.41	--	--	--	--	Fig. S3(L)
OM-Bar 69	Upper	Truncated	Bar clinoforms	1.10	--	--	--	--	Fig. S3(L)
OM-Bar 70	Upper	Truncated	Bar clinoforms	2.04	--	--	--	--	Fig. S3(L)
OM-Bar 71	Upper	Truncated	Bar clinoforms	2.51	--	--	--	--	Fig. S3(L)
OM-Bar 72	Upper	Truncated	Bar clinoforms	1.10	--	--	--	--	Fig. S3(L)
OM-Bar 73	Upper	Truncated	Bar clinoforms	0.82	--	--	--	--	Fig. S3(L)
OM-Bar 01	Lower	Truncated	Bar clinoforms	1.20	--	--	--	--	Fig. S3(A)
OM-Bar 02	Lower	Truncated	Bar clinoforms	0.40	--	--	--	--	Fig. S3(B)

OM-Bar 03	Lower	Truncated	Bar clinoforms	0.20	--	--	--	--	Fig. S3(B)
OM-Bar 04	Lower	Truncated	Bar clinoforms	0.65	--	--	--	--	Fig. S3(B)
OM-Bar 05	Lower	Truncated	Bar clinoforms	0.40	--	--	--	--	Fig. S3(B)
OM-Bar 06	Lower	Truncated	Bar clinoforms	1.00	--	--	--	--	Fig. S3(B)
OM-Bar 07	Lower	Truncated	Bar clinoforms	0.60	--	--	--	--	Fig. S3(B)
OM-Bar 08	Lower	Truncated	Bar clinoforms	1.70	--	--	--	--	Fig. S3(B)
OM-Bar 09	Lower	Truncated	Bar clinoforms	0.25	--	--	--	--	Fig. S3(B)
OM-Bar 10	Lower	Truncated	Bar clinoforms	1.65	--	--	--	--	Fig. S3(B)
OM-Bar 11	Lower	Truncated	Bar clinoforms	0.20	--	--	--	--	Fig. S3(B)
OM-Bar 12	Lower	Truncated	Bar clinoforms	0.72	--	--	--	--	Fig. S3(C)
OM-Bar 13	Lower	Truncated	Bar clinoforms	0.48	--	--	--	--	Fig. S3(C)
OM-Bar 14	Lower	Truncated	Bar clinoforms	0.48	--	--	--	--	Fig. S3(C)
OM-Bar 15	Lower	Truncated	Bar	0.32	--	--	--	--	Fig. S3(C)

			clinoforms						
OM-Bar 18	Lower	Truncated	Bar clinoforms	0.58	--	--	--	--	Fig. S3(D)
OM-Bar 19	Lower	Truncated	Bar clinoforms	0.60	--	--	--	--	Fig. S3(D)
OM-Bar 20	Lower	Truncated	Bar clinoforms	0.50	--	--	--	--	Fig. S3(E)
OM-Bar 21	Lower	Truncated	Bar clinoforms	0.35	--	--	--	--	Fig. S3(E)
OM-Bar 23	Lower	Truncated	Bar clinoforms	0.92	--	--	--	--	Fig. S3(F)
OM-Bar 24	Lower	Truncated	Bar clinoforms	0.33	--	--	--	--	Fig. S3(F)
OM-Bar 25	Lower	Truncated	Bar clinoforms	0.67	--	--	--	--	Fig. S3(F)
OM-Bar 26	Lower	Truncated	Bar clinoforms	0.50	--	--	--	--	Fig. S3(F)
OM-Bar 27	Lower	Truncated	Bar clinoforms	0.67	--	--	--	--	Fig. S3(F)
OM-Bar 28	Lower	Truncated	Bar clinoforms	0.33	--	--	--	--	Fig. S3(F)
OM-Bar 29	Lower	Truncated	Bar clinoforms	0.42	--	--	--	--	Fig. S3(F)
OM-Bar 30	Lower	Truncated	Bar clinoforms	0.30	--	--	--	--	Fig. S3(F)

OM-Bar 31	Lower	Truncated	Bar clinoforms	0.84	--	--	--	--	Fig. S3(F)
OM-Bar 32	Lower	Truncated	Bar clinoforms	1.14	--	--	--	--	Fig. S3(F)
OM-Bar 33	Lower	Truncated	Bar clinoforms	0.67	--	--	--	--	Fig. S3(F)
OM-Bar 34	Lower	Truncated	Bar clinoforms	0.47	--	--	--	--	Fig. S3(F)
OM-Bar 35	Lower	Truncated	Bar clinoforms	0.84	--	--	--	--	Fig. S3(F)
OM-Bar 36	Lower	Truncated	Bar clinoforms	0.67	--	--	--	--	Fig. S3(F)
OM-Bar 37	Lower	Truncated	Bar clinoforms	0.50	--	--	--	--	Fig. S3(F)
OM-Bar 38	Lower	Truncated	Bar clinoforms	0.92	--	--	--	--	Fig. S3(F)
OM-Bar 40	Lower	Truncated	Bar clinoforms	0.50	--	--	--	--	Fig. S3(F)
OM-Bar 41	Lower	Truncated	Bar clinoforms	0.58	--	--	--	--	Fig. S3(F)
OM-Bar 42	Lower	Truncated	Bar clinoforms	0.64	--	--	--	--	Fig. S3(F)
OM-Bar 43	Lower	Truncated	Bar clinoforms	0.24	--	--	--	--	Fig. S3(F)
OM-Bar 44	Lower	Truncated	Bar	0.16	--	--	--	--	Fig. S3(F)

			clinoforms						
OM-Bar 45	Lower	Truncated	Bar clinoforms	0.24	--	--	--	--	Fig. S3(F)
OM-Bar 46	Lower	Truncated	Bar clinoforms	0.24	--	--	--	--	Fig. S3(F)
OM-Bar 47	Lower	Truncated	Bar clinoforms	0.48	--	--	--	--	Fig. S3(F)
OM-Bar 48	Lower	Truncated	Bar clinoforms	0.24	--	--	--	--	Fig. S3(F)
OM-Bar 50	Lower	Truncated	Bar clinoforms	0.47	--	--	--	--	Fig. S3(G)
OM-Bar 51	Lower	Truncated	Bar clinoforms	0.47	--	--	--	--	Fig. S3(G)
OM-Bar 52	Lower	Truncated	Bar clinoforms	0.50	--	--	--	--	Fig. S3(G)
OM-Bar 53	Lower	Truncated	Bar clinoforms	0.33	--	--	--	--	Fig. S3(G)
OM-Bar 54	Lower	Truncated	Bar clinoforms	0.38	--	--	--	--	Fig. S3(G)
OM-Bar 55	Lower	Truncated	Bar clinoforms	0.58	--	--	--	--	Fig. S3(G)
OM-Bar 56	Lower	Truncated	Bar clinoforms	0.63	--	--	--	--	Fig. S3(G)
OM-Bar 57	Lower	Truncated	Bar clinoforms	0.97	--	--	--	--	Fig. S3(G)

OM-Bar 58	Lower	Truncated	Bar clinoforms	1.26	--	--	--	--	Fig. S3(H)
OM-Bar 59	Lower	Truncated	Bar clinoforms	0.72	--	--	--	--	Fig. S3(I)
OM-Bar 60	Lower	Truncated	Bar clinoforms	0.18	--	--	--	--	Fig. S3(I)
OM-Bar 61	Lower	Truncated	Bar clinoforms	0.81	--	--	--	--	Fig. S3(I)
OM-Bar 62	Lower	Truncated	Bar clinoforms	0.94	--	--	--	--	Fig. S3(I)
OM-Bar 63	Lower	Truncated	Bar clinoforms	0.54	--	--	--	--	Fig. S3(I)
OM-Bar 75	Lower	Truncated	Bar clinoforms	0.65	--	--	--	--	Fig. S3(O)
OM-Bar 76	Lower	Truncated	Bar clinoforms	0.75	--	--	--	--	Fig. S3(O)
OM-Bar 77	Lower	Truncated	Bar clinoforms	0.75	--	--	--	--	Fig. S3(O)
OM-Bar 78	Lower	Truncated	Bar clinoforms	0.95	--	--	--	--	Fig. S3(O)
OM-Bar 80	Lower	Truncated	Bar clinoforms	0.61	--	--	--	--	Fig. S3(P)
OM-Bar 81	Lower	Truncated	Bar clinoforms	0.50	--	--	--	--	Fig. S3(P)
OM-Bar 82	Lower	Truncated	Bar	0.50	--	--	--	--	Fig. S3(P)

			clinoforms						
OM-Bar 83	Lower	Truncated	Bar clinoforms	0.85	--	--	--	--	Fig. S3(P)
OM-Bar 84	Lower	Truncated	Bar clinoforms	1.10	--	--	--	--	Fig. S3(P)
OM-Bar 85	Lower	Truncated	Bar clinoforms	0.80	--	--	--	--	Fig. S3(P)
OM-Bar 86	Lower	Truncated	Bar clinoforms	0.40	--	--	--	--	Fig. S3(P)
OM-Bar 87	Lower	Truncated	Bar clinoforms	1.45	--	--	--	--	Fig. S3(P)
OM-Bar 88	Lower	Truncated	Bar clinoforms	0.65	--	--	--	--	Fig. S3(P)
OM-Bar 89	Lower	Truncated	Bar clinoforms	0.50	--	--	--	--	Fig. S3(P)
OM-Bar 90	Lower	Truncated	Bar clinoforms	0.40	--	--	--	--	Fig. S3(P)
OM-Bar 91	Lower	Truncated	Bar clinoforms	0.50	--	--	--	--	Fig. S3(P)
OM-Bar 92	Lower	Truncated	Bar clinoforms	0.30	--	--	--	--	Fig. S3(P)
OM-Bar 93	Lower	Truncated	Bar clinoforms	0.60	--	--	--	--	Fig. S3(P)
OM-Bar 94	Lower	Truncated	Bar clinoforms	0.60	--	--	--	--	Fig. S3(P)

OM-Bar 95	Lower	Truncated	Bar clinoforms	0.31	--	--	--	--	Fig. S3(P)
OM-Bar 96	Lower	Truncated	Bar clinoforms	0.30	--	--	--	--	Fig. S3(P)
OM-Bar 97	Lower	Truncated	Bar clinoforms	0.60	--	--	--	--	Fig. S3(P)
OM-Bar 98	Lower	Truncated	Bar clinoforms	0.60	--	--	--	--	Fig. S3(P)
OM-Bar 99	Lower	Truncated	Bar clinoforms	0.23	--	--	--	--	Fig. S3(Q)
OM-Bar 100	Lower	Truncated	Bar clinoforms	0.38	--	--	--	--	Fig. S3(Q)
OM-Bar 101	Lower	Truncated	Bar clinoforms	0.75	--	--	--	--	Fig. S3(Q)
OM-Bar 102	Lower	Truncated	Bar clinoforms	0.72	--	--	--	--	Fig. S3(Q)
OM-Bar 103	Lower	Truncated	Bar clinoforms	0.35	--	--	--	--	Fig. S3(Q)
OM-Bar 105	Lower	Truncated	Bar clinoforms	0.48	--	--	--	--	Fig. S3(R)
OM-Bar 106	Lower	Truncated	Bar clinoforms	1.05	--	--	--	--	Fig. S3(R)
OM-Bar 107	Lower	Truncated	Bar clinoforms	0.30	--	--	--	--	Fig. S3(R)
OM-Bar 108	Lower	Truncated	Bar	0.30	--	--	--	--	Fig. S3(R)

			clinoforms						
OM-Bar 109	Lower	Truncated	Bar clinoforms	0.48	--	--	--	--	Fig. S3(R)

TABLE S4.— LiDAR links to the Chamberlain Pass Formation and Orella Member outcrops.

Area	Link to LiDAR
Chamberlain Pass Formation	http://potree.villanova.edu/chamberlain/chamberlaintot/
Orella Member - Lower sand body	http://potree.villanova.edu/ts2/ts2_1p7/
Orella Member - Upper sand body	http://potree.villanova.edu/toadstool1/

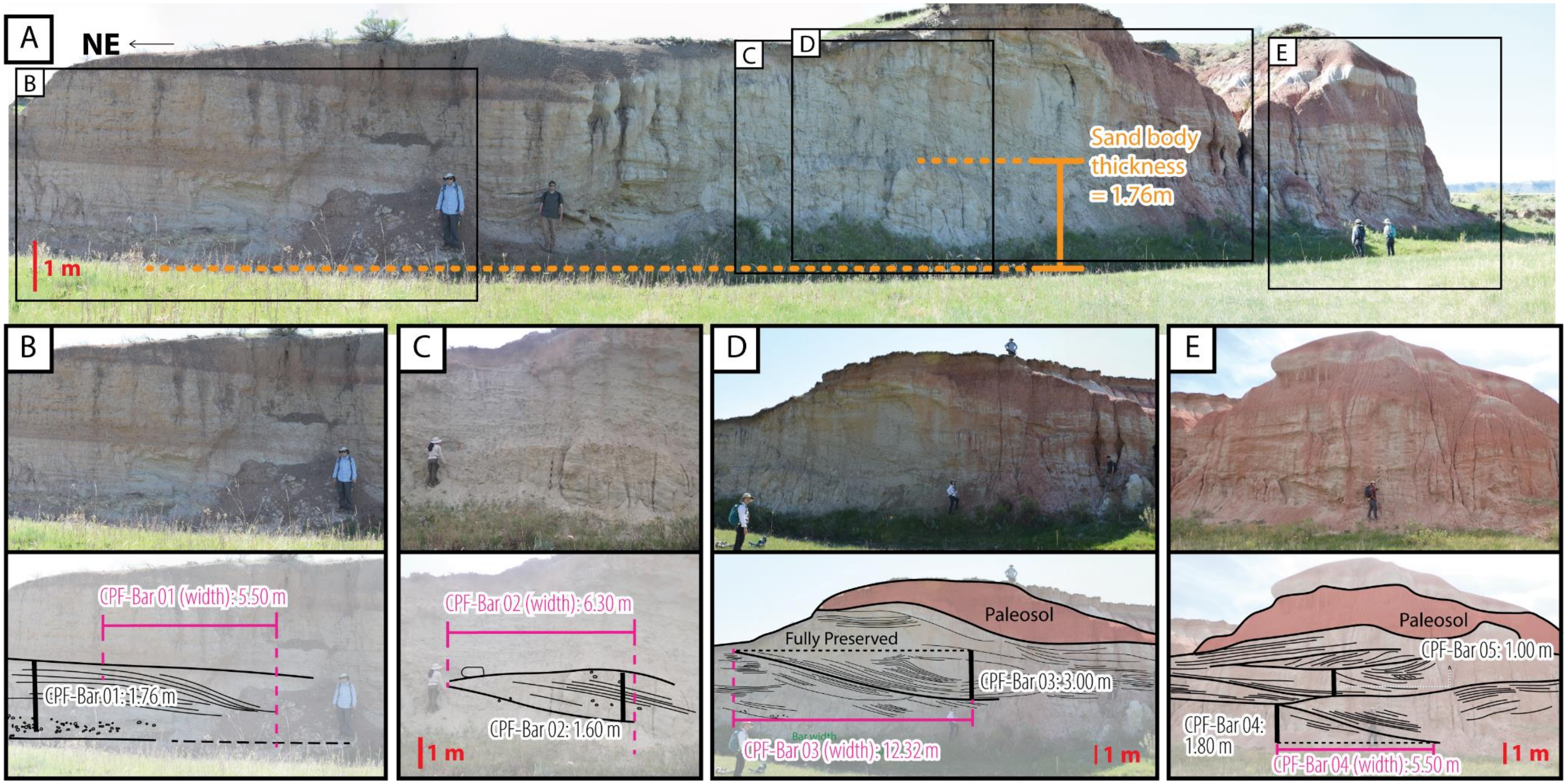

FIG. S1.— (A)-(E) Bar height and bar width results of Chamberlain Pass Formation (CPF).

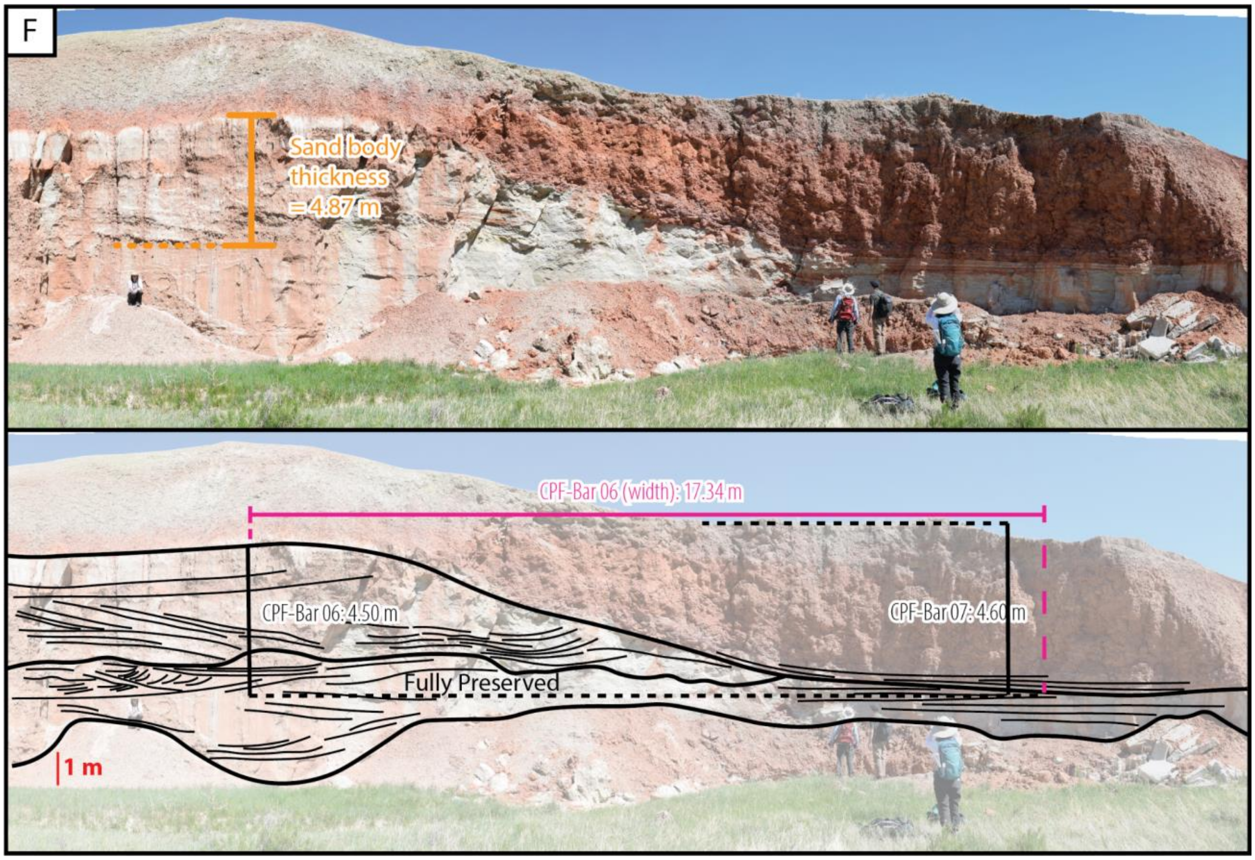

FIG. S1. (cont.)— (F) Bar height and bar width results of Chamberlain Pass Formation (CPF).

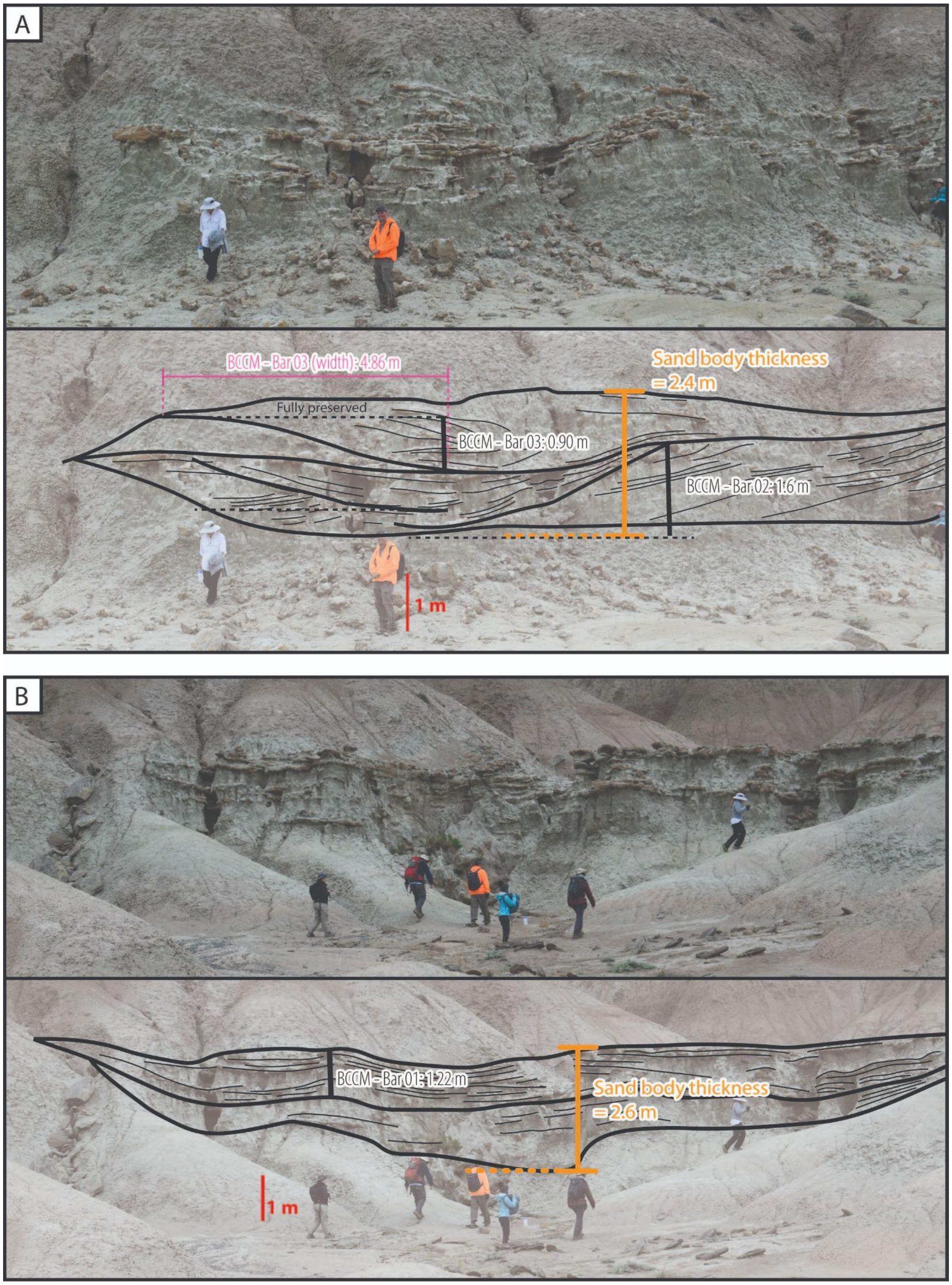

FIG. S2.— (A)-(B) Bar height and bar width results of Big Cottonwood Creek Member (BCCM) of Chadron Formation (CF).

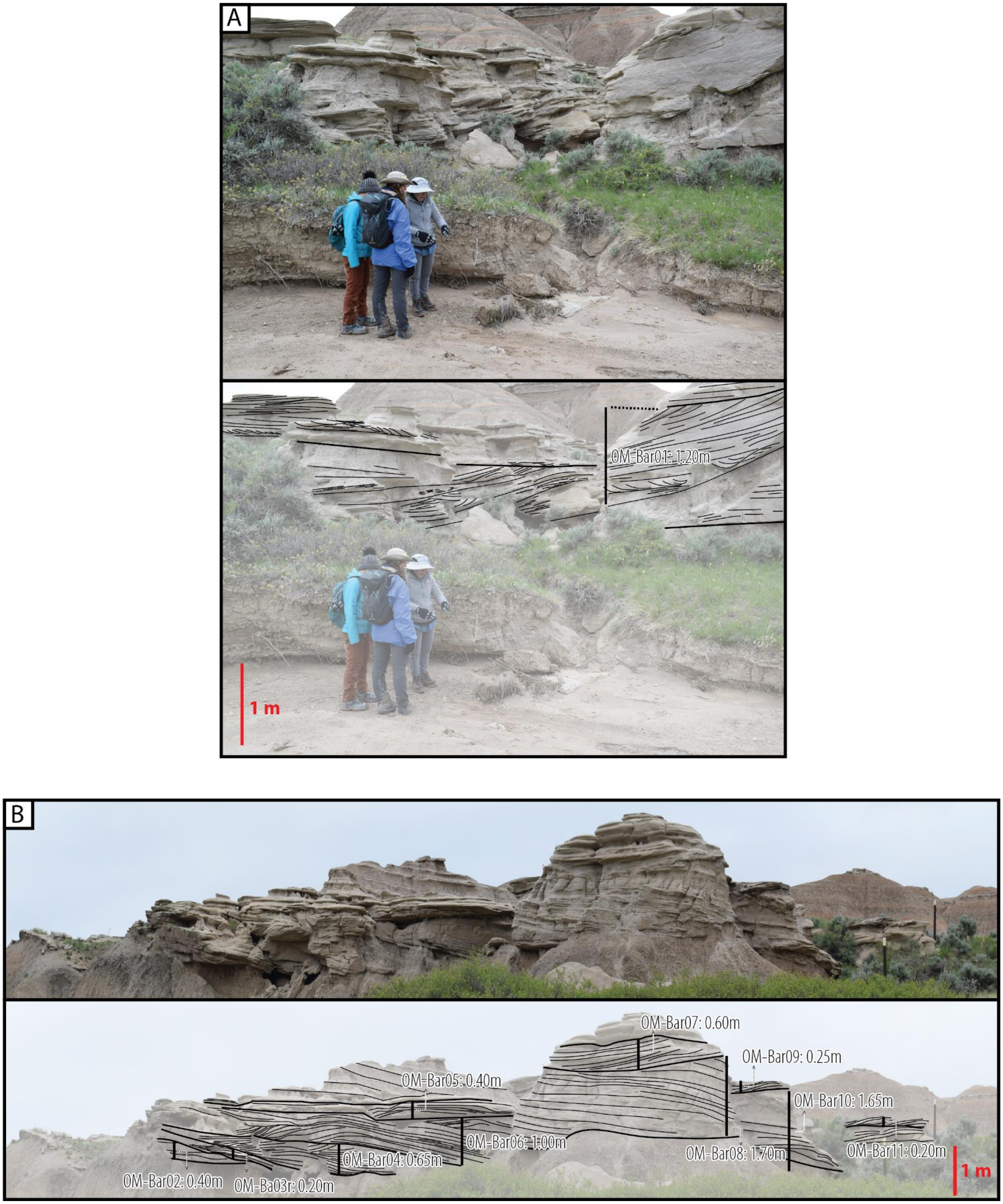

FIG. S3.— (A)-(B) Bar height and bar width results of Orella Member (OM).

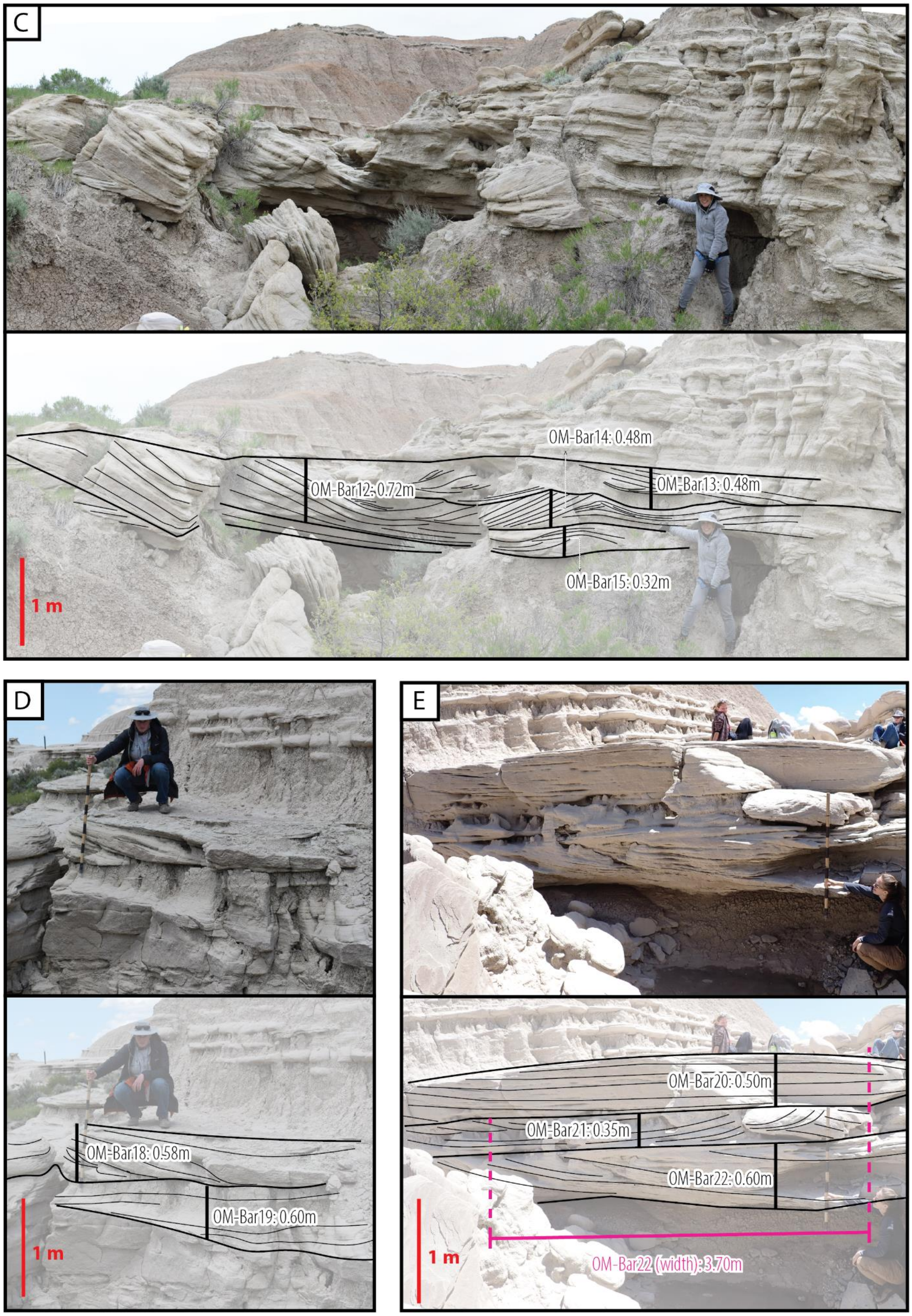

FIG. S3. (cont.)— (C)-(E) Bar height and bar width results of Orella Member (OM).

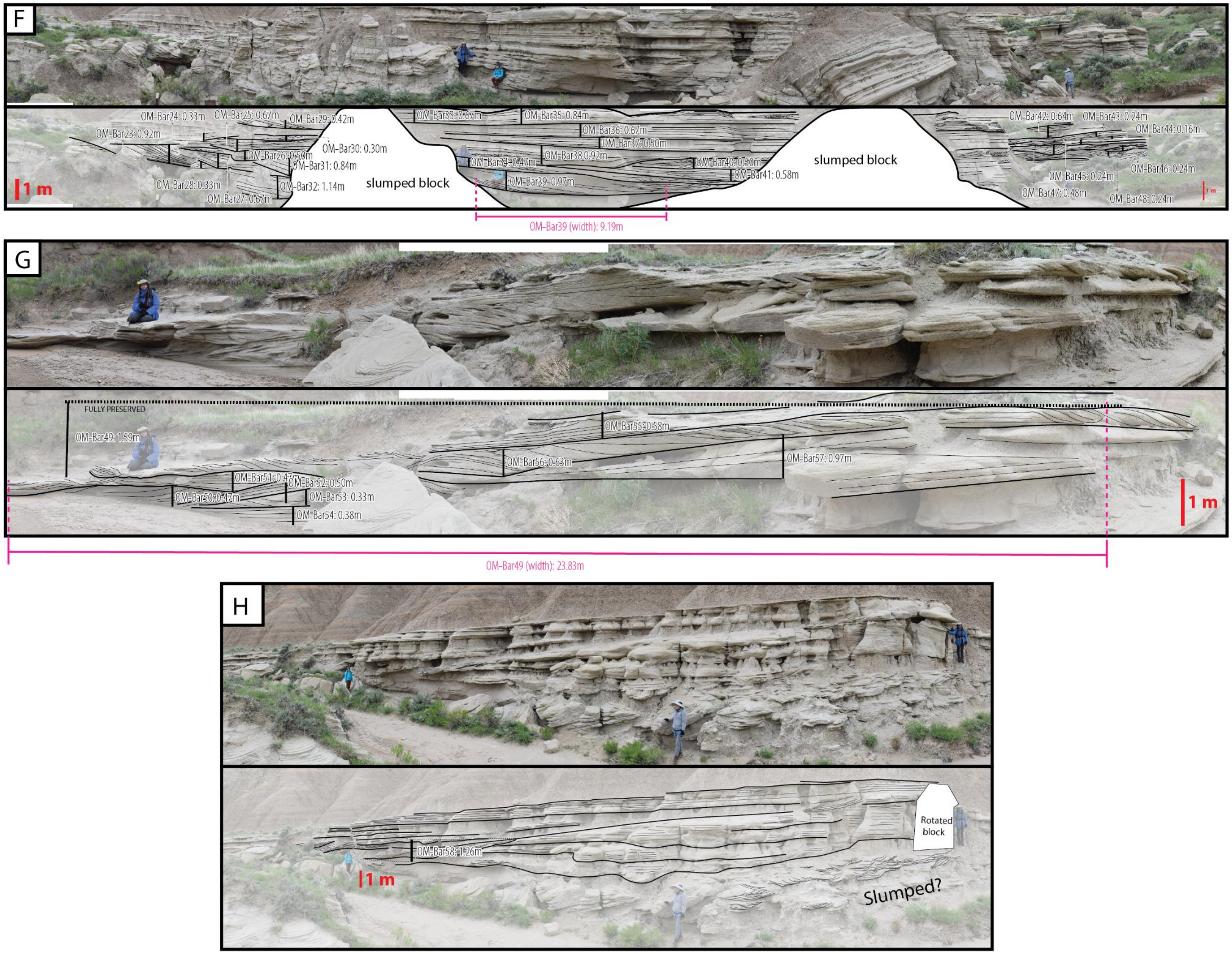

FIG. S3. (cont.)— (F)-(H) Bar height and bar width results of Orella Member (OM).

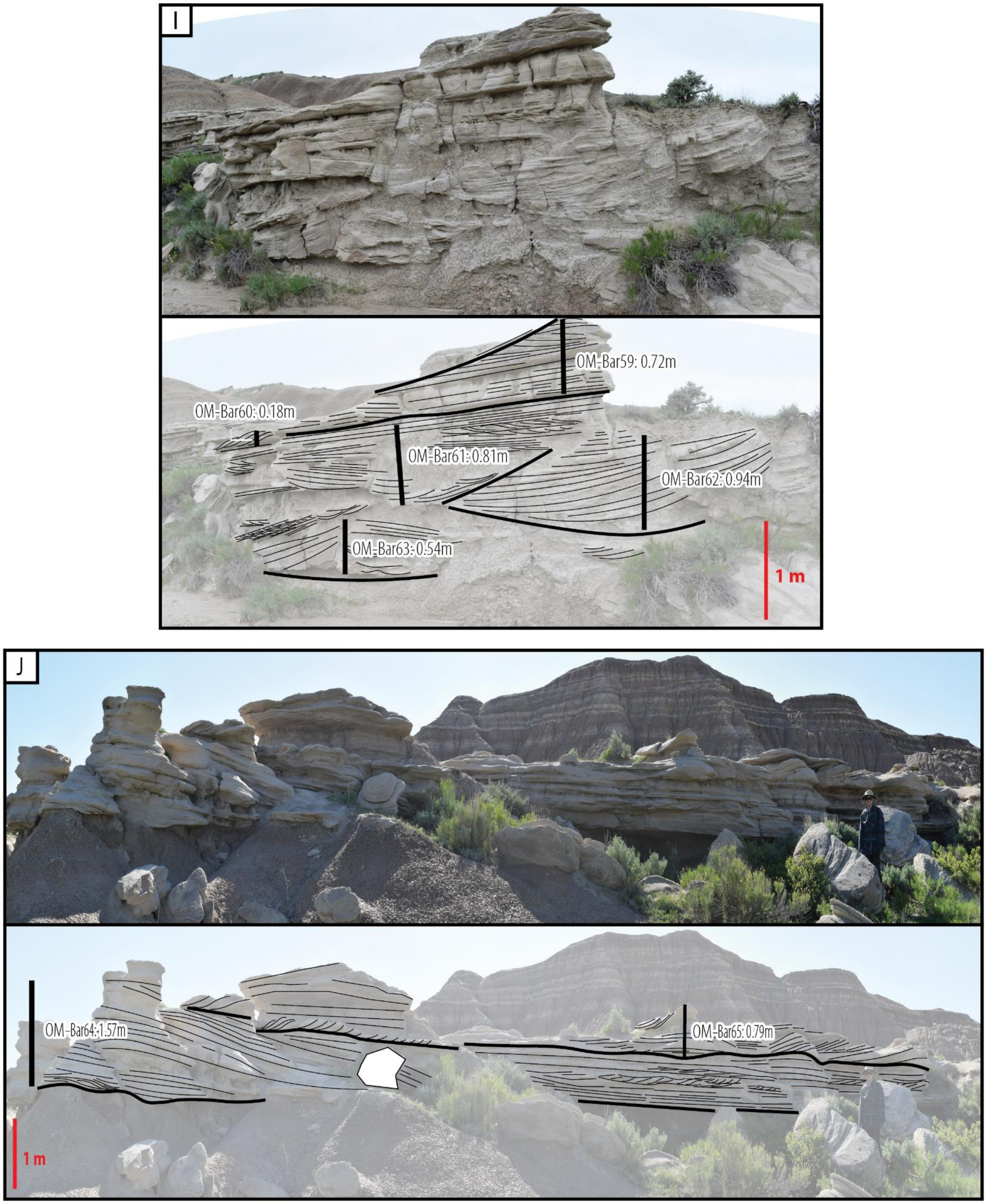

FIG. S3. (cont.)— (I)-(J) Bar height and bar width results of Orella Member (OM).

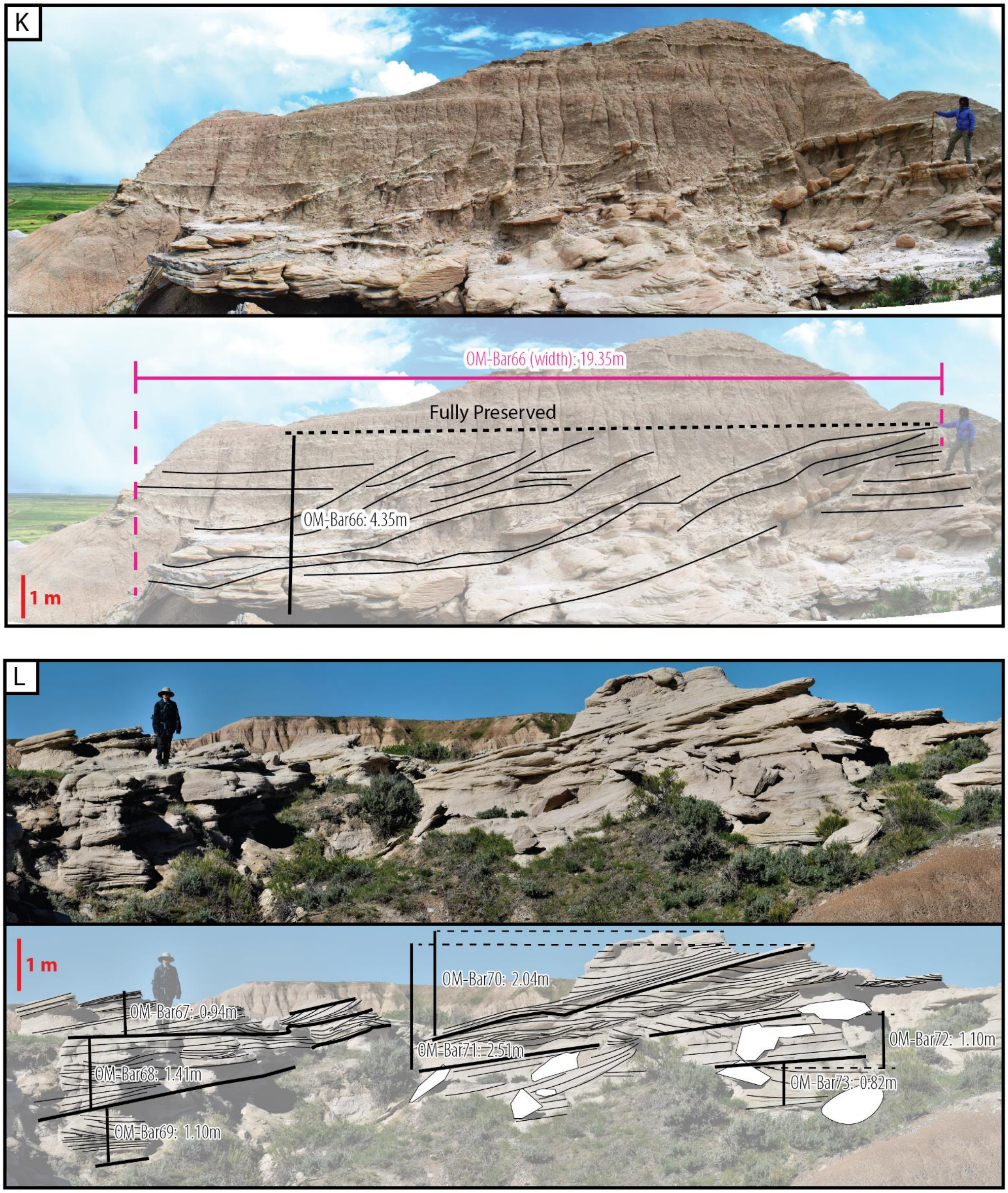

FIG. S3. (cont.)— (K)-(L) Bar height and bar width results of Orella Member (OM).

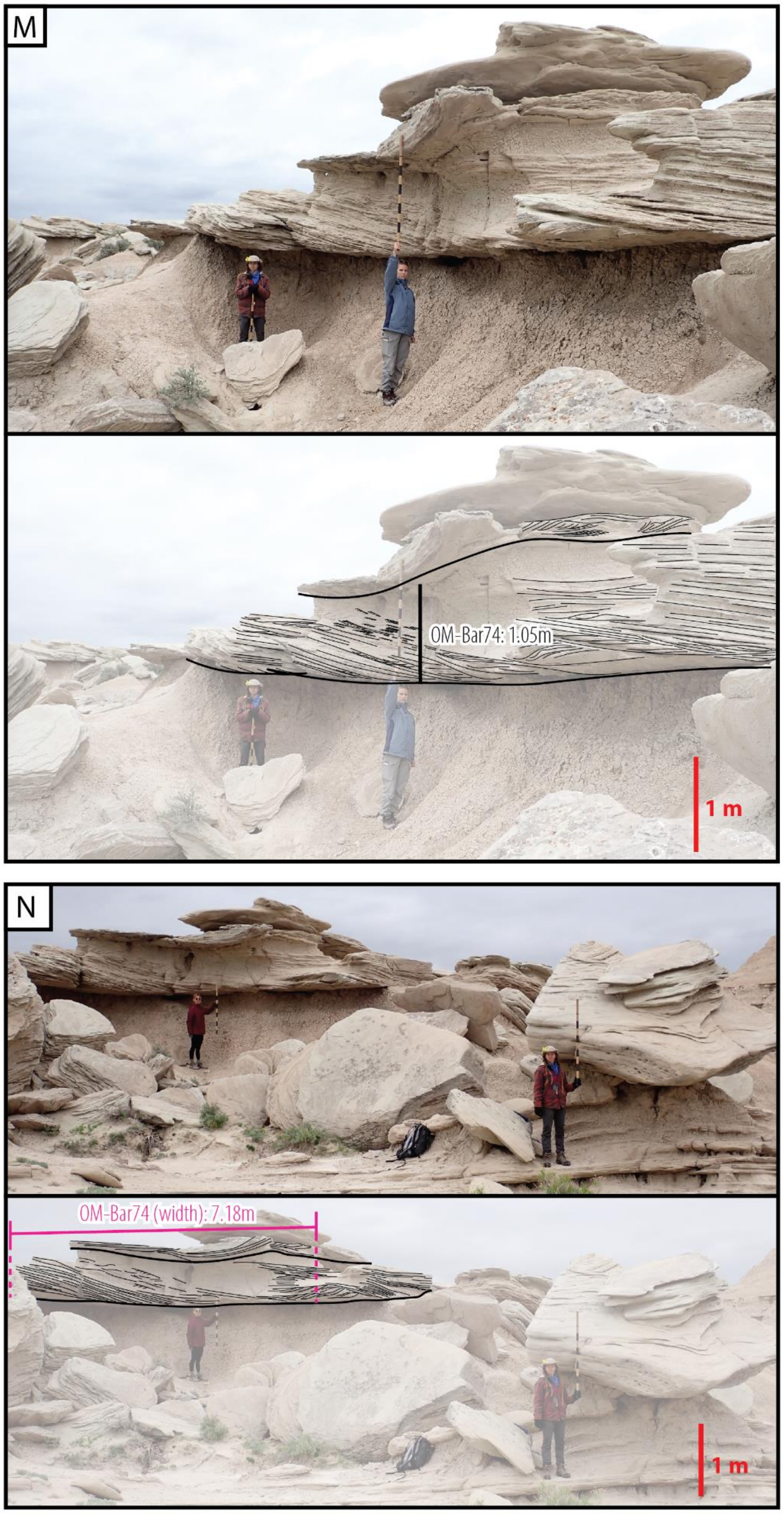

FIG. S3. (cont.)— (M)-(N) Bar height and bar width results of Orella Member (OM).

FIG. S3. (cont.)— (O)-(P) Bar height and bar width results of Orella Member (OM).

FIG. S3. (cont.)— (Q)-(R) Bar height and bar width results of Orella Member (OM).

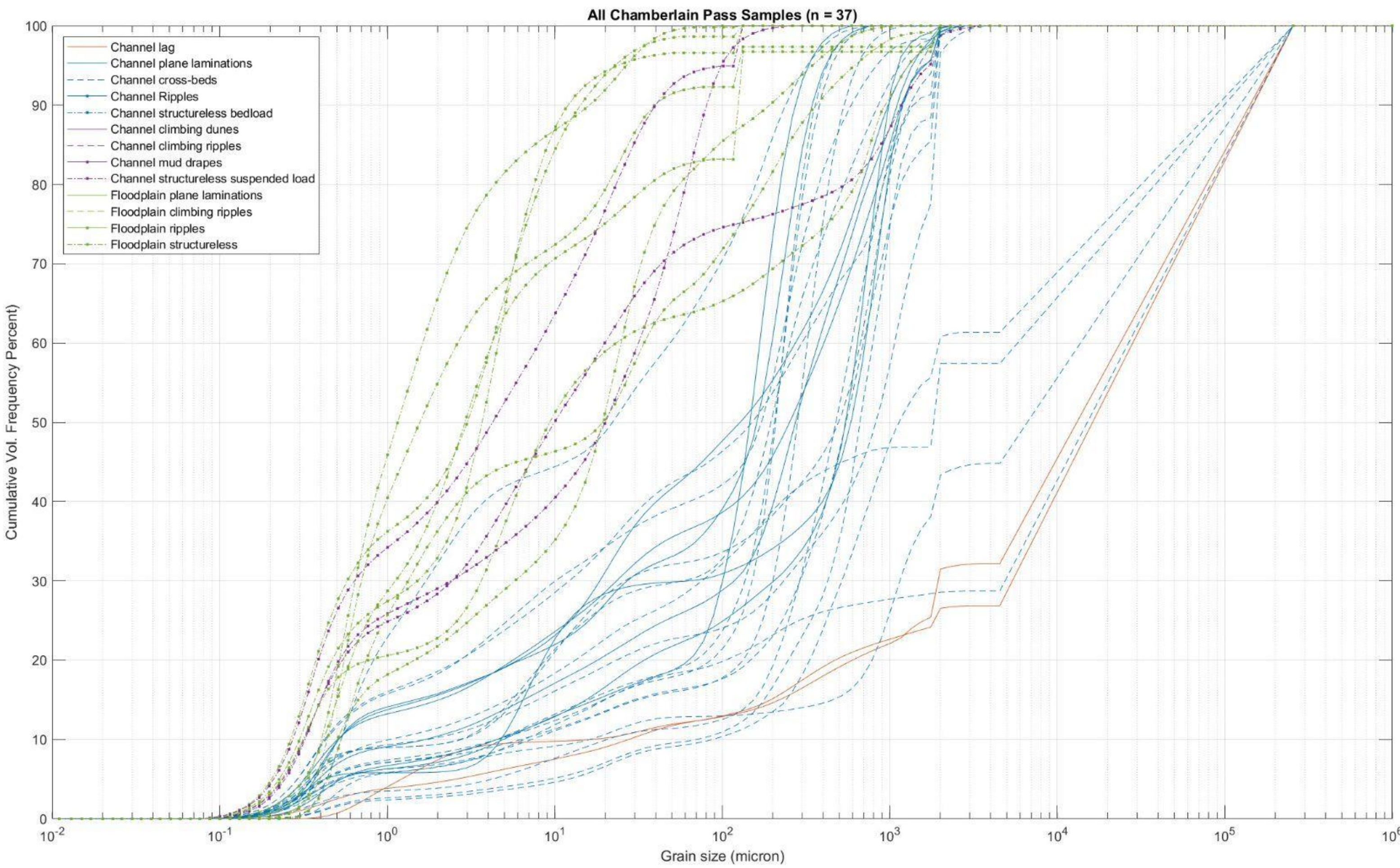

FIG. S4.— Grain size distribution associated with sedimentary facies of all samples of CPF.

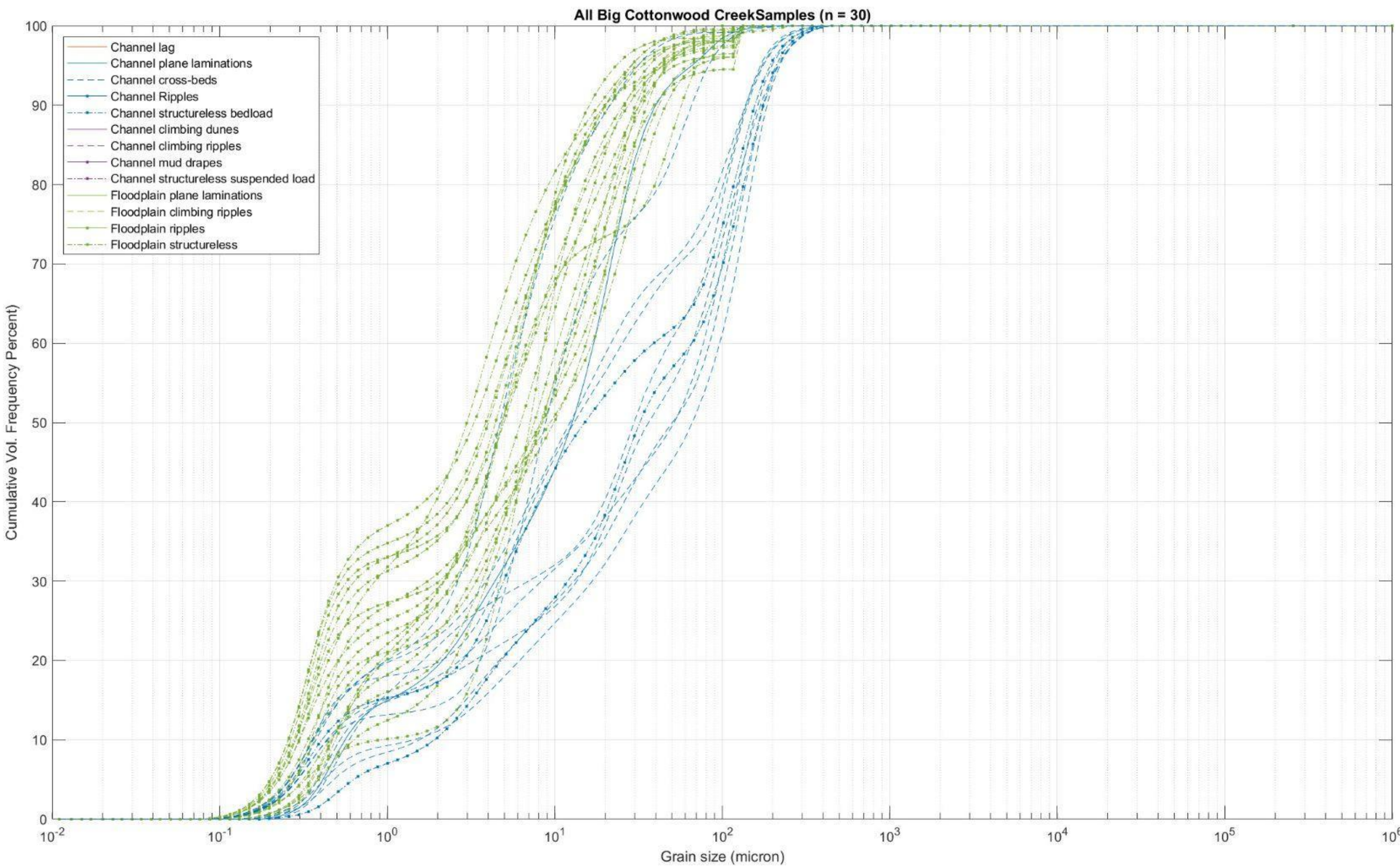

FIG. S5. — Grain size distribution associated with sedimentary facies of all samples of BCCM.

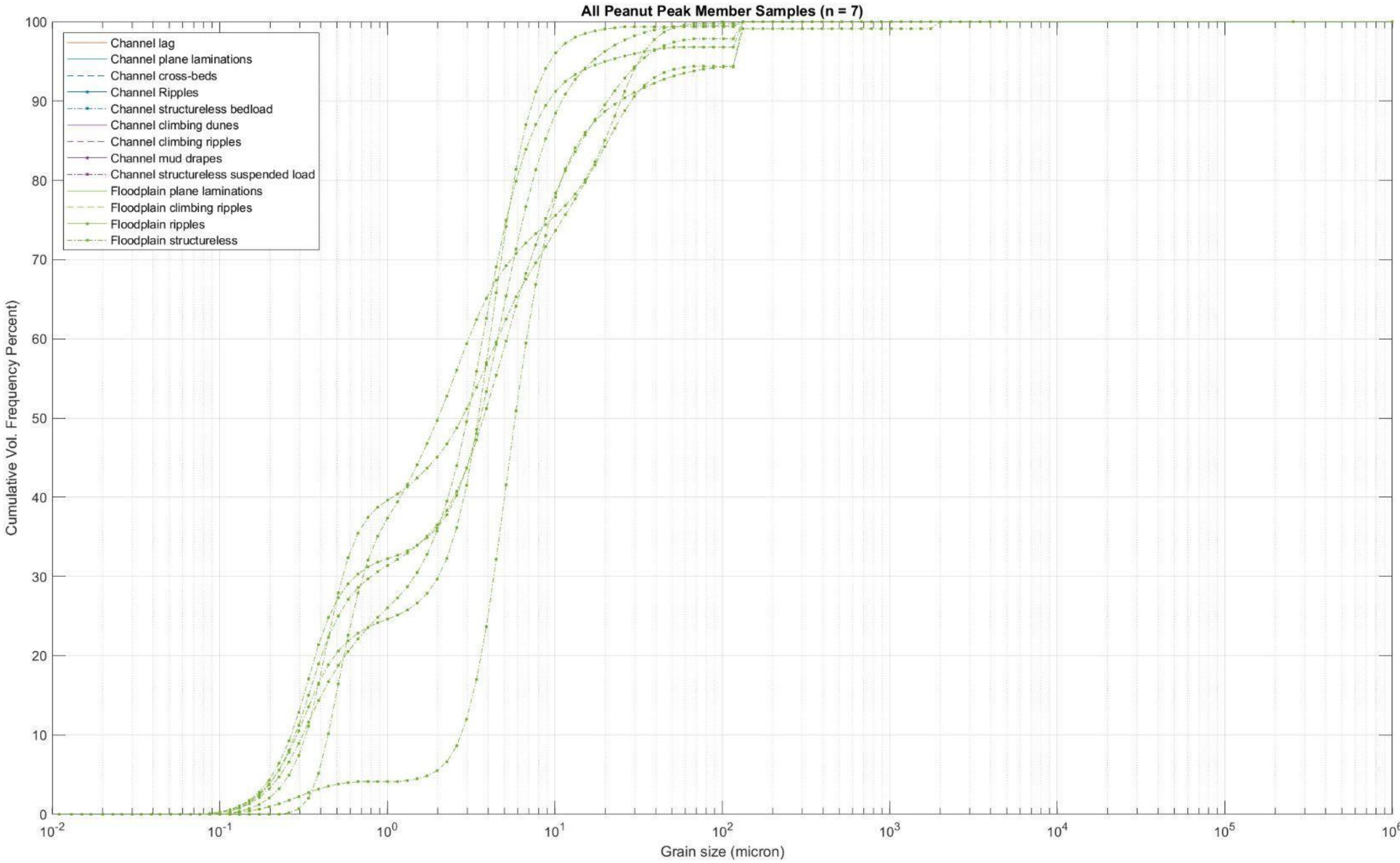

FIG. S6.— Grain size distribution associated with sedimentary facies of all samples of PPM.

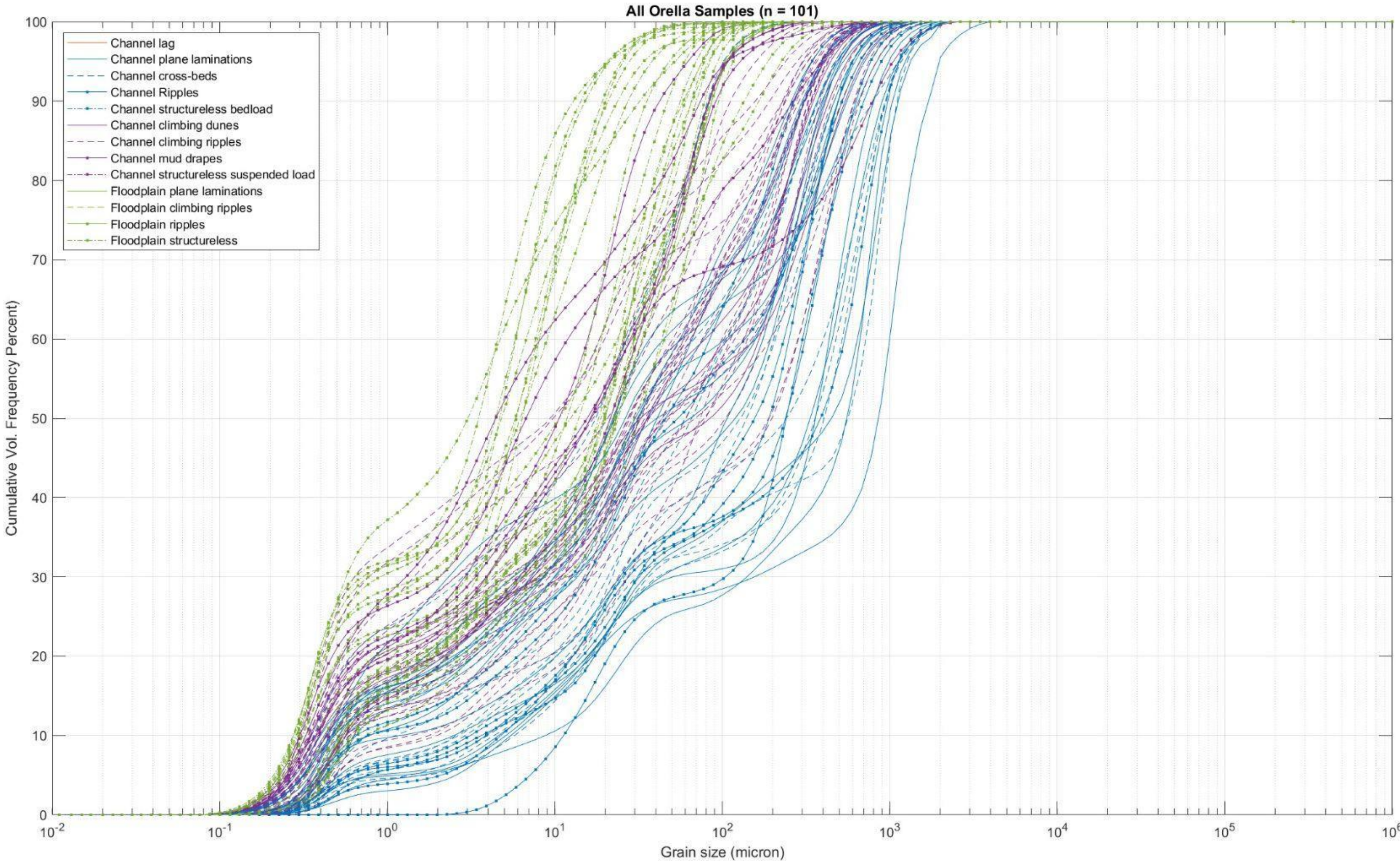

FIG. S7.— Grain size distribution associated with sedimentary facies of all samples of OM.

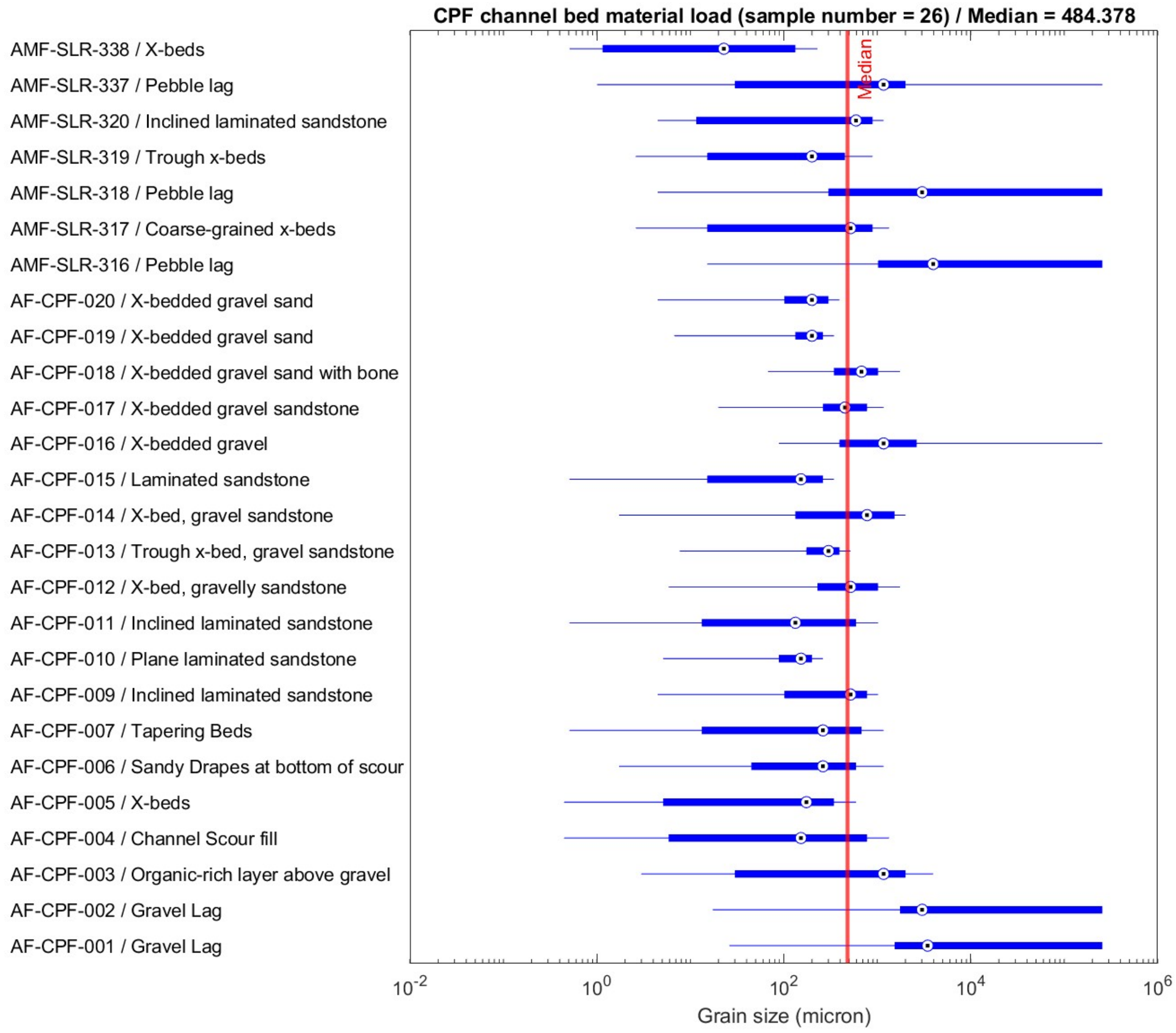

FIG. S8.— Grain size distribution of individual channel bed material load samples of CPF.

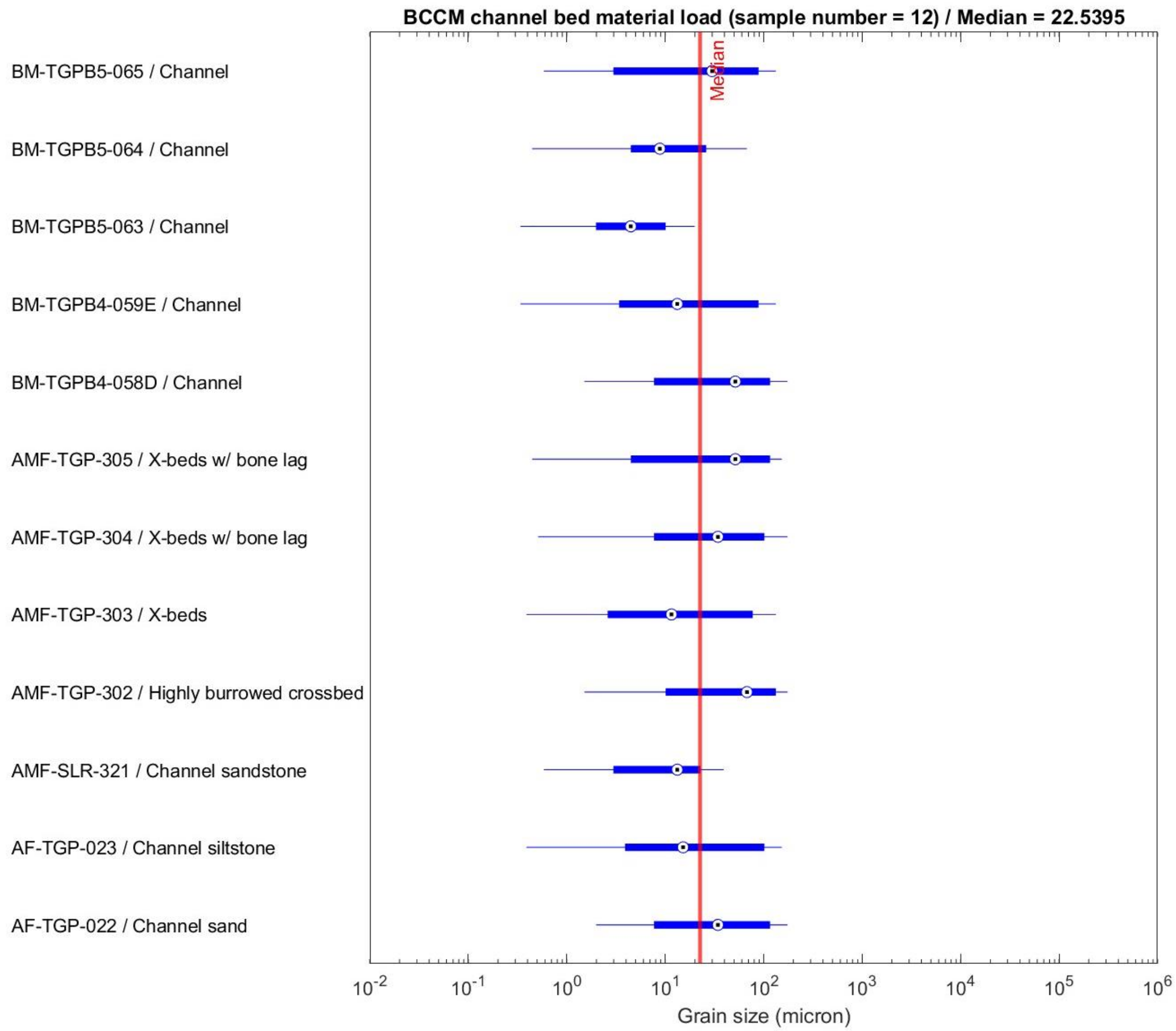

FIG. S9.— Grain size distribution of individual channel bed material load samples of BCCM.

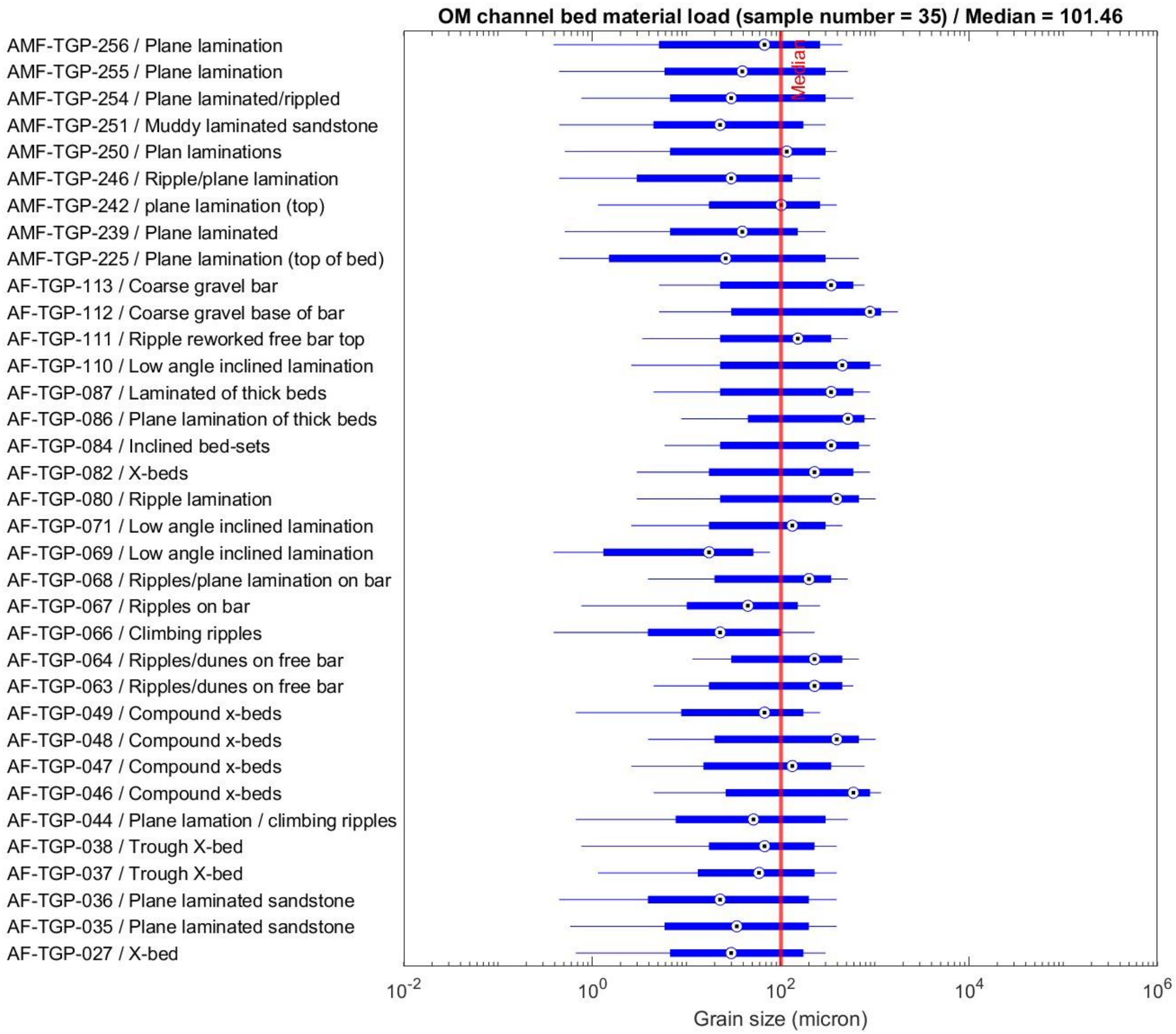

FIG. S10.— Grain size distribution of individual channel bed material load samples of OM.

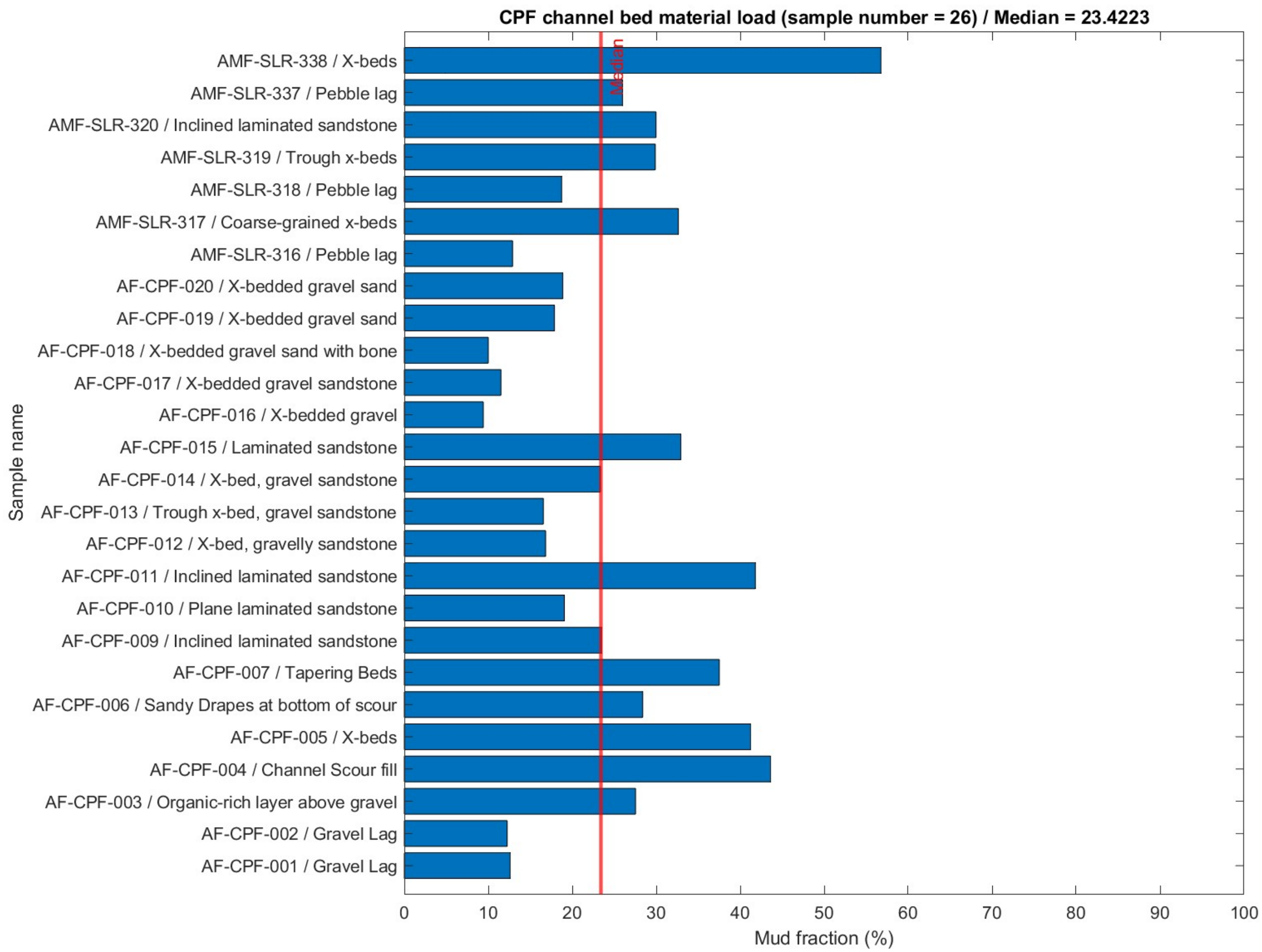

FIG. S11.— Mud fraction of individual channel bed material load samples of CPF.

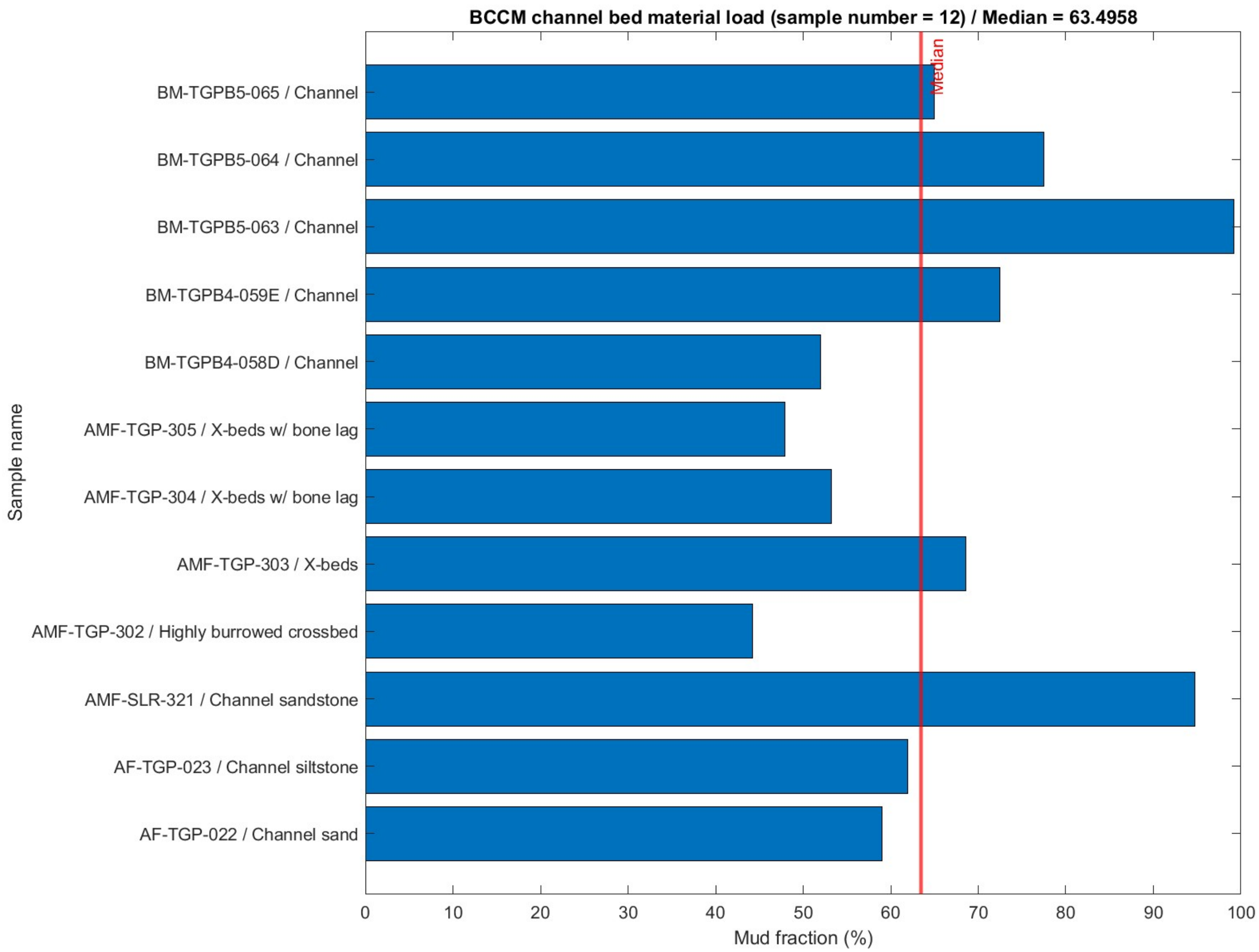

FIG. S12.— Mud fraction of individual channel bed material load samples of BCCM.

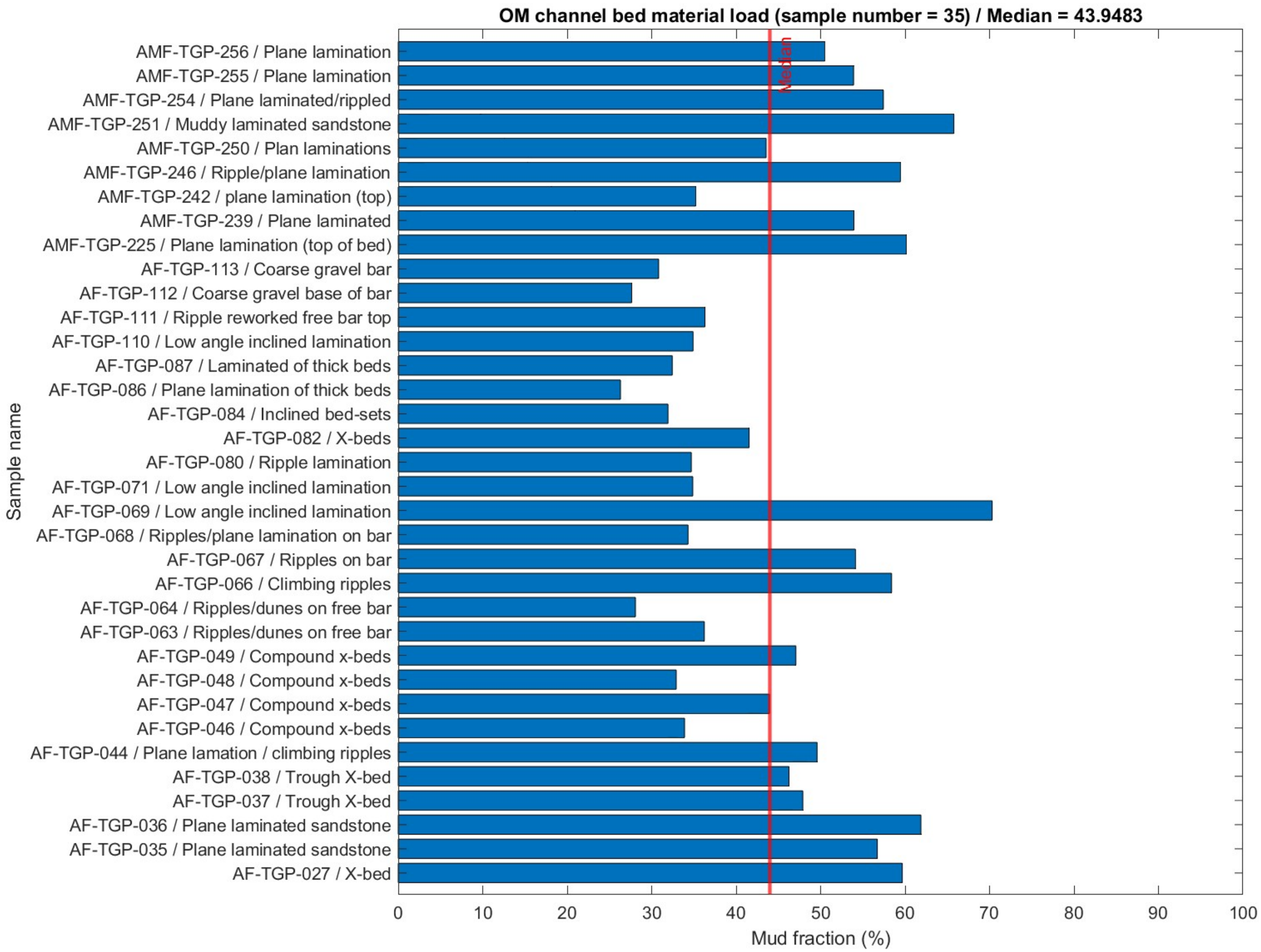

FIG. S13.— Mud fraction of individual channel bed material load samples of OM.

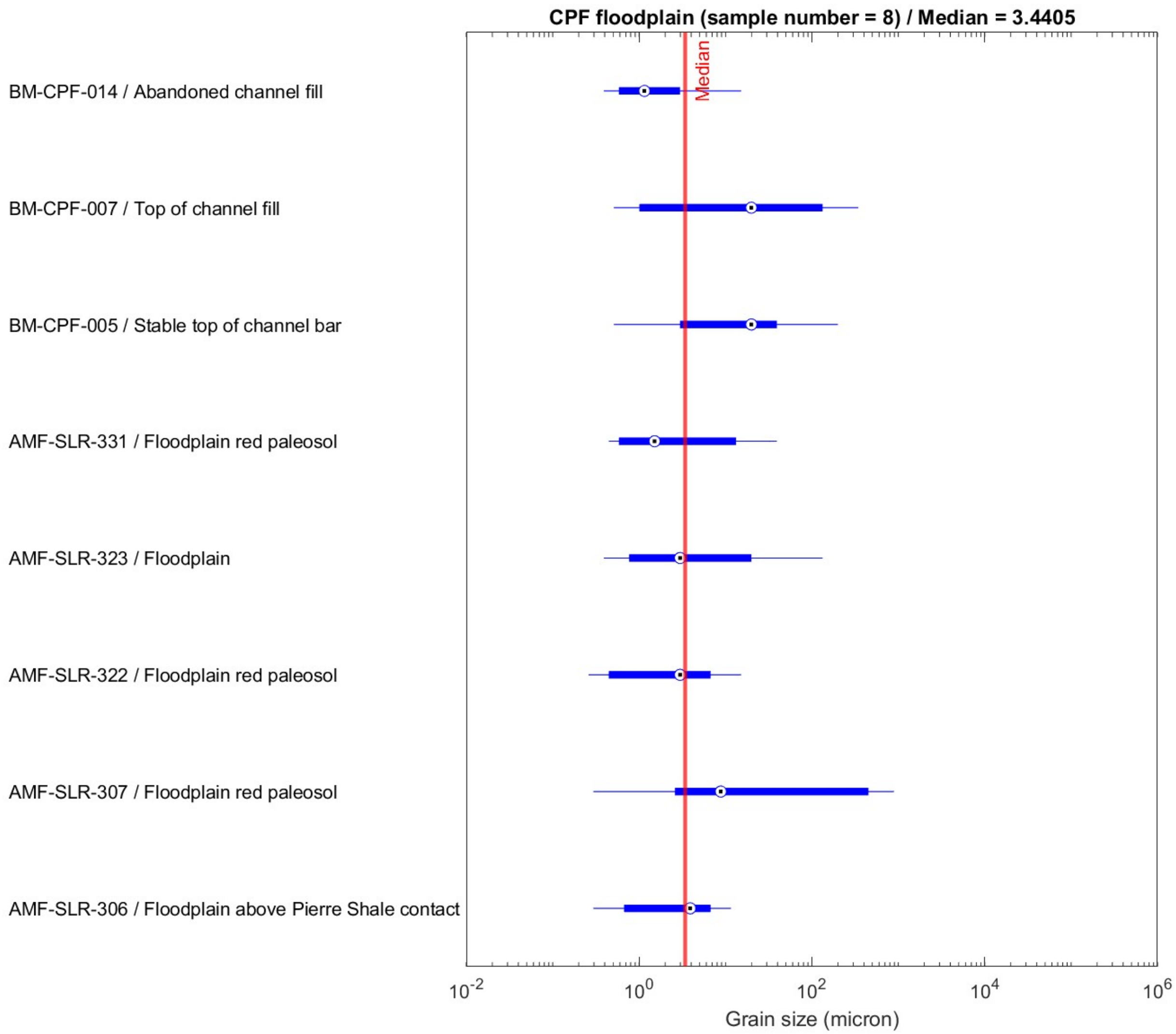

FIG. S14.— Grain size distribution of individual floodplain deposits samples of CPF.

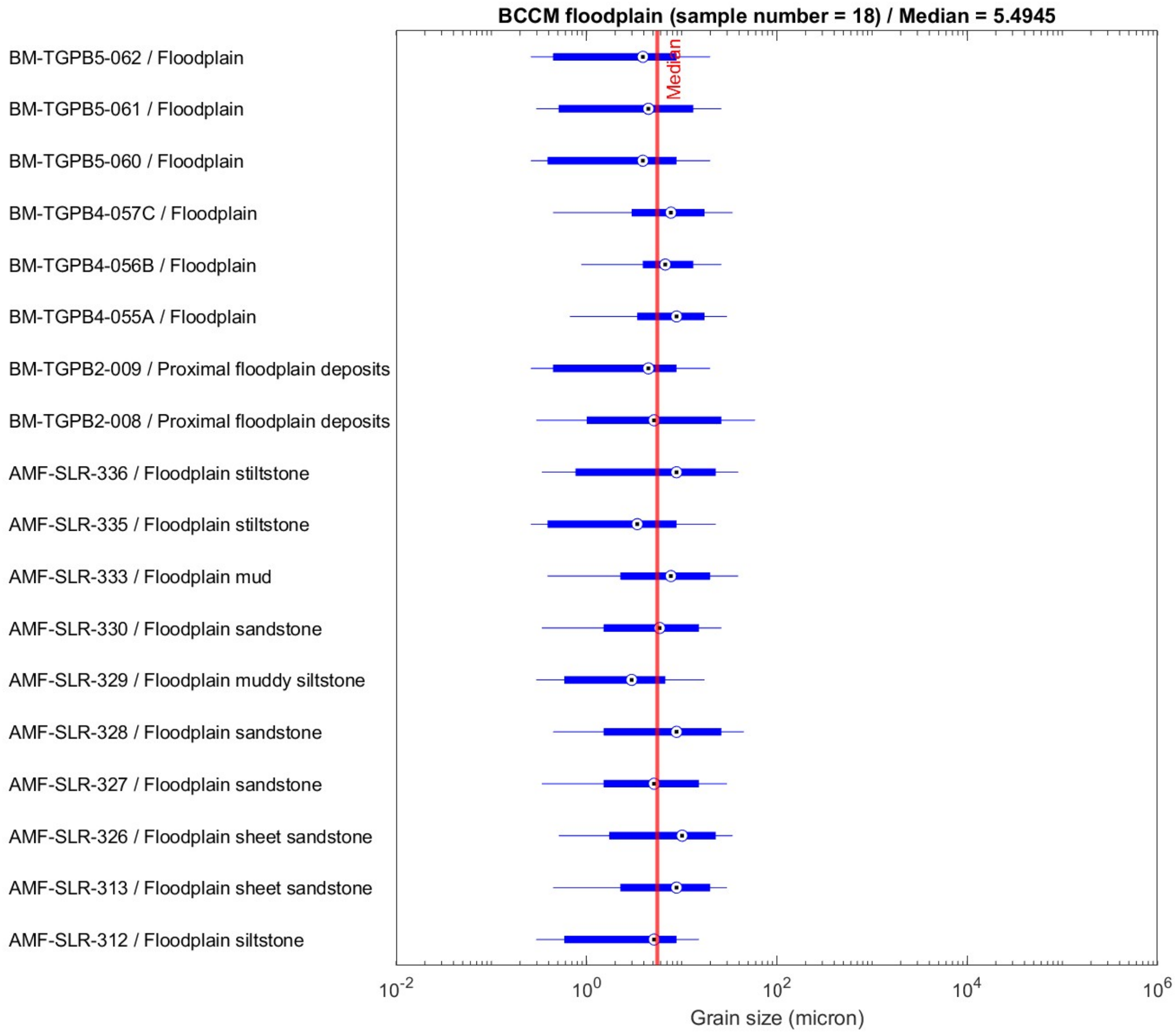

FIG. S15.— Grain size distribution of individual floodplain deposits samples of BCCM.

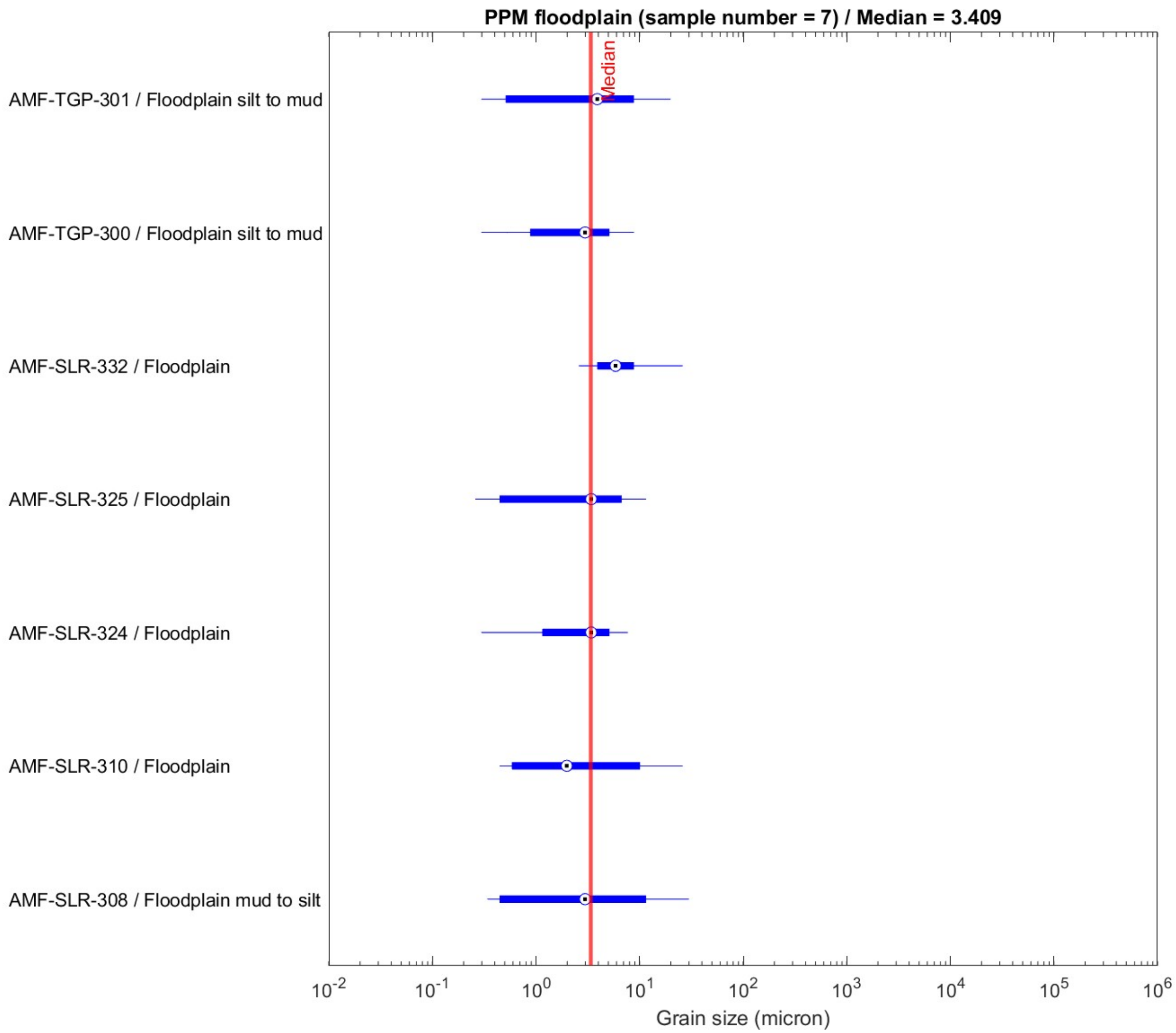

FIG. S16.— Grain size distribution of individual floodplain deposits samples of PPM.

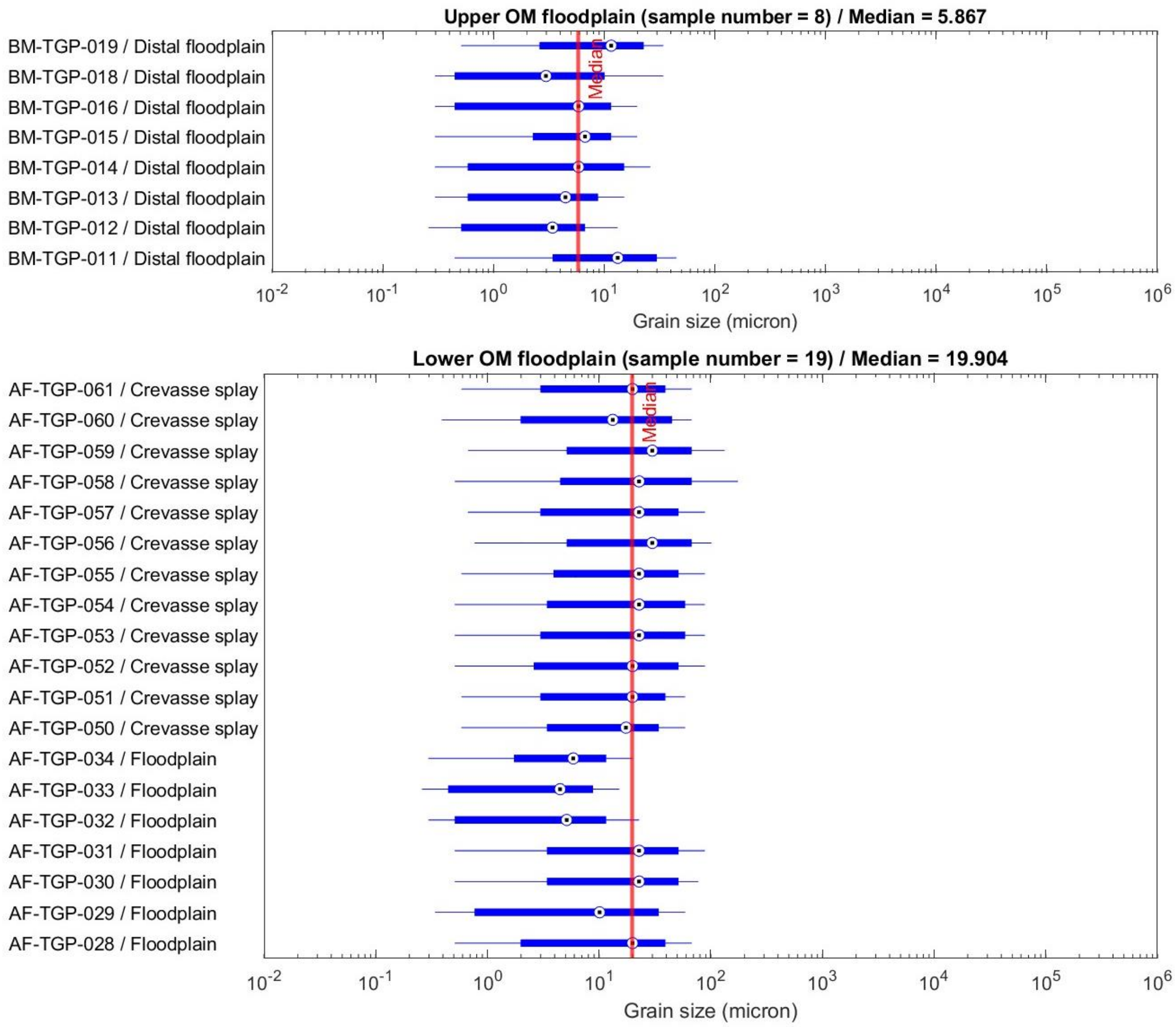

FIG. S17.— Grain size distribution of individual floodplain deposits samples of OM